Analytical methods for mapping river bathymetry from multi-spectral satellite images

Shayan Salavitabar

A Thesis

in

the Department

of

Building, Civil and Environmental Engineering

Presented in Partial Fulfillment of the Requirements

for the Degree of

Master of Applied Science (Civil Engineering) at

Concordia University

Montréal, Quebec, Canada

August 2021

CONCORDIA UNIVERSITY

SCHOOL OF GRADUATE STUDIES

This is to certify that the thesis prepared

By: **Shayan Salavitabar**

Entitled: **Analytical methods for mapping river bathymetry from multi-spectral satellite images**

and submitted in partial fulfillment of the requirements for the degree of

Master of Applied Science (Civil Engineering)

Complies with the regulations of the University and meets the accepted standards with respect to originality and quality.

Signed by the final examining committee:

____ Chair

Dr. Attila Michael Zsaki

____ Examiner

Dr. Angela Kross

____ Examiner

Dr. Attila Michael Zsaki

____ Supervisor

Dr. S. Samuel Li

Approved by ____

Dr. Ashutosh Bagchi, Chair

Department of Building, Civil and Environmental Engineering

____________2021 ____________________________________

Dr. Mourad Debbabi, Dean

Gina Cody School of Engineering and Computer Science

ABSTRACT

Analytical methods for mapping river bathymetry from multi-spectral satellite images

Shayan Salavitabar

Rivers are an important part of the aquatic environment, which supply freshwater essential to human life, support economic activities, and provide natural habitats for aquatic species. The river environment needs to be managed properly for the protection of river floods, channel erosion and water pollution as well as for the safety of in-stream hydraulic and other river engineering structures. River management needs data of river channel bathymetry as fundamental input. The purpose of this research is to explore new, efficient methods for mapping channel bathymetry. Traditionally, field methods are used for point-by-point measurements of flow depth, which need an operator to use instrument at a river site. The field methods are costly and inconvenient, true particularly for remote river sites. Recently, advancing remote sensing technology has offered promising opportunities for mapping river bathymetry, leading to the development of some empirical methods for converting light intensity in satellite images to river flow depth. A major shortcoming of the methods is that the conversion involves a light attenuation coefficient; its value needs to be determined using adequate field measurements from a river site of application, which are often not available. This thesis reports new analytical methods for retrieving river bathymetry from multi-spectral high-resolution satellite images. No field measurements are needed for the determination of regression relationships. The analytical methods are applied to a 25-km reach of the Nicolet River in Quebec, Canada. The application uses multi-spectral high-resolution images from WorldView-2 and WorldView-3 satellites. The methods involve radiometric corrections to images in order to remove the atmospheric effect on wavelengths and calculations of effective attenuation coefficient that allows for the effects of water column on the wavelengths. After removing the ambient effects, the ratio of a pair of selected wavelengths is used in algorithms for determining the flow depth. The bathymetry results show an 85% accuracy for WorldView-3 satellite image. The accuracy is lower for WorldView-2 satellite image due to a lack of two atmospheric factors in radiometric correction. The results offer a spatial resolution as high as 1.2-

m (for WorldView-3 image). Analytical methods have been used in coastal water and marine applications. This study is perhaps the first application to the river environment, where the spatial gradient of depth is typically much larger than those of the coastal and marine environment. There is no doubt that future satellite operations will provide increasing spatial resolution and coverage. There is a great potential to revolutionise the approach to mapping river bathymetry and to substantially reduce the need of costly and time-consuming field efforts.

ACKNOWLEDGEMENTS

I would like to express my deep and sincere gratitude to my supervisor Dr. S. Samuel Li for his continued support and valuable advice throughout my studies. I am extremely grateful to have this chance to complete my studies with him and learn from his expertise.

I am also thankful to my parents and sister for their support and encouragement through this academic journey.

Last but not the least, I would also like to express my appreciation to my friends especially, Amirreza Karimi, for his support during living in Montreal.

Table of contents

LIST OF FIGURES

LIST OF TABLES

LIST OF SYMBOLS

This study has used the following symbols:

a	Absorption coefficients (m^{-1})
$a_w(\lambda)$	Absorption coefficient for pure water (m^{-1})
$\Delta a(\lambda)$	Absorption of suspended loads (m^{-1})
$a(555)$	Absorption coefficient for reference band (m^{-1})
b_b	Total Backscattering Coefficients (m^{-1})
b_{bp}	Backscattering coefficient of suspended particles (m^{-1})
b_{bw}	Backscattering coefficient of pure seawater (m^{-1})
$b_{bp}(555)$	Backscattering coefficient of suspended particles for reference band (m^{-1})
$b_{bw}(555)$	Backscattering coefficient of pure water for reference band (m^{-1})
C	Transmission across air-water interface
d_{ES}	The Earth-sun distance (AU)
DN	Digital Number (pixel value) recorded by satellite sensors
DN_0	Pixel values before light entering water
E_d	Downwelling solar irradiance ($Wm^{-2}nm^{-1}$)
E_λ	Solar exoatmospheric irradiance ($Wm^{-2}\mu m^{-1}$)
f	Geometric factor
H	Orthometric height (m)
h	Ellipsoid height (m)
I_0	Intensity of light before entering the water
I(z)	Intensity of light in the depth of z
JD	Julian Day
K	Attenuation coefficient (m^{-1})
$\overline{K}$	Effective attenuation coefficient (m^{-1})
$\overline{K}_d$	Effective diffuse attenuation coefficient (m^{-1})
K_d	Diffuse attenuation coefficient (m^{-1})
$L_B(\lambda)$	Total radiance related to bottom ($Wm^{-2}\mu m^{-1}sr^{-1}$)
L_λ	Radiance for wavelength (λ) ($Wm^{-2}\mu m^{-1}sr^{-1}$)

L_p	Path radiance from the atmosphere ($Wm^{-2}\mu m^{-1}sr^{-1}$)
L_K	Diffuse sky radiance ($Wm^{-2}\mu m^{-1}sr^{-1}$)
L_{si}	Deep-water radiance including scattering effect ($Wm^{-2}\mu m^{-1}sr^{-1}$)
L_T	Total radiance of a band ($Wm^{-2}\mu m^{-1}sr^{-1}$)
n_0	Offset for depth zero
n_1	Tunable constant
m_0, m_1, and m_3	Attenuation Constants
N	Geoid height (m)
R	Ratio of bottom reflectance
R	Reflectance of wavelength
R_{bo}	Bottom reflectance
R_b	Substrate reflectance
$R_{b\lambda}$	Substrate reflectance of wavelength (λ)
R_c	Volume reflectance of the water column
R_E	Effective reflectance
R_λ	Reflectance-corrected
R_{rs}	Above-surface remote-sensing reflectance
r_{rs}	Below-surface remote-sensing reflectance
R_W	Reflectance from molecules and particles in the water column
T	Transmittance of the atmosphere
TR	Transformed Ratio Feature
U	Total number of ratio models
u	Ratio of backscattering coefficient to the sum of absorption and backscattering coefficients
X	Natural algorithm ratio between two bands
X^p	Known depth samples (m)
X^t	Unknown depth samples (m)
Y	Spectral power for particles
z	Water depth (m)
Z	Image-derived depth (m)

z_0	Initial depth (m)
$\Delta z(\lambda)$	The smallest detectable changes in depth (m)
Θ_s	Solar zenith angle
λ	Wavelength
λ_0	Reference wavelength
ρ	A calcutation factor to describe absorbtion
$\rho(TOA)$	Top of atmosphere reflectance

LIST OF ABBREVIATIONS

ADCP	Acoustic Doppler Current Profiler
SD	Analytical Spectral Devices
AU	Astronomical Unit
CGVD2013	The Canadian Geodetic Vertical Datum of 2013
CGVD28	The Canadian Geodetic Vertical Datum of 1928
CNES	National Centre for Space Studies of French
DEM	Digital Elevation Model
ERTS-A	Earth Resources Technology Satellite-A
ETM+	Enhanced Thematic Mapper Plus
GPS	Global Positioning System
HYDAT	Hydrometric Database
IMU	Inertial Measurement Unit
KaRIn	Ka-band Radar Interferometer
LiDAR	Light Detection and Ranging
MODIS	Moderate Resolution Imaging Spectroradiometer
MSL	Mean Sea Level
MSS	Multispectral Scanner
NASA	National Aeronautics and Space Administration
NDWI	Normalized Difference Water Index
NIR	Near-infrared
NRC	Natural Resources of Canada
OBRA	Optimal Band Ratio Analysis
OBRA	Optical Band Ratio Analysis
OLI	Operational Land Imager
QAA	Quasi-Analytical Algorithm
RBV	Return Beam Vidicon
RTK	Real-Time Kinematic

SMART-SDB	Sample-specific Multiple band Ratio Technique for Satellite-Derived Bathymetry
SRTM	Shuttle Radar Topography Mission
SWIR	Short Ware Infrared
SWOT	Surface Water and Ocean Topography
TM	Thermic Mapper
UAVs	Unmanned Aerial Vehicles
USGS	U.S. Geological Survey
UTC	Coordinated Universal Time
UTM	Universal Transverse Mercator
WRC	World Radiation Center

1 INTRODUCTION

1.1 Background

Rivers play an essential role in supporting life. Human civilisation and many forms of life on this planet have an active interaction with the rivers (Wiyanarti 2018). Cities and villages from historical time have been developing near the rivers, and almost all of them around the world depend on water carried by the rivers.

Rivers evolve on the Earth (Yalin 2015) and they support wildlife. All living things, particularly aquatic creatures, depend on the quality and quantity of water flowing in river channels (Wiyanarti 2018). Rivers also have a fundamental effect on shaping landscape. River flows have the power to erode and deposit sediments. This power enables them to create canyons and valleys or to build deltas. Because of these significant effects that rivers have on humans and wildlife, scientists and researchers are making continuous efforts for a better understanding and prediction of river flow characteristics. Determining river morphology is one of the most important elements in river studies. River morphology can reveal practical information of a river and it requires a good understanding of physical processes in rivers (Feurer et al. 2008). Knowledge of river morphology includes flow depth, flow velocity, channel width, bottom slope and so on (Matsuda 2004).

River flow depth is an essential variable among the above-mentioned variables in river morphology. Flow depth governs river engineering design and ecological design. For example, the health of fish habitats requires a minimum flow depth between the water surface and the riverbed in order to protect fish species. The challenge is that the flow depth varies at different temporal and spatial scales. Is there an efficient and cost-effective way to obtain data of flow depth? This question has become one of the active research subjects in the study of the river environment.

Several methods have been developed for acquisition of river flow depth. They include such methods as the use of a plumb line, and sound navigation and ranging (sonar), which are in-situ measurements (Farr 1980). They generally depend on deploying operators and instruments to a river site for depth measurements. Such methods are not only costly and time-consuming but also inconvenient. In the case of remote river sites, sending operators to the sites, and the logistics involved are difficult. The difficulties of access to a remote site are well-documented (Wang et al. 2015).

Over the past several decades, remote sensing technology has been used for the retrieval of geometries of shallow rivers and inaccessible rivers, and for mapping of large-scale depths (Farr 1980). The recent advancement of satellite remote sensing technology has led to the capacity of producing high resolution images with sensors that cover river bathymetry. This is a new opportunity, compared to earlier use of satellite images for bathymetry retrieval, which offered only low-resolution images. Such images may be adequate for ocean and coastal water applications. Accordingly, methods for obtaining bathymetry through analysing satellite images were applied to oceans and coastal waters. In these water bodies, depth changes in space are not as rapid, and therefore the results of depth from analysing satellite images are acceptable. Now, satellites can offer much higher resolution images; it becomes practical to obtain bathymetries of rivers where the water depths can change considerably in space.

Generally speaking, remote sensing methods for bathymetry retrieval are based on the ratio of different bands. The conversion of the band ratio between two visible bands to river flow depth involves a correction coefficient. In the band ratio algorithm, this coefficient is called the attenuation coefficient. Although the remote sensing methods are much more convenient than the field methods, some field measurements are still required in order to determine the attenuation coefficients. In other words, it entails a comparison between depth results from images and field measurements of depth.

Although the comparison does not require extensive field measurements of depth from the river in question, a reasonable amount of depth samples from the field are necessary to achieve statistical confidence. This is because the regression analysis used for estimating the correlations between optical variables and in site flow depth.

It is highly desirable to eliminate the necessity of sending operators and executing logistics to a river site, and to save a great amount of expense and time. The objectives of this study are to

(1) introduce new methodology that does not depend on field measurements for mapping bathymetry. Field measurements of depth do not enter the bathymetry analysis from satellite images.
(2) evaluate the accuracy of the new methodology. Field measurements of depth are used for the purpose of validation.

The new methodology will accelerate the process of bathymetry acquisition, making it possible to build a flow depth database in a much shorter time in comparison to the conventional methods for measuring depth. The new methodology will reduce the costs of bathymetry acquisition from the conventional methods.

1.2 The scope of this study

The contents of this thesis are organized into five chapters:

- Chapter One provides the background and motivation of conducting this study, along with a brief description of the differences between the new methods discussed in this thesis and the previous methods reported in the literature.
- Chapter Two is a review of the literature about the evolution of satellite images. The focus is on remote sensing approaches to bathymetry retrieval and on earlier attempts at developing ratio algorithms in the analytical approaches.
- Chapter Three introduces the collection of required data in this study, the analytical methods for calculating depth from multi-spectral high-resolution satellite images, and the implementation of the methods to the Nicolet River.
- Chapter Four presents the results of flow depth from the analytical methods using satellite images as input. It also includes validation of the methods through a comparison of the results with field measurements from previous studies. The chapter demonstrates the importance of allowing for contributing correction factors.
- Chapter Five addresses the improvement of methods from this study, compared to earlier studies of bathymetry. It discusses differences and similarities in parameters and their values between this study and the earlier studies. It also points out limitations and the need of further studies.
- Chapter Six gives highlights of conclusions from this study.

1.3 Contributions of this study

This study has made the following contributions:

- Present an analytical model for river bathymetry using high-resolution satellite images as input. Avoid using field measurements of depth as input to the analytical model.
- Use multispectral images for bathymetry, as opposed to single band data.
- Demonstrate the importance of radiometric corrections.

- Extend relationships from studies of oceanic and coastal-water bathymetry to calculate absorption and backscattering effects of river water.

2 LITERATURE REVIEW

2.1 Remote sensing

2.1.1 Definition of remote sensing

The ability to take images from features on the Earth from long distances enables humans to study patterns and the possible relations between these features. It has made it possible to investigate Earth's surface features and measure changes in them in massive size, depth, and area over time, which is more effortless but sometimes impossible for many features by other means. Airborne and satellite images can offer a variety of information that extracting them requires a high level of knowledge. The knowledge of processing information from an image that is taken at a long distance by satellite or airborne images is generally called remote sensing knowledge (Campbell and Wynne. 2011).

2.1.2 Evolution of satellites for remote sensing

Remote sensing consists of different methods for Earth observation. It includes aerial photography, Unmanned Aerial Vehicles (UAVs), geophysical prospection, and satellite remote sensing (Agapiou and Lysandrou 2015). This section of the thesis provides some information for the evolution in the technology of satellites for remote sensing purposes.

In July 1972, in order to respond to the new need for resource management and earth science, the U.S. Geological Survey (USGS) in collaboration with National Aeronautics and Space Administration (NASA), launched the first satellite designed to observe the surface of Earth. This satellite was first called Earth Resources Technology Satellite-A (ERTS-A), but later its name changed to Landsat1. It had a 5-years mission to take images from 75% of the earth's surface with two instruments; Return Beam Vidicon (RBV) and Multispectral Scanner (MSS). These instruments could provide images in four bands: green, red, and two near-infra-red bands (United States Geological Survey 1997). At first, RBV was selected to be the primary instrument; however, after testing MSS sensors for the first time, MSS was chosen to be the primary instrument.

In January 1975, the second Landsat named Earth Resource Technology Satellite-B was launched for the same purpose. Landsat-2 like Landsat-1 had an 80-meter ground resolution for both RBV and MSS instruments. In contrast to Landsat-1, the MSS instrument was more practical, and RBV was rarely used for engineering purposes rather than scientific analysis. This satellite became non-functional in February 1982. Landsat-3 was the last generation of Landsat satellites that used the same RBV and MSS instruments with almost the same features (United States Geological Survey 1997). The most significant change for this generation in comparison to the previous ones is the improvement in the resolution of the RBV instrument to 40-meter resolution.

All generations of Landsat satellites up to now use the same band function for MSS instruments. They use the green band to set out shallow water areas and highlight sediment-laden water and the red band to demonstrate cultural features. The first Near-infrared band was used to discriminate vegetation lands from landforms and water; and the second Near-infrared band was practical for pointing out vegetation, the boundary between land and water, and landforms in the condition that more penetration was required due to the hazy atmosphere (United States Geological Survey 1997).

Earth observation continued by lunching Landsat-4 and Landsat-5 in July 1982 and March 1984, respectively. For these satellites, RBV sensors are replaced by Thermic Mapper (TM) sensors (Barsi et al. 2007). This new sensor in company with the MSS sensor is used to detect visible reflected radiance and Infrared wavelengths. The MSS sensors on Landsat 4 and 5 are similar to Landsat 1, 2 and 3. TM sensor also gives the satellites the ability to provide information for the Thermal band with a spatial resolution of 120 m, Mid-Infrared, two Near-Infrared bands and visible bands with 30 m higher resolution. Landsat-7 and Landsat-8 are known as the latest launched satellites after failure in Landsat-6 in this series. For Landsat 7 an improved version of the TM sensor named Enhanced Thematic Mapper Plus (ETM+) was replaced to deliver 8-bit images (Barsi et al. 2007).

In addition to satellite images, Light Detection and Ranging (LiDAR) makes it possible to have higher resolution digital elevation data for coastal and inter-tidal zone areas to create Digital Elevation Model (DEM) (Quadros, Collier, and Fraser 2008). This system includes a Global Positioning System (GPS), a high frequency laser and an Inertial Measurement Unit (IMU) (Quadros et al. 2008). In the case of shallow waters where depth is less than 12 meters, airborne LiDAR can determine water depth. It uses a laser beam in green spectrum to penetrate in shallow water from a low-altitude aircraft (Wang et al. 2015). However, LiDAR bathymetry is initially built for near shore waters and its accuracy depends on several factors such as flying height, GPS geometry, water turbulence, IMU update and measurement frequency (Quadros et al. 2008).

Commercial satellites like QuickBird, GeoEye-1, WorldView-1, WorldView-2, WorldView-3 are newly used for bathymetry. They can provide images with better resolution (less than 2 meters) with multispectral bands. High-resolution images give us the opportunity of using images from these satellites for purpose of river bathymetry. We will discuss more the features of WorldView-2 and WorldView-3 satellite images in the following chapter.

2.1.3 Future developments of satellites for bathymetry

Existing global satellites provide images and Digital Elevation Models; however, they are not precise enough for studying river depth. The upcoming Surface Water and Ocean Topography (SWOT) satellite will provide elevation of surface water (Langhorst et al. 2019). This mission is a partnership between space agencies of countries including the United States of America, Canada, the United Kingdom, and France. The objective of this mission is to record high vertical accuracy, and high spatial resolution topography data with the main instrument called a Ka-band Radar Interferometer (KaRIn) for the scientific purpose of oceanography and hydrology, as well as measuring storage changes in the surface of water bodies and estimate discharges in the large rivers around the world (Vaze et al. 2018). This mission in terms of rivers wider than 100-200 m can identify many long stream topographic features by repeating measurement (Langhorst et al. 2019). SWOT will offer high frequency and high-resolution maps of elevation for surface water bodies around the world and will provide an exceptional opportunity to deal with issue requires knowledge of hydrology measurements (Vaze et al. 2018).

2.2 Challenges of using satellite images

One of the main issues in the analysis of satellite images for remote sensing process in water areas is unclear and falsify nature of multi-spectral images. This issue comes from a low level of contrast in water areas. This issue leaves scientists to process the raw data from multi-spectral images and perform an extra level of analysis for bathymetry that leads to the water attenuation coefficient (Bierwirth, Lee, and Burne 1993). Moreover, radiation before reaching to bottom level of water needs to pass through layers of atmosphere and water. These layers absorb and backscatter the depth reflectance; consequently, it leads to putting an additional signal in the reflectance spectrum; therefore, these added signals should also be considered in the optical process of raw data (Bierwirth et al. 1993).

Additionally, surface and bottom reflectance add another source of clutter for the classification of recorded reflectance. Radiometric correction techniques have provided the possibility of discrimination of water depth and bottom of other features once the data is recorded digitally from multi-spectral scanners (Lyzenga 1978).

2.3 Ratio algorithm: A proposed method to response challenges

In order to address some of the mentioned challenges, researchers in the field of remote sensing have been trying to present new approaches to suggest a solution for them. In this respect, many algorithms have been offered, some of which prepared for a specific case study, and others work with one particular instrument of a satellite. However, the process of evolution of algorithms leads to preparing more genialized algorithms for different case studies. In the following, a brief review of attempts in response to challenges is given. They lead to a concept of a ratio algorithm.

Polcyn, Brown, and Sattinger (1970) made an early effort to prepare a suggestion for the effect of bottom reflectance in the bathymetry process of waterbodies. Experimental investigations showed that there is a possibility to introduce an algorithm that can eliminate bottom reflectance. Based on the results, Polcyn et al. (1970) found that the ratio of the bottom reflectance for a pair of wavelength bands for different bottom types within a site of study is the same. This means in a scene, for bottom types A and B (Equation 1) the ratio for reflectance of wavelength bands 1 and 2 remains constant.

$$[1] \quad \frac{r_{A1}}{r_{A2}} = \frac{r_{B1}}{r_{B2}} = R_b$$

where R_b is substrate reflectance. Then the following equation is suggested as one of the primary algorithms for bathymetry:

$$[2] \quad z = \frac{1}{f(k_1 - k_2)}\left[\ln(\frac{K_1}{K_2}) - \ln(\frac{R}{R_b})\right]$$

Equation 2 also considers attenuation coefficient (k_i) (m^{-1}), geometric factor (f), ratio of bottom reflectance (R), and K_i as constant for solar irradiance. Bathymetry with the band ratio method relies on the assumption that in a scene for a couple of bands, the ratio reflectance is equal for different bottom reflectance. The challenge is to ensure the relationship is valid for the numerous water types and various bottom reflectance (Shah, Deshmukh, and Sinha 2020).

Later, Lyzenga (1978) showed that minimum information of a scene is required for the ratio method because this technique only requires information of two bands, and it does not use all reflectance spectral information. He suggested a two-band linear solution that corrects bottom reflectance; also, he pointed out that light scattering has the same depth dependency as bottom reflectance and recommended Equation 3 as a depth transmission equation to set a more general, linear equation

[3] $Z = c_0 + c_i X_i + c_j X_j$

and,

[4] $X_i = \ln(L_i - L_{si})$

where L_i and L_{si} are defined as radiance for wavelength (i) ($Wm^{-2}\mu m^{-1}sr^{-1}$), and deep-water radiance including scattering effect, respectively.

One of the main problems for the proposed Equations 3 was the use of radiance instead of reflectance. It is more convenient to use reflectance for the depth algorithms since reflectance, in contrast to radiance, is a measurable quantity; it is independent of light illumination condition; finally, it is the ratio of emergent relative radiance to total radiance so, it is proportional to radiance (Jupp 1989).

[5] $R_E = (e^{-2kz})R_b + (1 - e^{-2kz})R_W$

where R_E, R_W, and R_b represent effective reflectance of the water body, reflectance from molecules and particles in the water column, and substrate reflectance, respectively. Also, k is known as attenuation coefficient for depth (z).

Later Bierwirth et al. (1993) used Equation 5 for the images captured by Landsat 5 TM sensor from Hamelin Pool in Shark Bay, Western Australia. In their study, Equation 5 is transformed to Equation 6 with an assumption that due to suspended loads and biological considerations, R_W remains constant through the depth

[6] $R_E - R_W = R_\lambda = e^{-2kz}R_b$

where $R_E - R_W$ is equal to the reflectance-corrected Landsat data (R_λ). Bierwirth et al. (1993) showed from satellite Landsat 5, it is possible to obtain water depth through different wavelengths (λ) from Equation 6 by taking the logarithm of Equation 5 (Bierwirth et al. 1993)

[7] $Ln(R_\lambda) = Ln(R_{b\lambda}) - 2k_i z$

Up to this point as stated before, the technique of using the ratio of two bands in the algorithms helps separate the albedo effect from variation in the depth through an optical system; however, it has some limitations in the terms of depth penetration and turbidity.

Stumpf et al. (2003) studied penetration rate for different wavelengths of images from satellite IKONOS for coral reef environments. Their study approved wavelengths have a different absorption rate once they enter into water and they can penetrate to a certain depth. Bands like green with a higher absorption rate can go less in-depth and decreases proportionally faster than a blue band with a lower absorption rate. Consequently, when considering the reflectance ratio between two bands, moving toward deeper water causes an increase in this ratio for these two bands. At the same time, the ratio transform recovers the effect of different bottoms. Stumpf et al. (2003) also used Lyzenga (1978) formula and Beer's Law (indicates that light passes through water, it loses its intensity and it attenuates exponentially with depth) in Stumpf et al.'s (2003) study to experience Equation 8

$$[8] \quad \mathrm{Z} = n_1 \frac{\ln\left(\mathrm{nR_w}(\lambda_\mathrm{i})\right)}{\ln\left(\mathrm{nR_w}(\lambda_\mathrm{j})\right)} - n_0$$

In Equation 8, n is a constant to guarantee both logarithms are always positive. n_0 and n_1 represent offset for depth zero and tunable constant, respectively. The advantage of Stumpf et al.'s (2003) method is it does not require subtraction of any optical signal for image correction. In comparison to previous methods, it only requires two coefficients; however, to get the values for coefficients Stumpf et al. (2003) compared image depth value to chart depth from the beach. This means to complete Equation 8 for satellite bathymetry, having some field measurement is necessary to get the values for constants.

Continuing previous efforts to provide a general framework for bathymetry ratio algorithm, Legleiter, Roberts, and Lawrence (2009) conducted another experimental study along three reaches of Soda Butte Creek a tributary to the Lamar River located on Yellowstone Park, USA. In the first place like previous studies, measured bathymetry data were collected from another source of study, then from an image of the area of study, a series of data of radiometric quantities in the different forms of radiance or reflectance was gathered. The goal is to identify a pair of wavelengths among various options to use in the Optimal Band Ratio Analysis (OBRA) to identify the best combination of pair of wavelengths that determines the depth from image radiometric properties. Moreover, in this approach, the proposed algorithm also evaluated for the parameters that may affect results; especially ground reflectance and bottom reflectance, suspended sediment, and water surface roughness. To begin with, Legleiter et al. (2009) used an algorithm suggested by Philpot (1989) for the total radiance at the sensor

[9] $L_T = E_d CT(R_{bo} - R_c)\,exp(-KZ) + E_d CTR_c + T\rho L_k + L_p$

Equation 9 consists of parameters that have the potential to effective bathymetry from a multispectral image. The first one is E_d which is known as downwelling solar irradiance ($Wm^{-2}nm^{-1}$), then C represents a constant for transmission across air-water interface. T is transmittance of the atmosphere, R_{bo} and R_c are bottom reflectance of the streambed and volume reflectance of the water column respectively. L_p and L_K are also known as path radiance from the atmosphere and diffuse sky radiance ($Wm^{-2}\mu m^{-1}sr^{-1}$) respectively. The correlation between the depth (Z) and radiance of each band shows as depth increases, total radiance for bands decreases. Although the bottom of the river has some effect on the radiance, for a wavelength with stronger attenuation, measured radiance decreases faster due to increasing the depth than a wavelength with weaker attenuation. Therefore, the difference between the two total radiance of two bands escalates and the ratio between two bands (L_{T1}/L_{T2}) increase as well (Legleiter et al. 2009). Another point that is considered is the effect of bottom radiance is dominant to other terms in Equation 9. Therefore, taking the natural logarithm of the ratio between two total radiance of wavelengths from Equation 9 results in a variable for natural algorithm ratio between two bands called Y for bathymetric mapping

$$[10] \quad Y = \ln\left[\frac{L_{T1}}{L_{T2}}\right] \approx \ln\left[\frac{L_{b1}}{L_{b2}}\right] = \ln\left[\frac{E_{d1}C_1T_1(R_{b1} - R_{c1})}{E_{d2}C_2T_2(R_{b2} - R_{c2})}\right] - d(K_1 - K_2)$$

A constant as form of $A = \ln[E_{d1}C_1T_1/E_{d2}C_2T_2]$ is considered for terms that are constant in an image. Thus, simplified form of Equation 10 is:

$$[11] \quad Z \approx (K_2 - K_1)z + \ln\left[\frac{(R_{b1} - R_{c1}}{(R_{b2} - R_{c2})}\right]$$

Equation11 shows the relation between Z as image-derived depth and measured water depth (z). The slope term in this relation represents the effective attenuation coefficient (m^{-1}) between two bands (K_2-K_1) (Legleiter et al. 2009). The last equation represents an innovative ratio algorithm that provides the possibility of depth determination once a correlation between depth and some sample measured water depth is recognized. In the following, more discussion is for the application of these ratio algorithms in the various case of water bodies.

2.4 Application of satellite image in bathymetry

Although the primary use of Earth observation satellites has been monitoring land and its' changes, taking water bodies under surveillance has started from the early launched satellites for the Earth observation. As time passes, the evolution of satellites by means of higher technology has been offering higher accurate images with new instruments that provide more resolution and a more comprehensive range of wavelengths to keep wetlands under surveillance. At first, since satellite images cannot provide high-resolution images, and in the case of sea and oceans, changes for the depth in length are not intense in comparison to rivers, the bathymetry of those locations was in the center of attention. However, whenever satellites deliver an acceptable image resolution, river bathymetry through satellite images is considered as one of the possibilities for river bathymetry.

2.4.1 Satellite images and ocean, sea and lake bathymetry

Electromagnetic waves may be affected by various factors such as absorption, atmosphere effect, sun elevation, and scatter. Baban (1993) started to investigate the effects of the atmosphere on electromagnetic waves on either the available algorism or establishing regression algorithm. For this reason, he selected Derwentwater located in the heart of the English Lake District, Cumbria as his case of study. This lake has 2.2 km long, 2 km wide and a maximum depth of 22 m. Also, he assumed some other factors like wind, antecedent rainfall, and wave actions in the lake do not affect the bathymetry process. There were two reasons for selecting this lake; first, the availability of some measured data. Second, gradual changes in the depth of this river. For the imagery data source, two images were captured from this lake. The first one was from Landsat 4-MSS on 28 May 1977 and the second one was from Landsat 4-TM on 15 February 1985. Before utilizing any method for bathymetry retrieval, the suspended load was examined to make sure it does not affect the ground reflectance. Baban (1993) used three methods, all based on regression between different models and obtained depth from Landsat 4 images. In one of them, a relation between ground reflected data and the bands MSS4 and TM1 used to obtain a bathymetry map of the lake. Moreover, the mean attenuation coefficient (K) of water is calculated based on the average values of K in the five different points with known depth. The results of this comparison method reported 99% satisfaction.

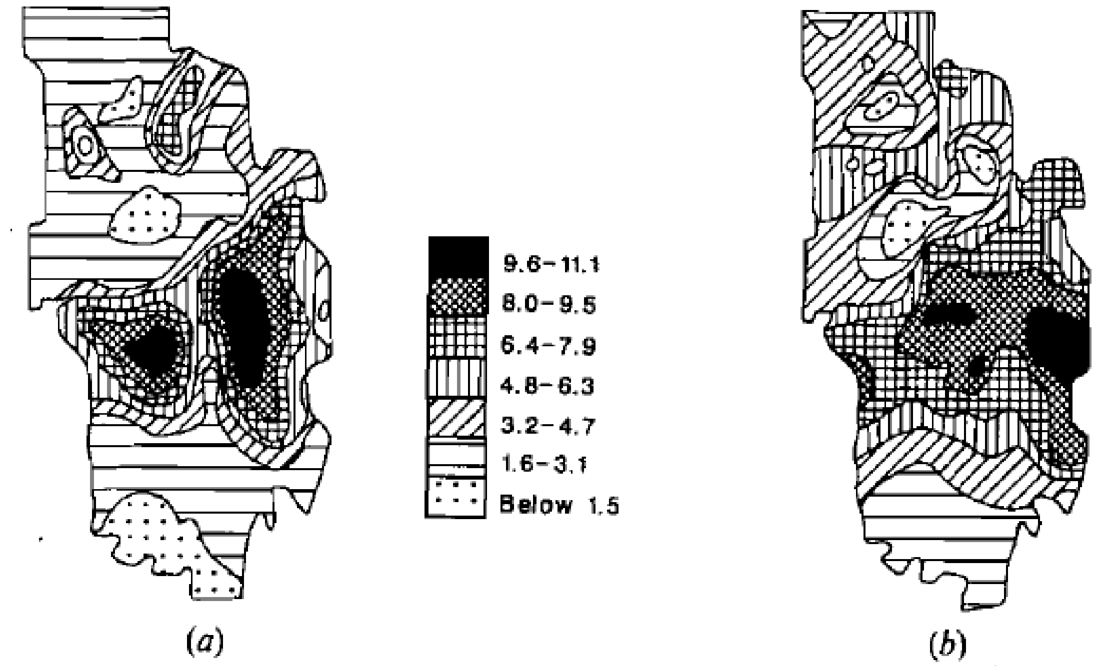

Figure 1: Derwentwater lake bathymetry map (a) with multispectral scanner (MSS) regression equation (b) with Thermic Mapper (TM) regression equation (Baban 1993)

Information concerning water depth near coastal lines in the harbor is essential for the shipping industry, navigation, and port management. Nevertheless, providing bathymetry maps requires spending a considerable amount of time and money in these locations (Tripathi and Rao 2002). For this reason, Tripathi and Rao (2002) used an Indian satellite named IRS-1D LISS–III for bathymetry of Kakinada Bay, India. Images from this satellite are multispectral linear include two visible bands and one near-infrared (NIR) in 23.5 m resolution and one in the short ware infrared (SWIR) in 70.5 m resolution. On the other side, an echo sounder and GPS were employed to detect the depth for 36 points in the harbor with the exact location of the sample points. Correlation between the reflectance data of each band and the depth at measured points for all four bands is provided in Figure 2.

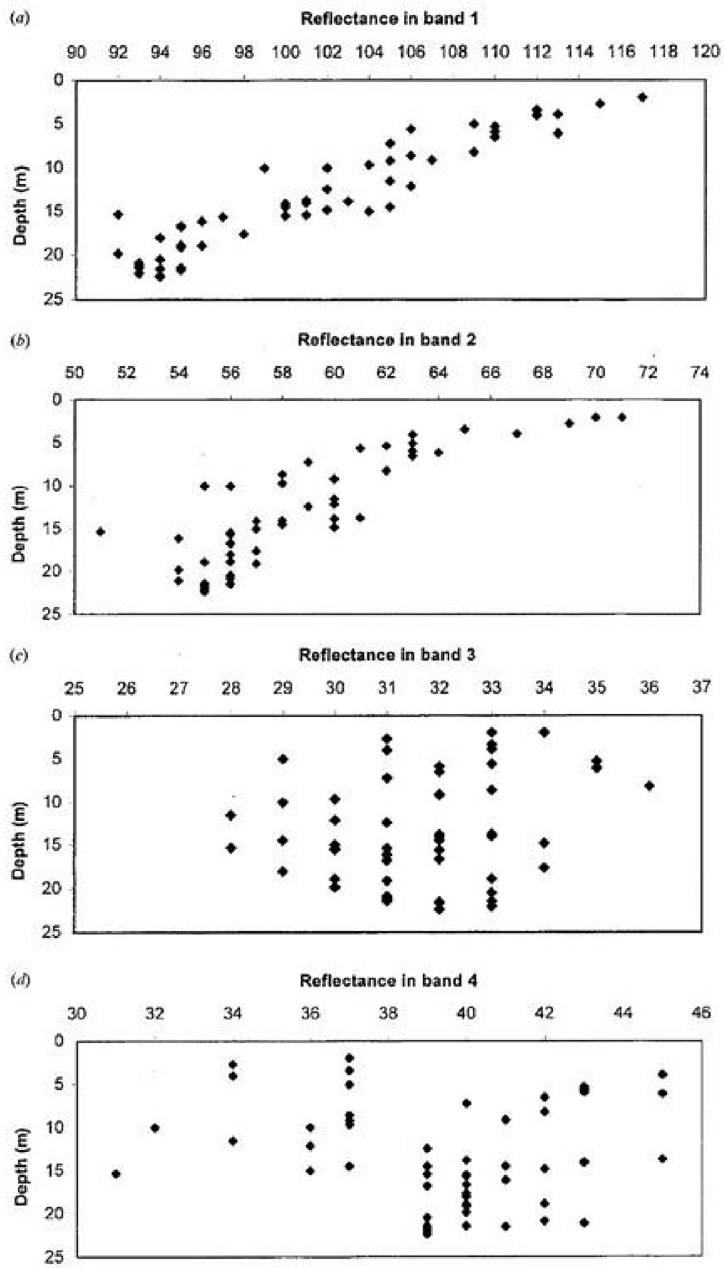

Figure 2: changes reported by Tripathi and Rao (2002) in reflectance of bands with measured lake depth in (a) band 1; (b) band 2; (c) band 3; (d) band 4

A least square regression was performed between sampled measured depth to all four reflected wavelengths in a model to detect the best correlation between measured data with the estimated depth. Tripathi and Rao (2002) concluded possibility of error with the average absolute percentage of 9.4676 for band 1 which provides the best link between estimated depth and field measurements.

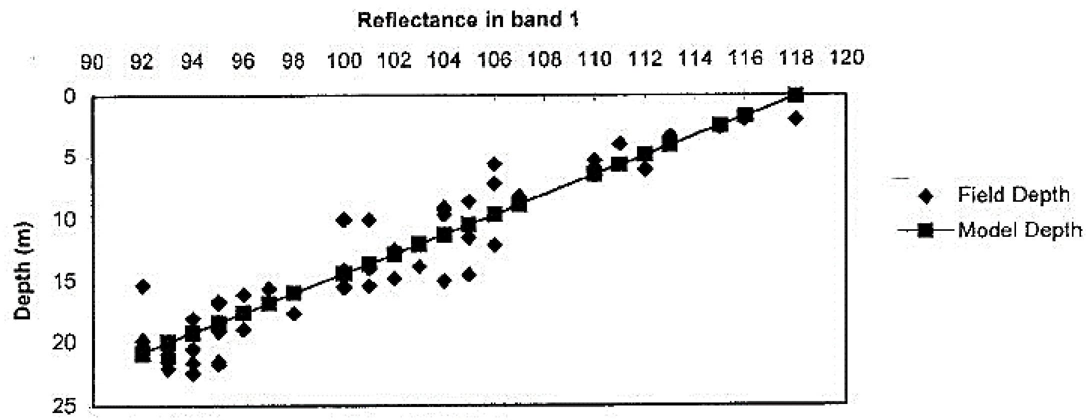

Figure 3: A least square correlation between the depths from reflected band 1 with field measurements (Tripathi and Rao 2002)

2.4.2 Satellite images and river bathymetry

Knowing channel morphology is an essential element in the understanding of river behavior; especially in terms of sediment transfer and flow. However, having this information is not a simple task in some cases because there are some restrictions such as logistical constraints and lack of investigations that hold the process of river bathymetry. In recent decades, satellites provide the possibility of capturing high-resolution multispectral images from the Earth. Consequently, similar to previous studies in the case of vast water bodies like lakes, sea or shallow coastal zones, satellite images can be used for bathymetry.

One of the interesting case studies conducted for a case of two shallow bed gravel rivers in the Yellowstone National Park, USA with high resolution satellite images for WorldView-2. This study was performed by Legleiter and Overstreet (2012) dividing into two sections. This the first part which is the field measurements, bed topography of those rivers surveyed by use of real-time kinematic (RTK) GPS receiver. For deeper parts of rivers GPS receiver was attached to a cataraft while it is connected to echo sounder to measure river depth. Additionally, to check accuracy of measured depth, Acoustic Doppler Current Profiler (ADCP) deployed to provide supplementary measured depth. Legleiter and Overstreet (2012) also recorded reflectance from the above surface of water by Analytical Spectral Devices (ASD) and used these measurements to calculated the diffuse attenuation coefficient (K_d) (m^{-1}). These values were used to calculated depth for the discrete measured points based on Equation 9

$$[12] \quad \Delta z(\lambda) = -\frac{1}{2K_d(\lambda)} \ln\left[1 - \frac{\Delta L_N(\lambda)}{L_B(\lambda)} \exp\{2K_d(\lambda) z_0\}\right]$$

here $\Delta z(\lambda)$ is known as the smallest detectable changes in depth from initial depth z_0, and $\Delta L_N(\lambda)$ and $L_B(\lambda)$ are sensor's noise equivalent and portion of total radiance related to bottom ($Wm^{-2}\mu m^{-1}sr^{-1}$).

For the second part, Legleiter and Overstreet (2012) followed a producer based on ratio algorithm that previously offered by Legleiter et al. (2009) as below:

$$[13] \quad X = Ln\left[\frac{R(\lambda_1)}{R(\lambda_2)}\right]$$

Analysis was performed to find the best pair of wavelengths that describe the best linear relation between Y and z. Results indicate the possibility of the bathymetry of a shallow gravel-bed river through satellite images. Also, it showed panchromatic and pan-sharpened multispectral images that provide a higher resolution; do not lead to more reliable depth estimation. Moreover, bathymetry for the pool locations was less reliable, and it may be a consequence of saturation of the radiance signal (Legleiter and Overstreet 2012).

Up to this point, the discussion has been for the regression relationship between a single band ratio and measured depth. However, more studies show that single band ratio characteristics may not be strong enough to reflect water depth, especially in the presence of some confusing factors such as river bed type, dissolved water elements or water surface roughness. To solve this issue an approach named Sample-specific Multiple band Ratio Technique for Satellite-Derived Bathymetry (SMART-SDB) is proposed to divide a river into different partition of spectral feature space (Niroumand-Jadidi, Bovolo, and Bruzzone 2020). In this approach a satellite image with n spectral ban (b_1, b_2, …, b_n) assumed to be a n dimensional image where every band represents one dimension. Therefore, for every two bands log transformed ratio feature (TR) is defined as follow (Niroumand-Jadidi et al. 2020):

$$[14] \quad TR_{ij}(x) = \ln\frac{b_i(x)}{b_j(x)}$$

where i = {1, 2, ..., n-1} and j = {i+1, i+2, …, n}

unlike Optical Band Ratio Analysis (OBRA) that uses a pair of bands which can provide the highest (R^2) in least-squares regression method, here bathymetry obtained from the second order polynomial of TR_{ij} as follow:

$$[15]\quad d(x) = f\left(TR_{ij}(x)\right) = a_1 TR_{ij}^2(x) + a_2 TR_{ij}(x) + a_3$$

where constaints like a_1, a_2, and a_3 can be estimated form in site measured samples. By considering all possible band ratios for n band image, the total number of ratio models (U) will be:

$$[16]\quad U = \frac{n!}{(n-2)! \times 2!}$$

To get the best estimation of water depth form multi band image, Niroumand-Jadidi et al. (2020) build up more ratio band models via sample-specific K-NN analysis to improve the results in comparision to single band ratio. These models are creatd by dividing "image X" into two X^t and X^p sets where the depth is known for the X^t samples and the depth is unknown for X^p samples

$$[17]\quad d(x) = \frac{\sum_{k=1}^{K}\left(\frac{1}{dist(X^t,X^p)} \times f_k(R^{opt}(x)\right)}{\sum_{K=1}^{K}\frac{1}{dist(X^t,X^p)}}$$

where f $(R^{opt}(x))$ comes from:

$$[18]\quad f\left(R^{opt}(x)\right) = argmin\left\{\left|f(TR_{ij} - z(x)\right|\right\}$$

The proposed method provide the eater depth by considering several band ratio to take account confusion factor and increase accuracy of model compared to single band ratio model. Although a significant improvement happens in the remote sensing technique to estimate water depth from a satellite image, so far, all the available methods rely on field measurements. Meaning all proposed ratio algorithms for bathymetry through satellite images consist of unknown constants which the only solution to determine numbers for them is comparing estimated depth from ratio algorithm to measured depth. In other words, the comparison method between two depth values from band ratio calculation and site measurements reveals constants values. As a result, river bathymetry from remote sensing techniques depends on field measurements.

Niroumand-Jadidi and Vitti (2016) used the ratio algorithm (Equation 13) in optimal band ratio analysis of high-resolution satellite images. They used images from the WorldView-3 satellite along with in-situ measurements of the Sarca River in Italy. They employed all possible pairs of bands to find the log-linear transfer, and they measured depth. Parente and Pepe (2018) also used high-resolution images from the WorldView-3 satellite. They extracted physical Earth surface parameters through radiometric corrections of optical sensors of WorldView-3. They developed a linear regression between two reflectance bands value and ground measurements in three scenarios, involving the ratio of the coastal blue band to the yellow band, the ratio of the green band to the blue band and the ratio of the coastal blue band to the green band. They obtained a correlation between the parameters.

For bathymetry retrieval from satellite images of seas and oceans, some analytical and semi-analytical methods do not rely on or make little use of field measurements for calibration. These methods take input of low or medium resolution satellite images, which are adequate for those water bodies because the spatial changes in the depth are not as considerable as in rivers. Satellite remote sensing technology provides increasingly high-resolution images. Inspired by the analytical methods for sea and ocean studies, a new approach to river bathymetry investigation is discussed in the next chapter of this thesis. The new approach does not require any field measurements for river bathymetry determination.

3 METHODOLOGY

3.1 Study area

The Nicolet River is one of the tributaries of the Saint Lawrence River located in Quebec. The site of this study is the Nicolet River between Norte-Dame-de-Ham Town and Victoriaville. This reach of the river has a length of 25 km, with pairs of deflectors. The surrounding lands of the river channel are mainly agricultural lands. Some areas are covered by coniferous trees, which impose a canopy on the river channel. The riverbed materials are mainly dolomite, limestone, shale, clays and sands (Ng 2005).

Figure 4: Field site locations within the Nicolet River watershed.

A decline in fish populations, especially the populations of two spices: brown trout *(Sa/mo trutta)* and brook trout *(Sa/velin us fontinalis),* puts the Nicolet River on the list of rivers with a risk of losing biological diversity (Ng 2005). Therefore, a set of deflectors were installed to reduce bank erosion and keep pools as habitants for endangered fish species. Some studies show that in general, introducing deflectors does not have negative effects on bed sediment size, channel sinuosity and hydraulic roughness and that it increases the chance of pool habitat availability approximately five times (Shields, Cooper, and Knight 1995). Initially, in 1994, a set of wooden deflectors were installed; however, these structures were washed by a massive flood a couple of years later (Carré, Biron, and Gaskin 2007). In the second attempt, in 1997, a set of boulders as deflectors were installed upstream, and then deflectors were added downstream (Carré et al. 2007).

In the Hydrometric Database (HYDAT), there is only one hydrometric station in the Nicolet River (Station number: 02OD003). This station is located at 5.8 km downstream of the mouth of the Bulstrode River flowing into the Nicolet River, downstream Victoriaville. Historical hydrometric data from this station covers a period of 38 years from 1966 to 2004. Observations of discharges near the deflectors in the Nicolet River gave a 9-to-1 ratio between the discharge at the station and that near the deflectors (Ng 2005).

3.2 Data collection

To determine the flow depths at certain locations and further depth contours for the site of study, we collected satellite images and data from other sources, and processed them. High-resolution satellite images were the primary data. The data processing also included some available in-situ depth measurements. Information of the data sources used in this study is given below.

3.2.1 High resolution satellite images

Images from the WorldView2 and WorlView3 satellites provide acceptable resolutions in different bands for river bathymetry retrieval. For this purpose, we modified analytical and semi-analytical methods from sea and ocean studies and applied the methods to the high-resolution satellite images. It is understood that compared to seas and oceans, rivers have more considerable changes in depth across channel cross sections.

3.2.1.1 WorldView-2 Satellite:

This satellite was launched on October 8, 2009. It has provided images for use since January 4, 2010. Commercially available images include nine spectral bands: panchromatic, CoastalBlue, blue, green, yellow, red, red edge, Near Infrared1 (NIR1), and Near Infrared2 (NIR2). The resolutions are 0.5 m for panchromatic images, and 2 m for multispectral images (Updike and Comp 2010).

On September 16, 2015, the WorldView-2 satellite captured an image from the area of this study, with no cloud coverage, at off-Nadir of 25.5° and Sun elevation of 46.3°. The final image that covered the whole area of this study was obtained by assembling several images. The individual images covered only a part of the area, with multispectral bands and a resolution of 2 m × 2 m pixel. Specifications of each band consisted of maximum bandwidth, minimum bandwidth, effective bandwidth, radiance gain and solar irradiance specific for the final image, as listed in Table 1.

Table 1: Specifications of WorldView-2 image bands.

Band	Min bandwidth (nm)	Max bandwidth (nm)	Effective bandwidth (μm)	Radiance gain
CoastalBlue	400.00	450.00	0.473	0.1923
Blue	450.00	510.00	0.0543	0.2316
Green	510.00	580.00	0.0630	0.1530
Yellow	585.00	625.00	0.0374	0.1342
Red	630.00	690.00	0.0574	0.1914
RedEdge	705.00	745.00	0.0393	0.1139
NIR1	770.00	895.00	0.0989	0.1231
NIR2	860.00	1040.00	0.0996	0.0892

3.2.1.2 WorldView-3 Satellite:

Since August 13, 2014, the WorldView-3 satellite has stayed at an altitude of 617 km. Similar to the WorldView-2 satellite, this satellite can produce images of the Earth in nine bands, including panchromatic, coastal blue, blue, green, yellow, red, red edge, NIR1, and NIR2. Commercially available images from this satellite offer good resolutions: 0.3 for panchromatic images; 1.2 m for multispectral images (Kuester 2016). On May 20, 2016, this satellite captured multiple images of the Nicolet River. We assembled them to generate a uniform image for a 25-km reach of the river under clear sky condition, at off-Nadir of 26.5° and Sun elevation of 62.3°. Band specifications of the captured images are listed in Table 2.

Table 2: Specifications of WorldView-3 image bands.

Band	Min bandwidth (nm)	Max bandwidth (nm)	Effective bandwidth (μm)	Radiance gain
CoastalBlue	400.00	450.00	0.0405	0.290882
Blue	450.00	510.00	0.0540	0.305240
Green	510.00	580.00	0.0618	0.195538
Yellow	585.00	625.00	0.0381	0.167912
Red	630.00	690.00	0.0585	0.169537
RedEdge	705.00	745.00	0.0387	0.159961
NIR1	770.00	895.00	0.1004	0.115925
NIR2	860.00	1040.00	0.0889	0.119327

3.2.2 Digital elevation model (DEM)

The images provided by both the WorldView-2 and WordView-3 satellites are not geo-referenced. It is necessary to add geo-reference to the images in order to obtain the correct position of every pixel on the ground. We accomplished the geo-referencing process by using a digital elevation model (DEM) provided by U.S. Geological Survey's (USGS) Earth Exploration. DEMs are "arrays of regularly spaced elevation values referenced horizontally either to a Universal Transverse Mercator (UTM) projection or to a geographic coordinate system (U.S. Geological Survey 1998). The Shuttle Radar Topography Mission (SRTM) prepared the DEM for the Nicole River for September 23, 2014. The DEM covered the entire site of this study.

3.2.3 Data from field survey

The main purpose of this study is to explore the feasibility and accuracy of the analytical approach to mapping shallow river bathymetry without the need of field measurements. This approach is in contrast to previous studies that use a correlation/comparison between field measurements of depth and retrieved depths from processing satellite images. In this study, we used field measurements for the purpose of assessing the accuracy of the analytical approach. We made a comparison between analytical results and field measurements.

The measurements were made during a field survey in 2005, reported in the study of Carré et al. (2007). The purpose of their study was to reveal the effects of deflectors installed in the Nicolet River on sediment transport, flow velocity, and bed topography. The field survey was conducted on a 250-m long section of the river, including two sets of paired deflectors. By using the depth measurements, a DME was generated for the river section near the two sets of deflectors. According to this DEM, the depth of the Nicolet River varied from 96.5 m, in a pool right between and in the front of the deflectors, to 99.7 m in the vicinity of the river shoreline. In Figure 5, the bathymetry around two of the deflectors is shown in DEM values, and in Figure 6, details around one of them are plotted.

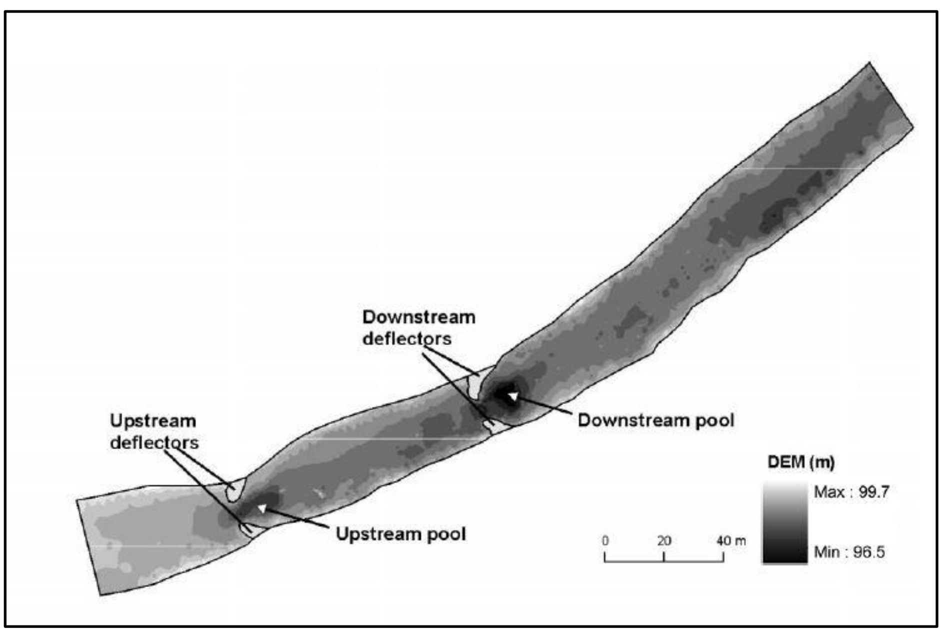

Figure 5: Digital Elevation model around two of deflectors.

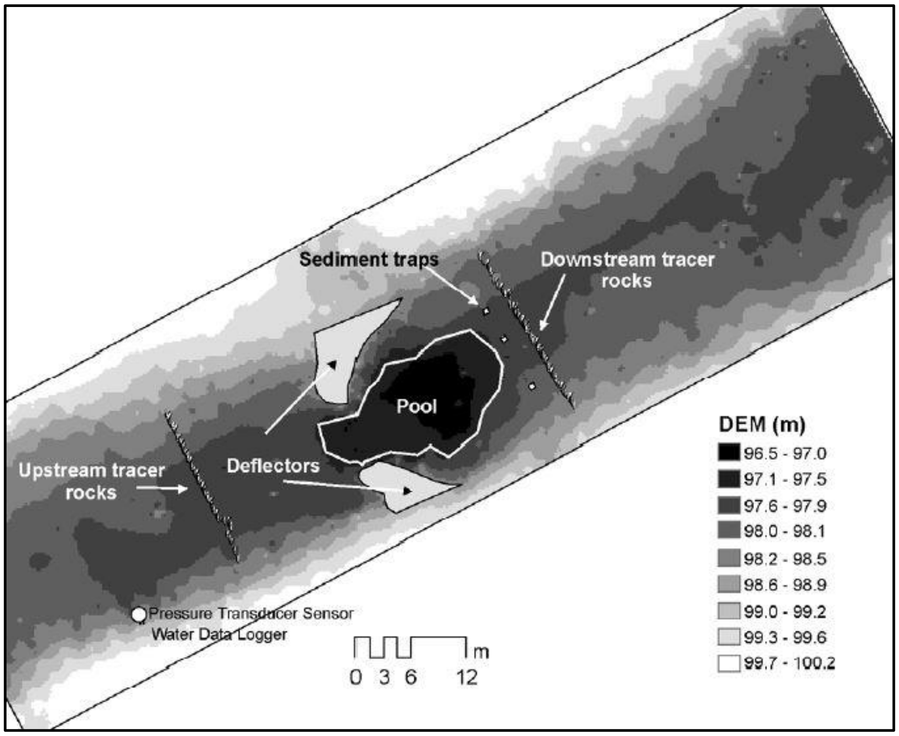

Figure 6: Digital Elevation model in the neighboring area of the downstream deflector.

Figure 7: Detailed locations of the deflectors in the Nicolet River (Image downloaded from Google Earth on March 1, 2021).

3.3 Geometric correction

The raw images from WordView-2 and WordView-3 did not come with geometric corrections. To associate each pixel on the images with the real position, a process for geometric corrections is essential. This process started from the DEM downloaded from the USGS. Two major issues needed to be dealt with: The first issue was that one part of the river channel in the study area is within one DEM map, whereas another part is within a different DEM map. Therefore, if corrections were based on just one of these two DEM maps, the final results would split the river channel into two sections: One section had newly corrected geographic positions, and the other did not. This issue was resolved by merging the two DEM maps into one uniform DEM, and then geo-referencing satellite images were applied based on the uniform DEM. In Figure 8, the river channel location in DEMs before and after merging is illustrated.

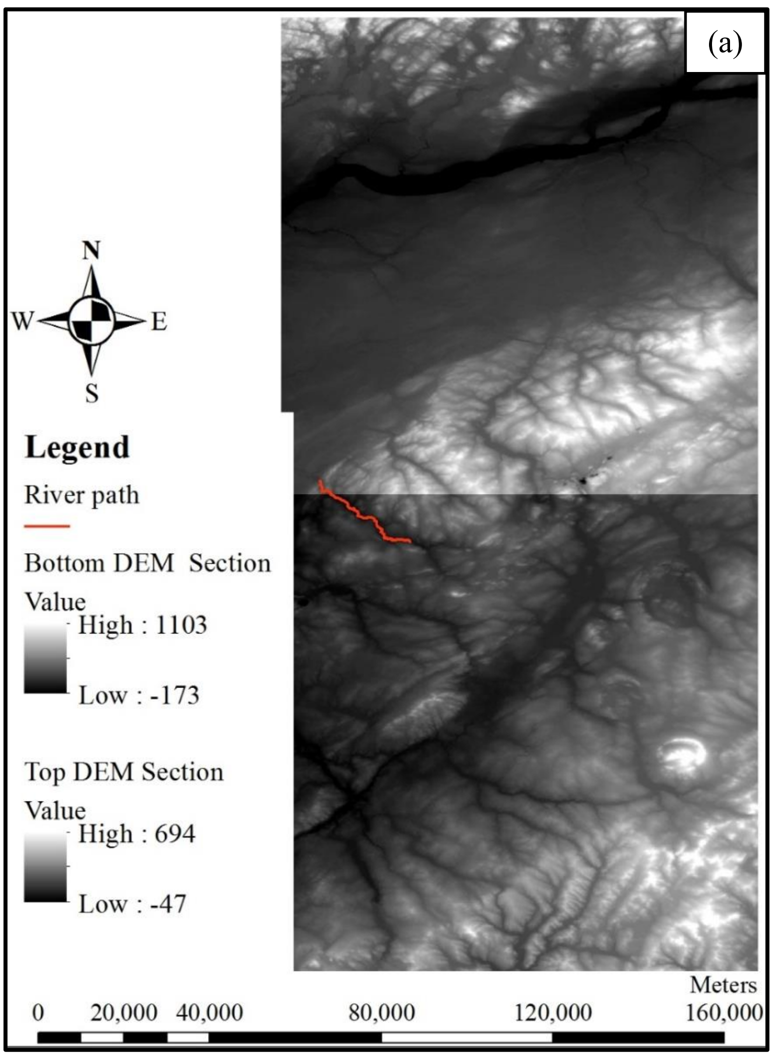

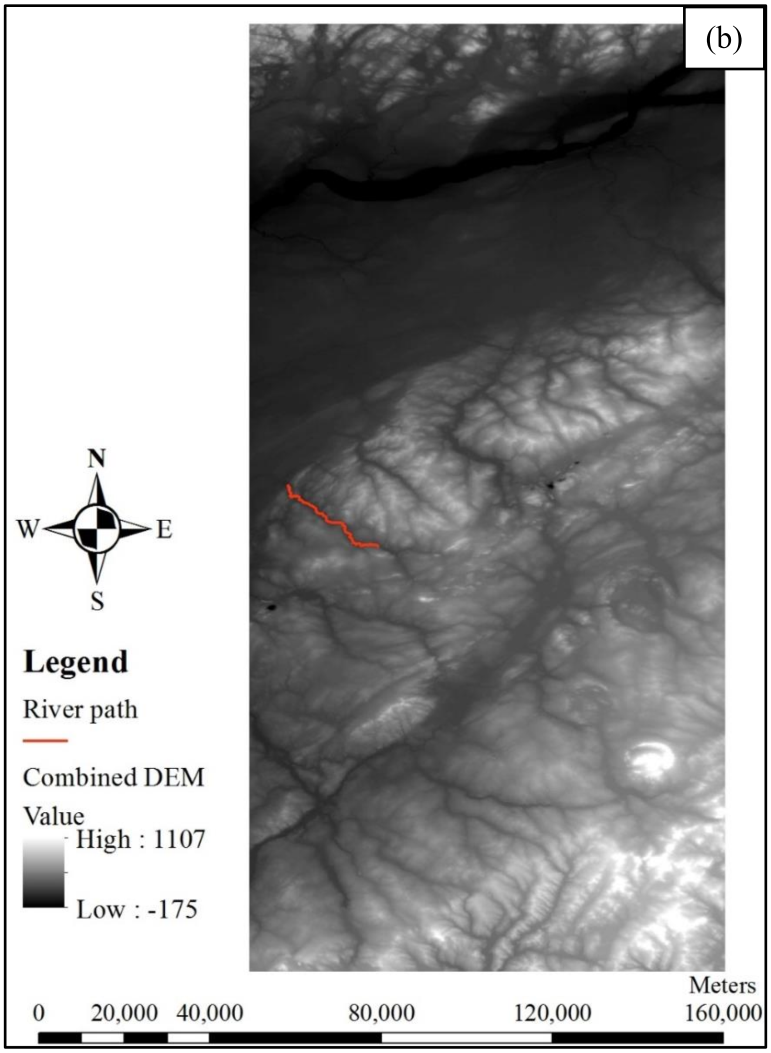

Figure 8: Digital elevation models (DEMs): a) before merging; b) Combined DEMs.

The second issue was that the dates of satellite images are different from those of the DEM. So, there may be some changes in the riverbank position between the times when the images were captured and for which the DEM were constructed. This issue was resolved by using data from google earth. For the dates when the two satellite images were captured (September 16, 2015 for WorldView-2; May 20, 2016 for WordView-3), images of the study area were obtained from google earth. The river channel centreline was delineated on the google earth image and was then compared to the geometrically corrected satellite images. This was an important part of the validation process. In Figures 9 and 10, the positions of the river channel centreline before and after geometric corrections are shown.

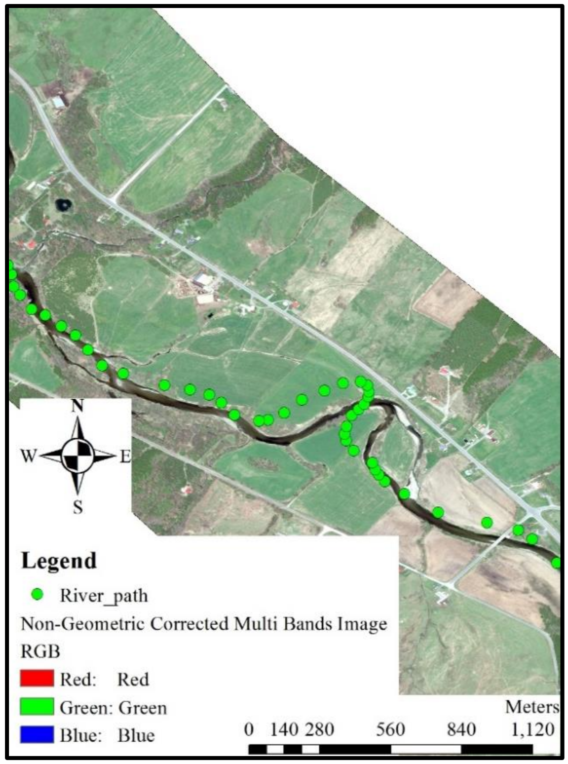

Figure 9: The Nicolet River before geometric correction.

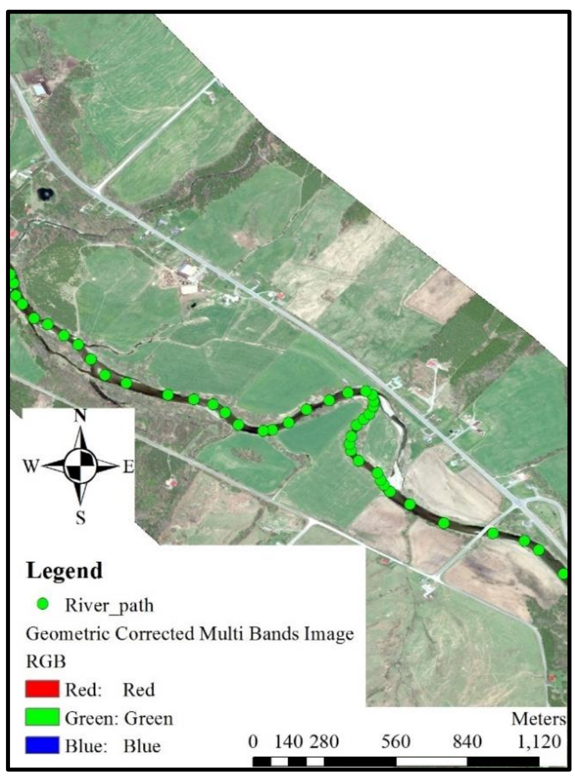

Figure 10: The Nicolet River after geometric correction.

3.4 Bathymetry retrieval

In this study, the methods for bathymetry retrieval include two main components. The first component was an exploration of the best algorithm for bathymetry calculations. The second component focused on eliminations/reductions of errors in calculation equations as well as in input data to the calculations. We used available tools such as radiometric correction.

3.4.1 Ratio algorithm

Lambert-Beer's law states that a beam of light passing into water transfers its energy to molecules; consequently, its intensity falls gradually. This attenuation occurs due to the absorption and scattering properties of molecules. The attenuation is regulated by attenuation properties, and it is influenced by the optical properties of that medium. The model equation is given by

$$[19] \quad \mathrm{I(z)} = \mathrm{I_0 e^{-kz}}$$

where I(z) is the intensity of light at the depth z; I_0 is the intensity of light before entering the water; k is an attenuation coefficient. A band with a shorter wavelength, defined as the distance between two adjacent peaks of a wave, has a higher frequency, which possesses a higher level of energy and consequently can penetrate deeper in the water column and can retain higher intensity. The visible spectrum (wavelengths between 400 and 700 nm) includes the bands CoastalBlue, Blue, Green, Yellow and Red; the band CoastalBlue has the shortest wavelength and thus the highest intensity, whereas the band Red has the longest wavelength and therefore the lowest intensity.

Satellite images consist of pixels. In remote sensing, light intensity for each band reflects the value of that band for every pixel of an image. Thus, the light intensity in Equation 19 can be replaced by pixel value, also called the Digital Number, DN, of that pixel recorded by a satellite sensor. In our analysis of the satellite images, the intensity of light is substituted by DN

$$[20] \quad \mathrm{DN} = \mathrm{DN_0 e^{-kz}}$$

where DN_0 is the pixel value before light enters water. The problem is that satellite images do not provide information about DN_0 since optical lenses of satellites only record discrete values of radiance of bands. We eliminated DN_0 by considering the ratio between two band values at identical depth

[21] $$\frac{DN_1}{DN_2} = \frac{DN_0}{DN_0} \times \frac{e^{-k_1 z}}{e^{-k_2 z}}$$

[22] $$Ln\left(\frac{DN_1}{DN_2}\right) = Ln\left(\frac{e^{-k_1 z}}{e^{-k_2 z}}\right)$$

[23] $$Z = \frac{1}{(K_2 - K_1)} \ln \frac{DN_1}{DN_2}$$

In Equation 23, $\overline{K} = K_2 - K_1$ is called the effective attenuation coefficient. With this equation, from a multi-spectral satellite image, it is possible to determine the depth through computing the natural logarithm ratio of two bands if the attenuation coefficient number is known.

There are two methods for determining the values of the attenuation coefficient. One of the methods, previously used in both river and ocean studies, is based on field surveys. The method made a comparison between observed water depth and the ratio of bands. In this method, an adequate number of points is used to build a linear regression relationship between water depth and pixel brightness. This is the conventional correlation technique used by many researchers. For example, Harada and Li (2018) used the method for the bathymetry of the Goulais River in Ontario. They employed high-resolution images from the GeoEye-1 and Pleiades-1A satellites. They selected 35 data points for a field survey of river depth and obtained a linear regression relation between the data points and the natural logarithm ratio of two bands (red and green) to determine the attenuation coefficient.

Another method originated from ocean and coastal water studies. The method does not use input of field measurements to the estimation of the attenuation coefficient. This coefficient is calculated from semi-analytical and analytical formula. The calculations are based on the radiative transfer theory, in which such optical properties of a water body as solar zenith, absorption coefficient, backscattering coefficient, and boundary condition plays a significant role, discussed below.

3.4.1.1 Diffuse attenuation coefficient

In remote sensing of coastal areas and oceans, the radiative transfer equation contains the effective diffuse attenuation coefficient, $\overline{K}_d$ (m^{-1}), as a correlation between absorption coefficients, a, backscattering coefficients, b_b, and solar zenith angle, Θ_s (Z. Lee et al. 2005). For ocean and coastal areas, Lee et al. (2005) suggested a multiband Quasi-Analytical Algorithm (QAA) and formulated $\overline{K}_d$ in Equation 24:

$$[24]\ \overline{K}_d = m_0 a + m_1(1 - m_2 e^{-m_3 a}) b_b$$

where the attenuation constants are given by: $m_0 = 1 + 0.005\Theta$, $m_1 = 4.18$, $m_2 = 0.52$, and $m_3 = 10.8$. The values remain the same for all different wavelengths and water depths, with or without suspended materials.

This semi-analytical method is more complicated with regard to determining the values of the absorption coefficient and backscattering coefficient, than the empirical method. For values of these coefficients, it is necessary to utilise equations from empirical and analytical studies, along with radiometric analysis of satellite images, in order to implement Equation 24 and subsequently depth retrieval.

3.4.1.2 Absorption Coefficient

The absorption coefficient (m^{-1}) indicates how far a wavelength can penetrate into water before it loses all energy due to absorption. This coefficient is not constant for different environments and particularly depends on the strength of a wavelength. In Lee, Carder, and Arnone (2002), the total absorption coefficient varied for each wavelength, λ; it depended on the absorption coefficient for pure water $a_w(\lambda)$ (m^{-1}), and the absorption of suspended loads $\Delta a(\lambda)$ (m^{-1}) for that wavelength, given by:

$$[25]\ a(\lambda) = a_w(\lambda) + \Delta a(\lambda)$$

In the analytical method, it is necessary to use a wavelength as the reference wavelength and to calculate the other wavelength coefficients based on the reference.

Wavelengths equal to or longer than 550 nm contribute little to absorption energy by suspended load (Lee et al. 2002). As in ocean studies, in the case of the Nicolet River, $\lambda_0 = 555$ nm in the green band is considered as the reference wavelength. Therefore, the total absorption coefficient is related to the absorption energy of pure water as:

$$[26]\ a(\lambda) = a_w(\lambda)$$

Equation 26 is a general form for absorption equation. For the reference band, an empirical relation is given by

$$[27]\ a(555) = 0.0596 + 0.2[a(440) - 0.01]$$

Here, a(440) is an intermediate parameter for the derivation of a(555) (Z. Lee et al. 2005)

$$[28]\ \mathrm{a}(440) = \exp(-0.2 - 1.4 + 0.2\rho^2)$$

where ρ is a calcutation factor to describe absorbtion:

$$[29]\ \rho = \ln\{\mathrm{r_{rs}}(440)/\mathrm{r_{rs}}(555)]$$

In Equation 29, r_{rs} is called below-surface remote-sensing reflectance. It is part of any image radiometric characteristics. For each wavelength, the value of r_{rs} is calculated from the above-surface remote-sensing reflectance R_{rs} as

$$[30]\ \mathrm{r_{rs}} = \mathrm{R_{rs}}/(0.52 + 1.7\mathrm{R_{rs}})$$

Lee et al. (2002) suggested a general form of absorption formula for other wavelengths.

$$[31]\quad a(\lambda) = \frac{[1\text{-}\mathrm{u}(\lambda)][\mathrm{b_{bw}}(\lambda)+\mathrm{b_{bp}}(\lambda)]}{\mathrm{u}(\lambda)}$$

where $b_{bw}(\lambda)$ and $b_{bp}(\lambda)$ are the backscattering coefficients; u(λ) is the ratio of the backscattering coefficient to the sum of absorption and backscattering coefficients.

3.4.1.3 Backscattering Coefficients

Once a beam of light enters a water body, particles scatter photons of light. The backscattering coefficient is defined as the differential scattering cross-section per unit volume for a scattering angle of 180° (Chen, Zagzebski, and Madsen 1993). The total backscattering coefficient, b_b (m^{-1}), is the sum of the backscattering coefficient of suspended particles b_{bp} (m^{-1}) and the backscattering coefficient of pure seawater b_{bw} (m^{-1})

$$[32]\ b_b = b_{bp} + b_{bw}$$

To obtain a value of b_{bw} for any wavelength, Morel (1974) suggested an equation under the standard atmospheric pressure and water temperature 20 °C:

$$[33]\quad b_{bw} = 3.5 * 10^{-3}\left(\frac{\lambda}{450}\right)^{-4.32}$$

Buiteveld, Hakvoort, and Donze (1994) made measurements and used the Einstein-Smoluchowski equations to calculate the scattering coefficient in pure water in a temperature range of 2.5 °C and 45 °C. In Tables 3 and 4, values of b_w for center wavelength of Worldview-2 and WorldView-3 satellites as calculated from Equation 33, are listed, along with a comparison of the calculated values with experimental results of Buiteveld et al. (1994), for the visible spectrum. For the green band, instead of using the center wavelength of that band, the calculation used the reference band (555nm). The caculated values compare reasonably well with the experimenal data, especially for wavelengths larger than 555 nm, for which small suspended materials have least effects on absorption coefficient.

Table 3: Scattering coefficient of pure water for the visible spectrum of WorldView-2.

Band	Center wavelength (nm)	Morel 1974 (m^{-1})	Buiteveld 1994 (m^{-1})
Coastal Blue	427.4	0.004372	0.0041
Blue	478	0.002696	0.0025
Green	555	0.001414	0.0014
Yellow	608	0.000953	0.0009
Red	659	0.000673	0.0007

Table 4: Scattering coefficient of pure water for the visible spectrum of WorldView-3.

Band	Center wavelength (nm)	Morel 1974 (m^{-1})	Buiteveld 1994 (m^{-1})
CoastalBlue	427.4	0.0044	0.0041
Blue	481.9	0.0026	0.0025
Green	555	0.0014	0.0014
Yellow	604.3	0.0010	0.0010
Red	660.1	0.0007	0.0007

Under real-world condition of a water body, there are some dissolved and suspended loads in the water, which affects the scattering coefficient. To allow for this effect, Lee et al. (2002) suggested an equation for the backscattering coefficient of suspended particles. In the same way as for the absorption coefficient, the backscattering coefficient of suspended particles for any wavelength is calculated based on the coefficent of the reference wavelength (λ = 555 nm).

[34] $$b_{bp}(\lambda) = b_{bp}(555) * \left(\frac{555}{\lambda}\right)^{Y}$$

where Y is Spectral power for particles in backscattering coefficient:

[35] $$Y = 2.2\left\{1 - 1.2\exp\left[-0.9\frac{r_{rs}(440)}{r_{rs}(555)}\right]\right\}$$

and backscattering coefficient of suspended particles for λ=555nm is:

[36] $$b_{bp}(555) = \frac{u(5555) * a(555)}{1 - u(555)} - b_{bw}(555)$$

3.4.1.4 u ratio

Note that u is defined as the ratio of the backscattering coefficient to the sum of absorption and backscattering coefficients, given by:

[37] $$u = \frac{b_b}{a + b_b}$$

According to Lee et al. (2002), it is possible to rewrite this equation in terms of $r_{rs}(\lambda)$, which removes the dependency on the absorption or backscattering coefficients

$$[38] \quad u = \frac{-g_0 + [(g_0)^2 + 4g_1 r_{rs}(\lambda)]^{\frac{1}{2}}}{2g_1}$$

where g_0 and g_1 are constants taken as 0.0895 and 0.1247, respectively.

Up to this point, all necessary equations and methods for the required constants and coefficients that appear in Equation 24 have been discussed. It is ready for us to test depth determination that does not need input of field measurements. Apart from the band ratio directly related to the radiance for each band, the only parameter that is related to the attenuation coefficient and that requires quantification from the radiance of satellite images, is below-surface remote-sensing reflectance r_{rs}. More discussion of this aspect will be given after the radiometric process and band selection.

3.4.2 Radiometric correction and top-of-atmosphere spectral radiance

Radiance is defined as variables recorded by satellite observation sensors. The sensors measure the light passing through the atmosphere, where some of the light scatter due to atmospheric character. Moreover, the atmosphere absorbs some of the light and results in a reduction of recorded radiance. Before using satellite images for bathymetry calculations, radiometric corrections should be applied to eliminate atmosphere effects.

Radiometric corrections are divided into two main categories: relative correction; absolute correction. The relative correction standardises multiple-satellite scenes to each other using available supplementary information like ground reference data, climate data, and illumination geometry in order to remove fundamental radiometric problems like stripe noises, defective lines and non-uniformity (Janzen, Fredeen, and Wheate 2006). In Figure 11, a desert image before and after relative radiometric correction for the WorldView-2 Pan band I shown. Generally speaking, for every satellite image, there is a Metadata file that indicates radiometric, geometric and band specifications of that image. We used a Metadata file provided by Apollo Mapping Co. (provider of images). Both the WorldView-2 and WorldView-3 satellite images were delivered with relative radiometrical corrected image pixels.

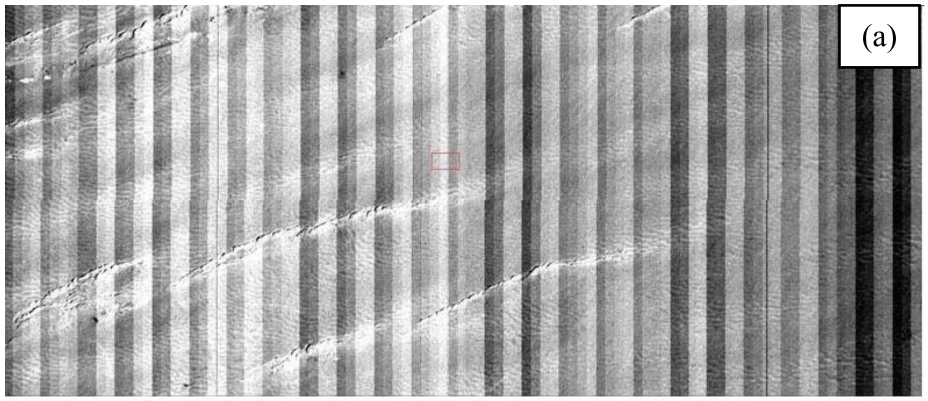

Figure 11: : Image of a desert from WorldView-2: a) Before relative radiometric correction; b) after relative radiometric correction (Updike and Comp 2010)

The absolute correction transforms digital numbers of pixels (radiance numbers) to reflectance values. The radiative transfer model depends on the combination of atmospheric correction and geometry coefficients. Information of these coefficients includes the date of the scene and sensor properties. Compared to the relative correction, the absolute radiometric correction requires more theoretical consideration and computational operations (Janzen et al. 2006), and thus is more complicated. Values of the absolute correction factor are given in the Metadata file of images for the Nicolet River. These factors are referred to as “absCalfactor” in this file.

To obtain reflectance values from the radiance of each band, the first step is to calculate the top-of-atmosphere spectral radiance. Digital radiances recorded from the conversion instrument depend on the amount of spectral radiance captured by telescope aperture and are directly linked to telescope spectral transmission, filters, and spectral quantum efficiency. Accordingly, pixel data from the WorldView-2 and WorldView-3 satellte are unique and not comparable to other satellites sensors (Kuester 2016). We need to use specific formulations to calculate top-of-atmosphere radiance. Equation 39 gives L as the top-of-atmosphere radiance (W-m^{-2}-$sr^{-1}$$\mu m^{-1}$), where q_{pixel} is radiometrically corrected pixel value, absCalfator is the absolute radiometric calibration factor (W-m^{-2}-$sr^{-1}$$count^{-1}$), and $\Delta\lambda_{band}$ is the effective bandwidth for WorldView-2 satellite (Updike and Comp 2010)

$$[39] \quad L_{\lambda} = \frac{\text{absCalfactor}.\, q_{\text{pixel}}}{\Delta\lambda_{\text{Band}}}$$

where abscalfactor is 0.009094740, 0.01257455, 0.009636360, 0.005018950, 0.01098462, 0.004475790, 0.01217436, and 0.008884210, for the eight bands, respectively. Almost the same procedures were followed for the top-of-atmosphere radiance of WorldView-3. The only difference was there were two more factors for calibration and adjustments: radiance gain, and offset added to Equation 39 (Kuester 2016)

$$[40] \quad L_{\lambda} = G * DN * \left(\frac{\text{absCalfactor}}{\Delta\lambda_{\text{Band}}}\right) + O$$

where abscalfactor is 0.01397474, 0.01772364, 0.01316364, 0.006720000, 0.01020364, 0.006063160, 0.01170909, and 0.01034947, for the eight bands, respectively. G and O stand for gain and offset values of pixels. The logic behind adding the gain and offset factors for WorldView-3 images comes from atmospheric correction. Assume that in a histogram of pixel brightness of a wavelength, there are some pixel values near zero. If the observed pixel brightness did not start from zero (e.g for water pixels), it is assumed to be the consequence of atmospheric contributions in recorded data. Therefore, this offset should be substracted from histograms with an offset greater than zero for the entire image in order to remove most of the atmospheric effects. In Table 5, the offset values for each band for WorldView-3 satellite images are listed.

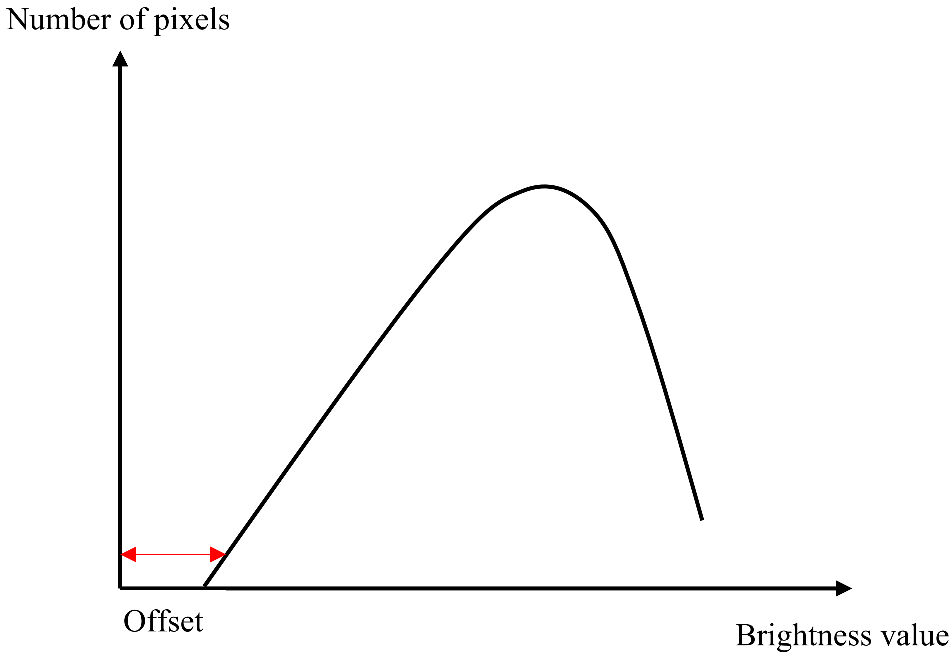

Figure 12: Effect of offset on brightness histogram.

Table 5: Band offset values for Worldview-3 image.

Band	offset
CoastalBlue	-7.070
Blue	-4.253
Green	-2.633
Yellow	-2.074
Red	-1.807
RedEdge	-2.633
NIR1	-3.406
NIR2	-2.258

Another coefficient in Equation 40 is the gain. This coefficient is the second important factor in reducing the atmosphere effect. As shown in Figure 13, the ideal correlation between ground scene brightness and image brightness should be a line at 45°, but in real satellite images, this line has a deviation from 45°. As a result, to correct the deviation, the gain coefficient is defined as the slope of the sensor response line.

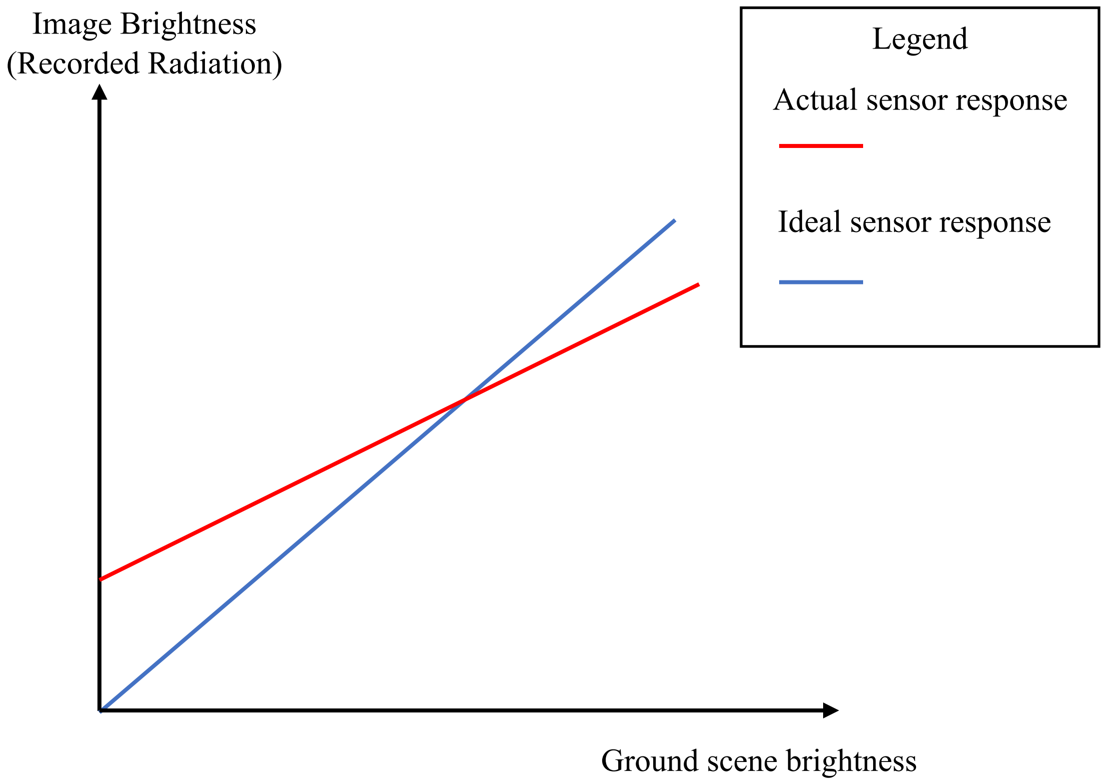

Figure 13: Comparison between ideal and actual sensor response.

3.5 Converting from top-of-atmosphere radiance to top-of- atmosphere reflectance

The reflectance of materials is defined as the ratio of light leaving materials to the amount of light that strikes them. In some remote sensing applications, it is possible to use radiance and reflectance interchangeably. Nevertheless, the preference is to use the reflectance of light, because it is an inherent property of the materials and it has no dependency on light illumination or the position of objects. For this reason, it is conventional to take some steps to convert radiance to reflectance.

Noted in Updike and Comp (2010) and Kuester (2016) for the WorldView-2 and WorldView-3 satellites, respectively, the same model as suggested by NASA has been used to correct moderate resolution imaging spectroradiometer (MODIS) images since the Earth observation system for terra and aua platforms started. This model indicates that top-of-atmosphere reflectance, $\rho(TOA)_\lambda$, requires input of the solar zenith angle, Θ_s, Earth-Sun astronomical distance, d, and band averaged solar exoatmospheric irradiance, E_λ ($Wm^{-2}\mu m^{-1}$).

$$[41] \quad \rho(\mathrm{TOA})\lambda = \frac{L_\lambda d^2 \pi}{E_\lambda \cos\Theta_s}$$

3.5.1 The Earth-Sun distance

The Earth-sun distance is about 150 million kilometres, which is equal to one astronomical unit (AU). The exact distance between the Earth and the Sun at the time when an image is captured is calculated as follows. First, time Julian Day (JD) is calculated based on the time of the captured image. This time is provided in the Metadata file in Coordinated Universal Time (UTC) in the format of "YYYY_MM_DDThh:mm:ss:ddddddZ". The first four digits (YYYY) give the year, the next two digits give the month (MM), followed by the date "DD". The "T" is just a literal to separate the date from time. Letters "hh", "mm", "ss", "dddddd" mean the hour, minute, seconds and fraction of a second respectively. Finally, Z shows zero-hour offset (UTC). These numbers for WorldView-2 is highlighted as **2015-09-16T16:11:42.254439Z,** and for WorldView-3 as **2016-05-20T15:52:58.346343Z.** To determine JD, first, it is necessary to calculate Universal Time

$$[42] \quad \mathrm{UT} = \mathrm{hh} + \frac{\mathrm{mm}}{60} + \frac{\mathrm{ss.dddddd}}{3600}$$

For dates that are not in January or February, Meeus (1998) recommended to use the following equations

$$[43] \quad \mathrm{A} = \mathrm{int}\left(\frac{\mathrm{year}}{100}\right)$$

$$[44] \quad \mathrm{B} = 2 - \mathrm{A} + \mathrm{int}\left(\frac{\mathrm{A}}{4}\right)$$

$$[45] \quad \mathrm{JD} = \mathrm{int}[365.25 * (\mathrm{year} + 4716)] + \mathrm{int}[30.6001 * (\mathrm{month} + 1)] + \mathrm{day} + \frac{\mathrm{UT}}{24} + \mathrm{B} - 1524.5$$

In Equations 43 to 45, the word "int" means only use the integer part of the number. JD is then used in the following equations to calculate Earth-Sun distance at the time of the captured images

$$[46] \quad \mathrm{D} = \mathrm{JD} - 2451545$$

$$[47] \quad \mathrm{g} = 357.529 + 0.98560028 * \mathrm{D}$$

Equation 48 provides the Earh-sun distance ($\mathrm{d_{ES}}$):

$$[48] \quad \mathrm{d_{ES}} = 1.00014 - 0.01671\cos(\mathrm{g}) - 0.00014\cos(2\mathrm{g})$$

Table 6: Summary of Earth-Sun calculated numbers for both satellites

Coefficients	WorldView-2	WorldView-3
UT	2984.638	5595.837
A	20.000	20.000
B	-13.000	-13.000
JD	2457405.86	2457774.660
D	5860.860	6229.660
g	6133.994	-5782.425
($\mathrm{d_{ES}}$)	0.984	0.985

Acceptable values for the Earth-Sun distance should be between 0.983AU and 1.017AU for both satellites (Kuester 2016). The results given in Table 6 indicate that the values are in the correct range.

3.5.2 Solar zenith angle

The solar zenith angle is an angle between the Sun and the vertical. This angle is obtained from subtracting the degree of mean solar elevation provided in the Metadata file from 90°. If an image strip is less than 13.4 km, it is not required to calculate the zenith angle for every single pixel, and only one angle for solar zenith is acceptable. For the area of this study, the length (25 km) is bigger than the standard length of 13.4 km. However, since only one Mean Sun Elevation was available, we assumed that the solar zenith angle remains constant over the entire length of the images. The results are presented in Table 7.

Table 7: Mean Sun Elevation and solar zenith angle of images

Angle	WorldView-2	WorldView-3
Mean Sun Elevation	46.3	62.3
solar zenith angle (Θ_s)	43.7	27.7

3.5.3 Solar exoatmospheric irradiance

Instruments installed on the WorldView-2 and WorldView-3 satellites are sensitive to a wide range of wavelengths from the visible light spectrum to near-infrared. In this range, solar radiation has a significant effect on recorded wavelengths. Thus, to calculate the reflectance of each wavelength, it is necessary to consider this effect by creating a model of irradiance. One of these models used for both satellites is provided by the World Radiation Center (WRC), on the basis of a series of measurements (Kuester 2016). As shown in Figure 14, according to this model, solar irradiance peaks around 450 nm for the coastalBlue and blue band and then declines toward longer wavelengths. In Table 8, values of solar irradiance for each wavelength of satellites are listed.

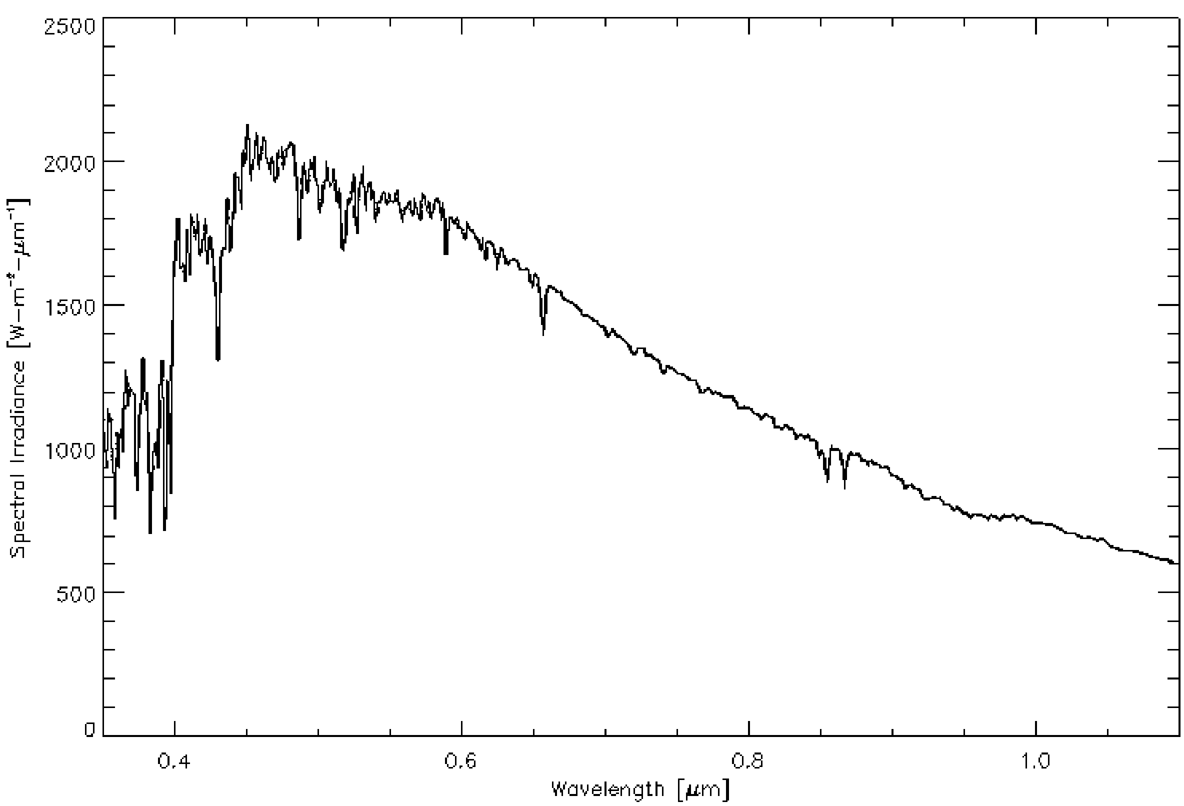

Figure 14: Solar irradiance of wavelengths for WorldView-2 and 3 (Kuester 2016)

Table 8: Values for solar irradiance in World Radiation Center (WRC) model

Spectral Band	Solar irradiance ($Wm^{-2}\mu m^{-1}$)	
	WorldView-2	WorldView-3
CoastalBlue	1758.22	1743.81
Blue	1974.24	1971.48
Green	1856.41	1856.26
Yellow	1738.48	1749.40
Red	1559.46	1555.11
RedEdge	1342.07	1343.95
NIR1	1069.73	1071.98
NIR2	861.29	863.30

3.6 Vertical datum

The retrieved bathymetry for the Nicolet River is validated using field measurements, reported in Carré et al. (2007). Their bathymetry data is given in geoid height. Accordingly, for a comparison, we must convert the bathymetry to geoid height. The conversion needs a reference point called the vertical datum in order to change river flow depth to geoid height and achieves acceptable accuracy.

Natural Resources of Canada (NRC) developed a vertical reference system across Canada. In this system, mean sea level (MSL) observations from five tide gauges: Yarmouth and Halifax in the Atlantic Ocean, Pointe-au-Père in the St-Lawrence River, and Vancouver and Prince-Rupert in the Pacific Ocean, were used to define the Canadian Geodetic Vertical Datum of 1928 (CGVD28). The tidal datums at those gauges serve as the reference for measurements of elevations across the country (Natural Resources Canada 2020). Subsequently, to decrease costs and respond to new requirements, this system was replaced by the Canadian Geodetic Vertical Datum of 2013 (CGVD2013) in November 2013. This replacement increases the accuracy at some points, and on the national scale, it corrects some distortions of the previous reference system from -65 cm to +55 cm. The difference between CGVD28 and CGVD2013 shows up once a resolution of 20 cm or less in ten km is required. In this case, the difference between the two reference systems must be taken into account. In the case of a precision better than 2 cm required, adding an offset value would be sufficient (Natural Resources Canada 2020).

For all reference systems, MSL Height, often known as Orthometric height, H (m), is a vertical height of a point of interest to a reference surface called the geoid. NRC provides Orthometric height through benchmarks as a reference surface for topographic elevations. Also, geoid height, N, gives the difference between Orthometric height and reference ellipsoid, h (m), where the ellipsoid does not have any physical meaning

$$[49]\ H = \begin{cases} h + N\,;\ if\ N > h \\ h - N\,;\ if\ N < h \end{cases}$$

Geoid height can be either positive or negative. If it points above the ellipsoid, it will be positive; otherwise, it will be negative. The Metadata file of images provides the ellipsoid height of four corner pixels in abbreviation form. In Table 9, explanations and values relevant to each satellite image are given.

Table 9: Ellipsoid height for four-pixel corners of satellite image

File name	explanation	Ellipsoid value for WorldView-2 image	Ellipsoid value for WorldView-3 image
URHAE	Height above the ellipse of the upper right pixel of the image	160.20	161.45
ULHAE	Height above the Ellipse of the upper left pixel of the image	160.20	161.45
LRHAE	Height above the ellipse of the lower right pixel of the image	160.20	161.45
LLHAE	Height above the ellipse of the lower left pixel of the image	160.20	161.45

As shown in Table 9, all the corners of each image have the same ellipsoid height; consequently, there must be a unique value for the overall image pixels. According to Equation 49, determining the orthometric height is the only missing value to calculate geoid height for each pixel. A search through benchmarks near the deflectors to find a reference datum point led to the choice of station “77KZ122” with (latitude, longitude) = (45° 56' 38.4", 71° 46' 58.8") MSL. The orthometric height for this datum was 259.702 m in the CGVD28 reference system. The reason for choosing CGVD28 over the CGVD2013 reference system is simple. The 2005 measurements of depths around the deflectors were made before CGVD2013 was defined. Thus, to eliminate errors coming from the difference between the two-reference systems, CGVD28 is a better choice. In Table 10, values obtained from Equation 49 for geoid height are listed. The values are added to the river depth.

Table 10: Ellipsoid, orthometric, geoid height of images

	WorldView-2 image	WorldView-3 image
Ellipsoid Height	160.2	161.45
Orthometric Height	259.702	259.702
Geoid Height	98.252	99.502

3.7 Normalized difference water index (NDWI)

Creating depth contours of a river channel requires the separation of wet pixels of the river from other pixels. Some methods can discriminate water bodies from soil and vegetated pixels. One of these methods is based on the reflectance of different wavelengths. Researches show that water bodies strongly absorb Near Infra-Red (NIR), but NIR is highly reflected by vegetation and soil (McFeeters 1996). Employing a single NIR band, water bodies appear in the dark; soil and terrestrial vegetation look lighter. The disadvantage of this method is although it suppresses non-wet pixels, it does not remove them. On the other hand, the green band acts oppositely to the NIR band and has the maximum reflectance from water features. Normalize Difference Water Index takes advantage of the maximum reflectance for the green band and the minimum reflectance for the NIR band in wet pixels (McFeeters 1996). A threshold between these two bands discriminates the river's pixels from the rest. The NDWI is calculated as

$$[50] \quad \mathrm{NDWI} = \frac{\mathrm{Green} - \mathrm{NIR1}}{\mathrm{Green} + \mathrm{NIR1}}$$

This index varies from -1 to +1, and the water feature has positive values. In Figure 15, part of the Nicolet River after NDWI was applied is illustrated. River pixels distinguish in brighter color, compared to the rest of the pixels, and their values are positive.

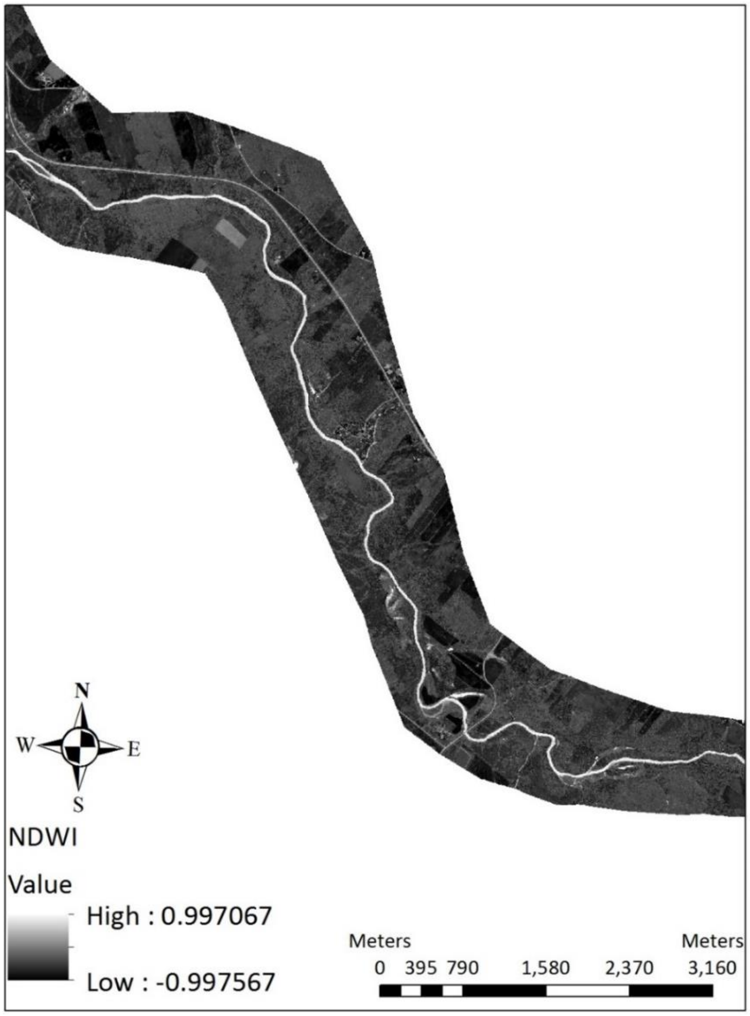

Figure 15: Normilized difference water index (NDWI) map of the Nicolet River.

3.8 Extracting river from the rest of image

After distinguishing wet pixels from dry pixels (river boundaries) through NDWI in the previous section, it is possible to separate and extract river pixels from the rest of the pixels. The reason behind this important process in the analytical approach is the necessity of choosing accurate radiance input data for use in the analytical model proposed in this study. Unlike in Niroumand-Jadidi et al. (2020), no field measurements of depth are needed as input to the proposed model. On the other hand, the success of the proposed model lies in the use of precise remote sensing data as input; of the most importance is the wavelength radiance of images. An analysis of the results from this study indicates that an increase in the accuracy of radiance variable is achieved when only wavelength radiances from river pixels are used in the calculations. The resulting bathymetry becomes more precise when using radiance from river pixels.

4 RESULTS

This chapter presents the results of river bathymetry for the site of study. The bathymetry was retrieved from high-resolution multi-spectral images of the World-View2 and World-View3 satellites, using analytical methods that involved the ratios of bands and the attenuation coefficients. The results for two conditions: before and after radiometric corrections, are compared. The comparison helps improve our understanding of the influence of corrections on reflectance.

4.1 Separation of bands

Four wavelength bands were extracted from the multispectral images. The result was a separation of multispectral images into multi-single band images. The range of radiance values are listed in Tables 11 and 12. After separation, for each of the bands, the radiance values range from zero to a specific level. The band values are shown in Figures 16 and 17. These values are raw data extracted from WorldView-2 and WorldView-3 satellite images for the site of this study. They are the basic input to the calculations of the attenuation coefficient and the ratio between two bands. It is important to note that the values need to be corrected before they are used in the band ratio algorithm.

Table 11: WorldView-2 band ranges of the visible spectrum of images for the site of study.

Band Index	Band	Minimum Radiance Value	Maximum Radiance Value
B1	Coastal Blue	0	1254
B3	Green	0	1960
B4	Yellow	0	2047
B5	Red	0	1819

Table 12: WorldView-3 band ranges of the visible spectrum of images for the site of study.

Band Index	Band	Minimum Radiance Value	Maximum Radiance Value
B1	Coastal Blue	0	826
B3	Green	0	1525
B4	Yellow	0	1722
B5	Red	0	1928

To reveal the influence of corrections, we calculated and compared the reflectance of wavelengths between before- and after-radiometric corrections. We assessed the quality by comparing the calculation output with available Nicolet River elevations in the deflector pool. The goal of this primary step was to validate and check the accuracy of our analytical methods. This step is important to mapping the bathymetry for the rest of the river channel. Proper ban separation and the proper use of band ratios are essential to the success of our analytical methods.

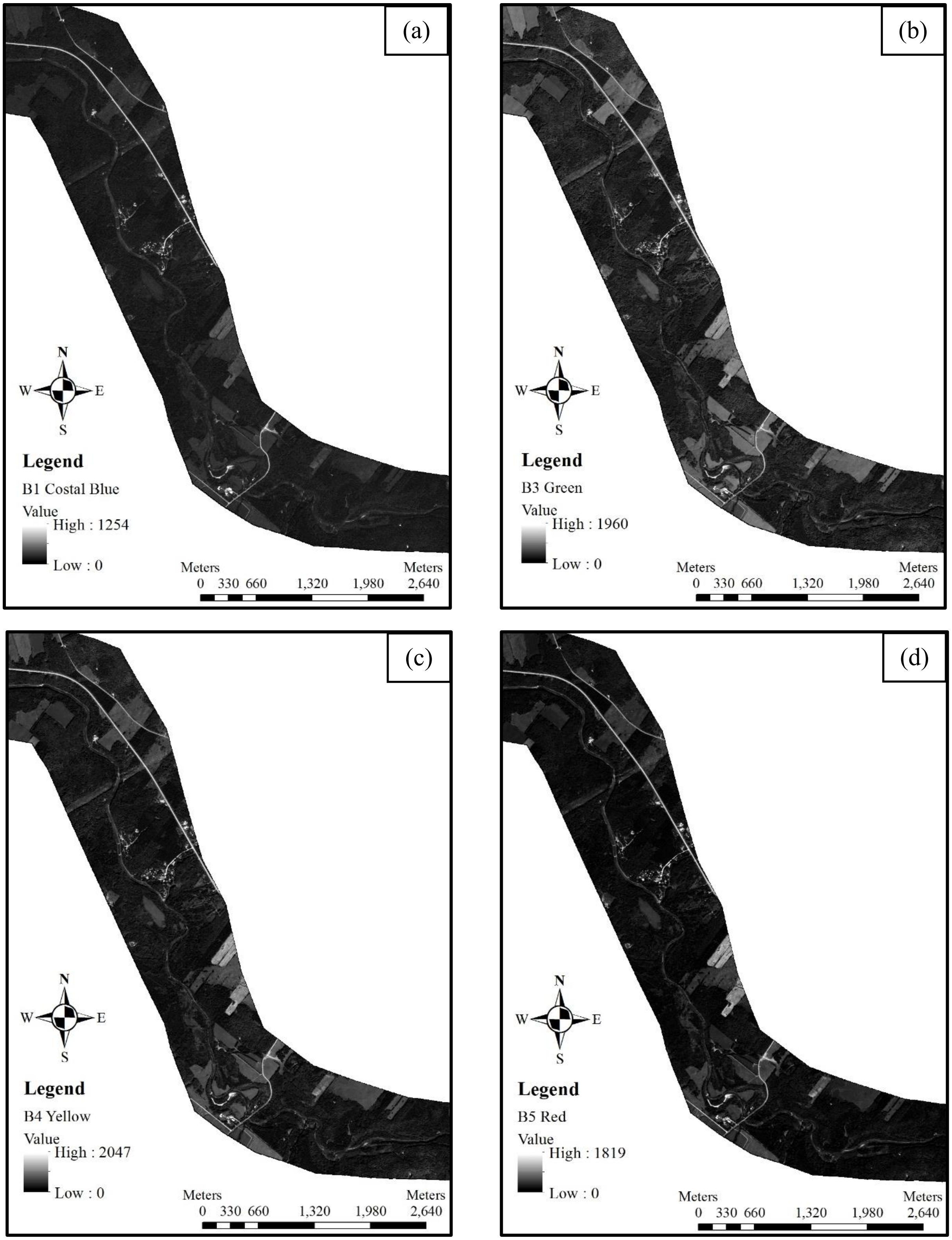

Figure 16: WorldView-2 image pixel value (radiance) for: a) coastal blue; b) green band; c) yellow band; d) red band

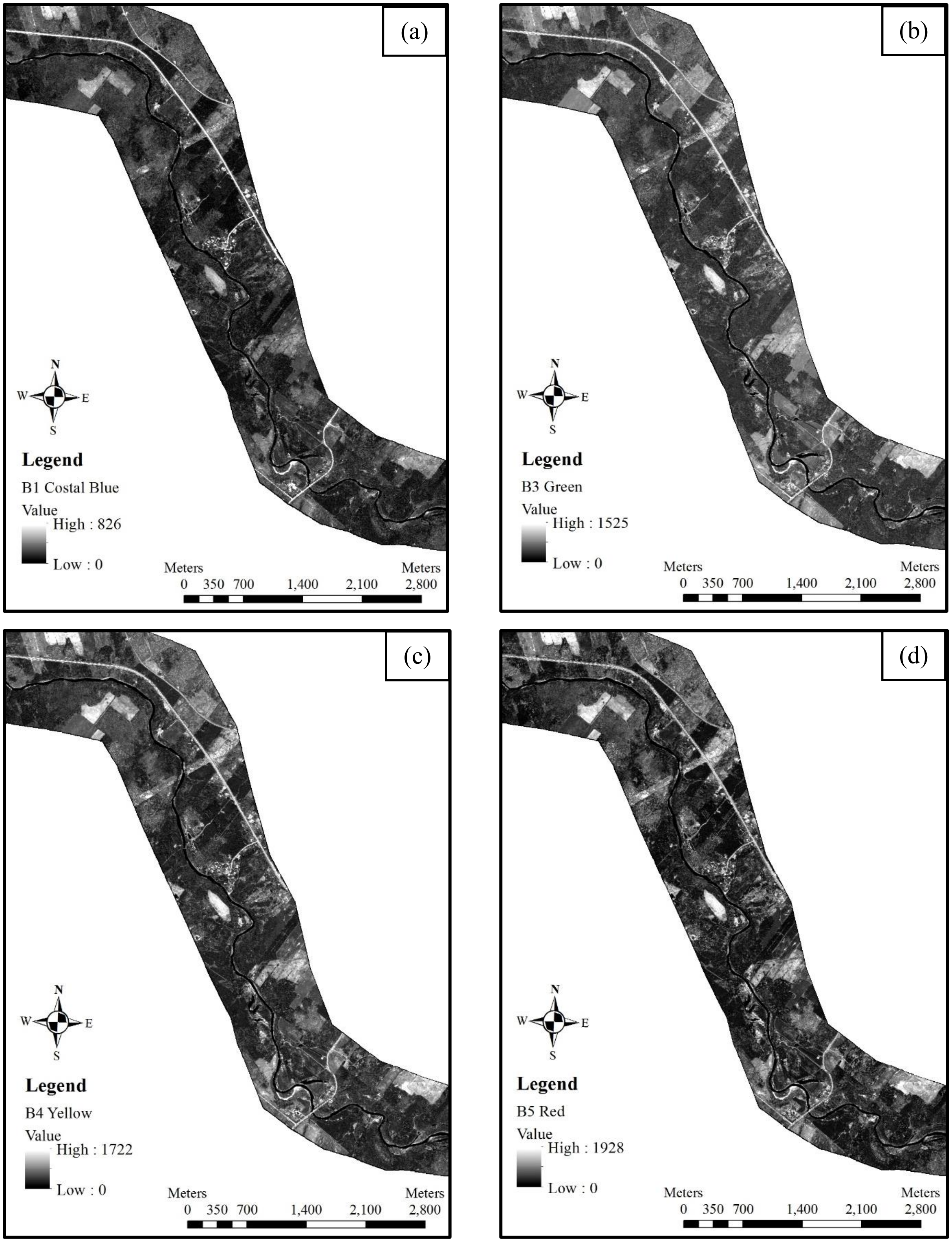

Figure 17: Worldview-3 image pixel value (radiance) for: a) coastal blue; b) green band; c) yellow band; d) red band

4.2 Riverbed elevations without radiometric corrections

This section discusses the results of riverbed elevation retrieved from images without radiometric corrections. Radiometric values from band separation were used directly to calculate wavelength reflectance (Eq. 41); no radiometric corrections were applied. The idea was to demonstrate the influence of the corrections on the results. The WorldView-3 image had a better resolution than the WorldView-2 image, and thus was selected for the demonstration. In the visible spectrum of WorldView-3 image, there are 12 combinations of the natural logarithm of bands: 1) red to green; 2) blue to green; 3) yellow to green; 4) red to yellow; 5) red to blue; 6) blue to red; 7 to 12) the inverse of the six ratios listed above. Which of these band ratios is the most suitable for use ultimately to map bathymetry?

We answered this question by checking that the combination of wavelengths produces results of riverbed elevations in closest agreement with the available field measurements from the deflector pool. For the WorldView-3 image of the Nicolet River, the best pair of wavelengths are the combination of green and red bands. The attenuation coefficients calculated for the two bands before radiometric corrections, along with all necessary parameters required in the calculations, are summarised in Tables 13 and 14. In Equation 23, from the attenuation coefficients, K_1 and K_2, for the green and red bands, the effective attenuation coefficient ($K_1 - K_2$) for the WorldView-3 image before radiometric corrections was 0.1533.

Table 13: Attenuation coefficient and relevant parameters for the green band of WorldView-3 image before radiometric correction

Parameter	Value	Units
Absorption Coefficient (a)	0.0775	m^{-1}
backscattering coefficient of pure seawater (b_{bw})	0.0014	m^{-1}
backscattering coefficient of suspended particles (b_{bp})	0.0015	m^{-1}
Total backscattering (b_b)	0.0029	m^{-1}
Spectral power for particle backscattering coefficient (Y)	0.2172	-
u ratio	0.0343	-
Attenuation Coefficient	0.0978	m^{-1}

Table 14: Attenuation coefficient and relevant parameters for the red band of WorldView-3 image before radiometric correction.

Parameter	Value	Units
Absorption Coefficient (a)	0.1908	m^{-1}
backscattering coefficient of pure seawater (b_{bw})	0.007	m^{-1}
backscattering coefficient of suspended particles (b_{bp})	0.0017	m^{-1}
Total backscattering (b_b)	0.0087	m^{-1}
Spectral power for particle backscattering coefficient (Y)	0.2172	-
u ratio	0.0421	-
Attenuation Coefficient	0.2511	m^{-1}

Now, applying the effective attenuation coefficient to natural logarithm ratio of red to green band for WorldView-3 image resulted in water depth at each pixel. In this study, Equation 49 converts the water depth to elevation at each pixel. Results of riverbed elevation are plotted in Figure 18 for the 25-km long river channel; details for sub-areas and key locations are shown in Figures 19 and 20.

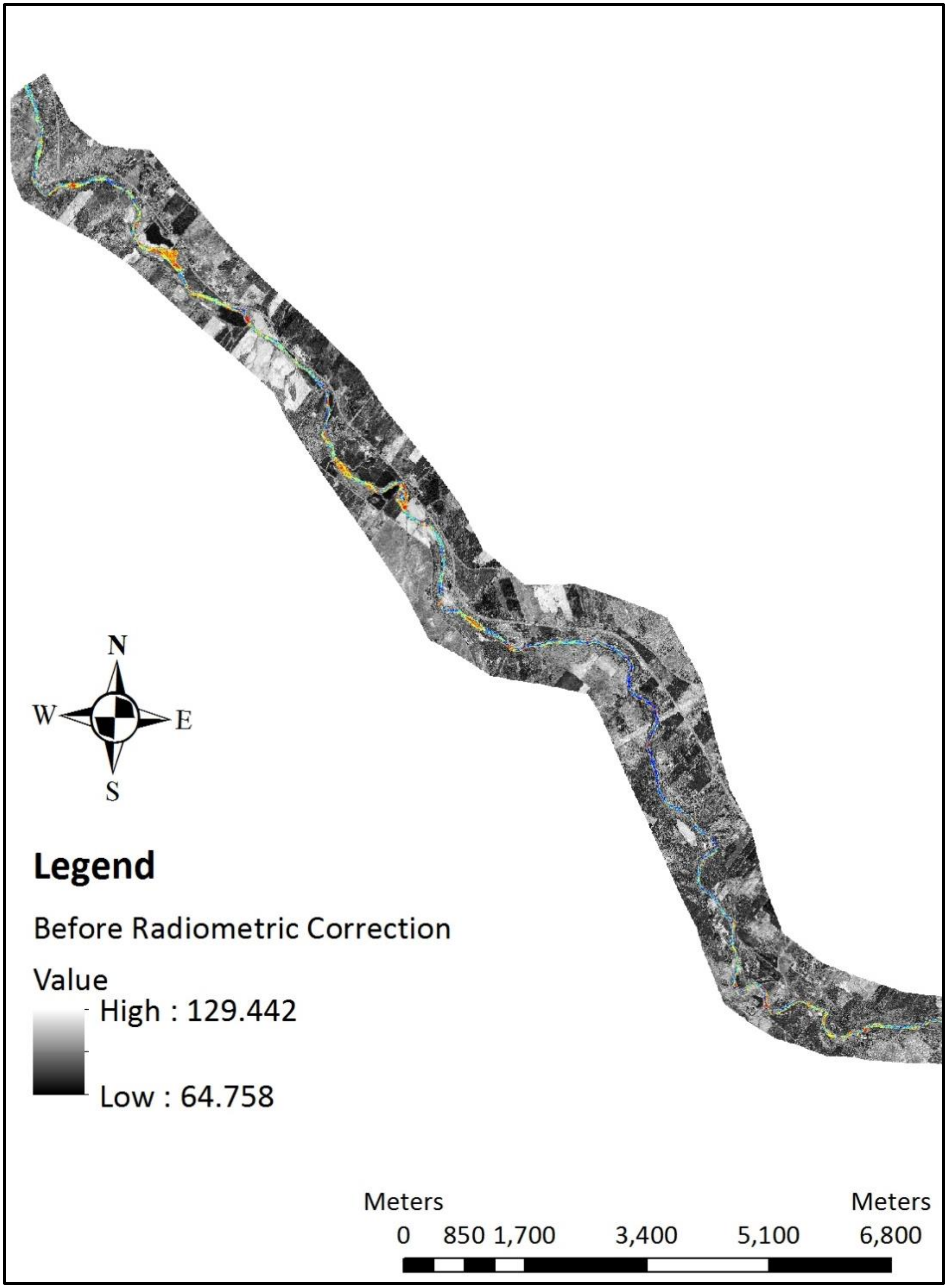

Figure 18: Overview of the result of riverbed elevation for the Nicolet River

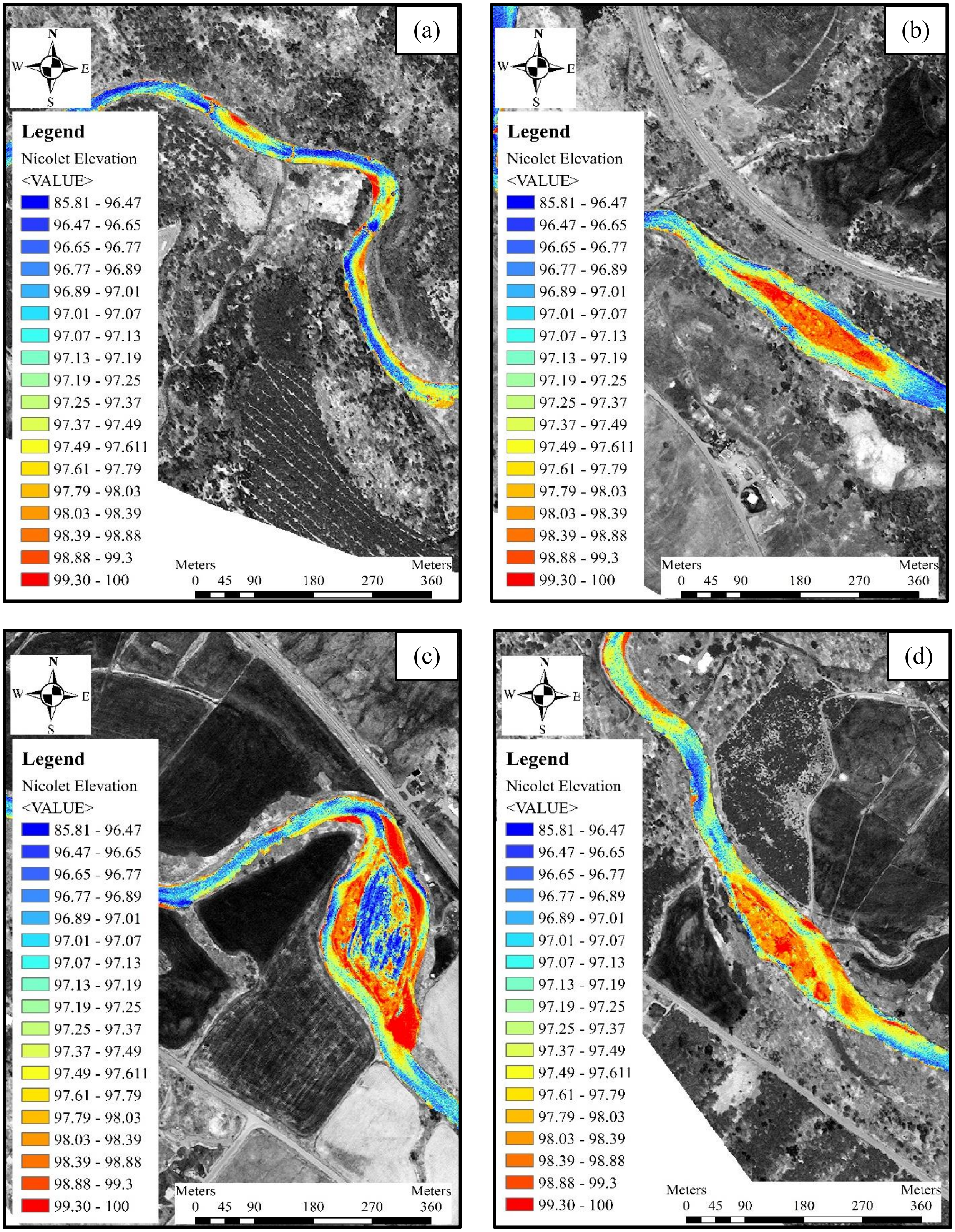

Figure 19: Elevation detail for some locations of the Nicolet River in WorldView-3 image before radiometric corrections.

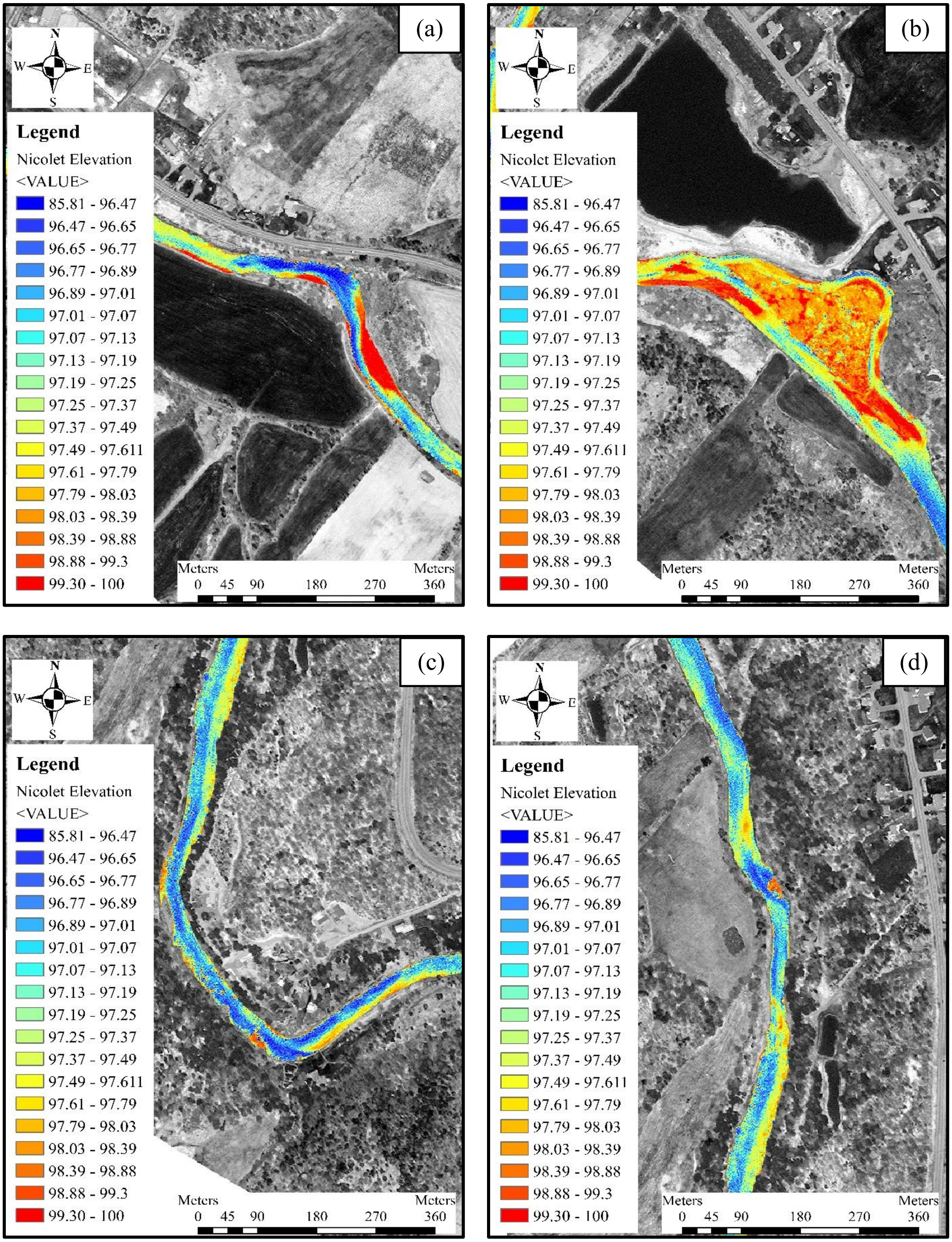

Figure 20: Elevation detail for some locations of the Nicolet River in WorldView-3 image before radiometric corrections.

Consider the pool around the deflectors in the Nicolet River. The riverbed elevations are shown in Figure 21. The field measurements (Carré et al. 2007) illustrated in Figures 5 and 6 show changing riverbed elevations between 96.5 and 97 m in the pool area and 97.1 to 97.9 m surrounding the pool. The caluculated riverbed elevations using our analytical approach are compared with the measured elevations in Figure 22.

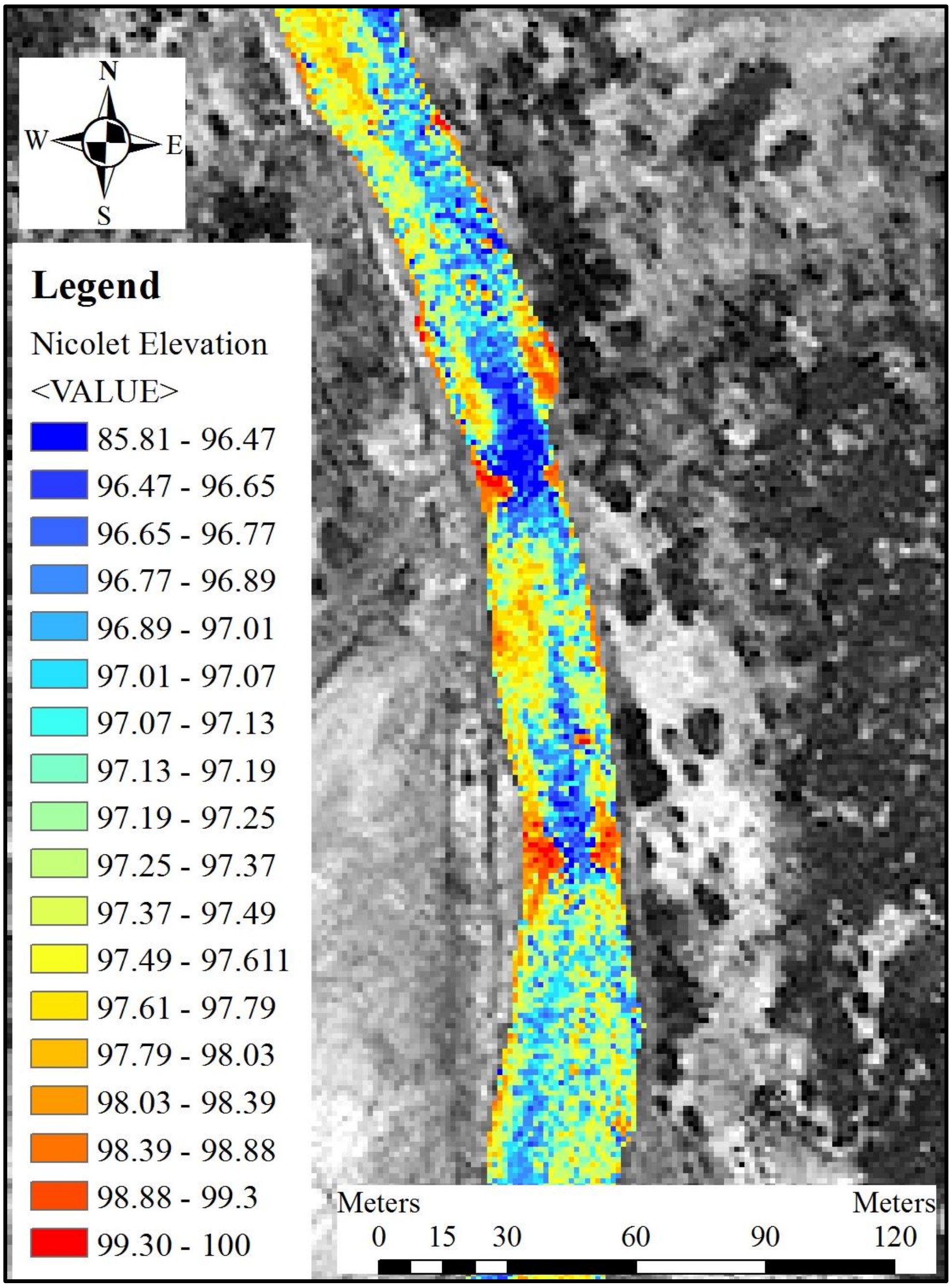

Figure 21: The Nicolet River elevations around deflectors before radiometric correction

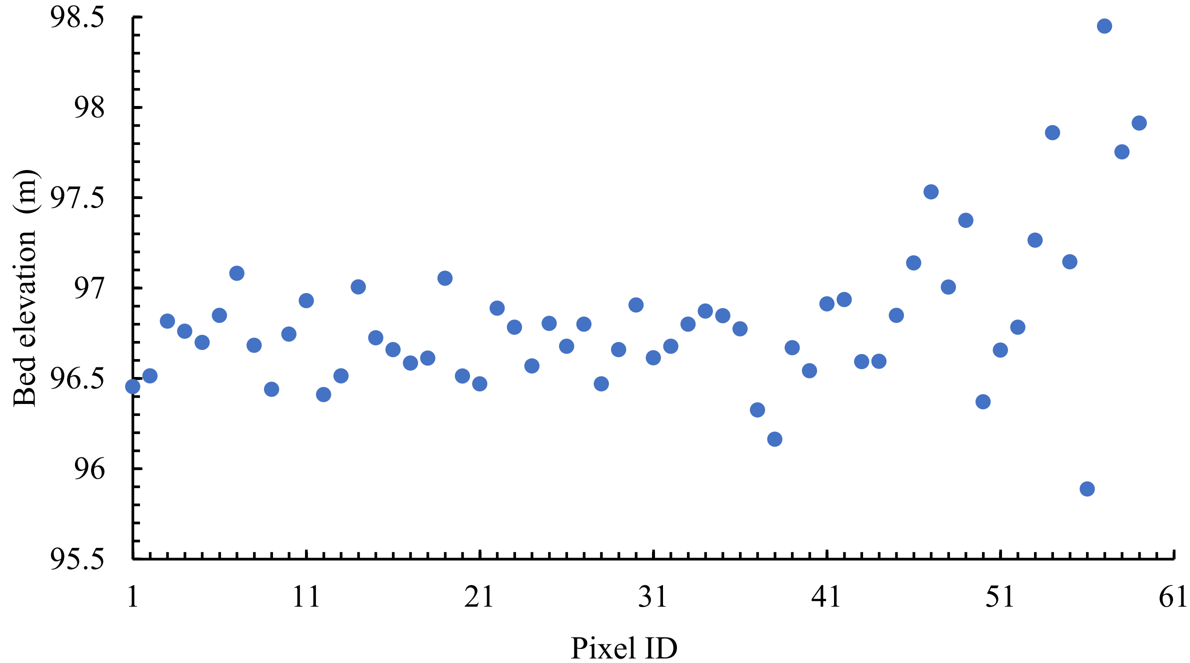

Figure 22: Bed elevation from WorldView-3 at 59 pixels located downstream of the pool (Figure 21) before radiometric corrections.

The pool area of comparison consisted of 59 pixels, each having a size of 1.2 m × 1.2 m. Out of the 59 pixels, 13 show bed elevation values of larger than 97 m, and 9 show values of lower than 96.5 m. This means that before radiometric corrections, a total of 22 pixels out of 59 has calculated elevations different from the reported measurements. In other words, about 62.7% of the analytical data points are valid. This is without applying atmospheric corrections. The following section focuses on applying radiometric corrections and their influence in the accuracy of results.

4.3 Corrections of radiometric bands in band ratio algorithm

For each image the corrections use Equation 39 for the WorldView-2 image and Equation 40 for the WorldView-3 image. The corrections removed the atmosphere effects on wavelengths and provided more reliable data for further calculations. After the corrections, the corrected values of radiance were converted to top-of-atmosphere reflectance. Then the reflectance entered the calculations of logarithm band ratio, as part of input in Equation 23. A comparison between Figures 16 to 23 and Figures 17 to 24 shows changes between before- and after-radiometric corrections. For each of the satellite images, the most noticeable change in the band ranges is a significant decrease in pixel values. In Figure 23, no pixel values were larger than 5.3, and there were no negative pixel values, whereas in Figure 24, radiometric corrections brought changes. The corrections were that some of the pixel values became negative. This may be due to negative values for image offset.

As in the analysis of images without radiometric corrections, we explored various band combinations for both satellite images after radiometric corrections. The results demonstrate that the best combination of bands for mapping the Nicolet River elevations was the ratio between the red and the green band for the WorldView-3 satellite image, and the ratio of the green to the yellow band for the WorldView-2 satellite image. In Tables 15 and 16, a summary of the elevation results, along with and necessary parameters and coefficients, for the green and red bands of the WorldView-3 satellite image in the calculations of the attenuation coefficient, is given.

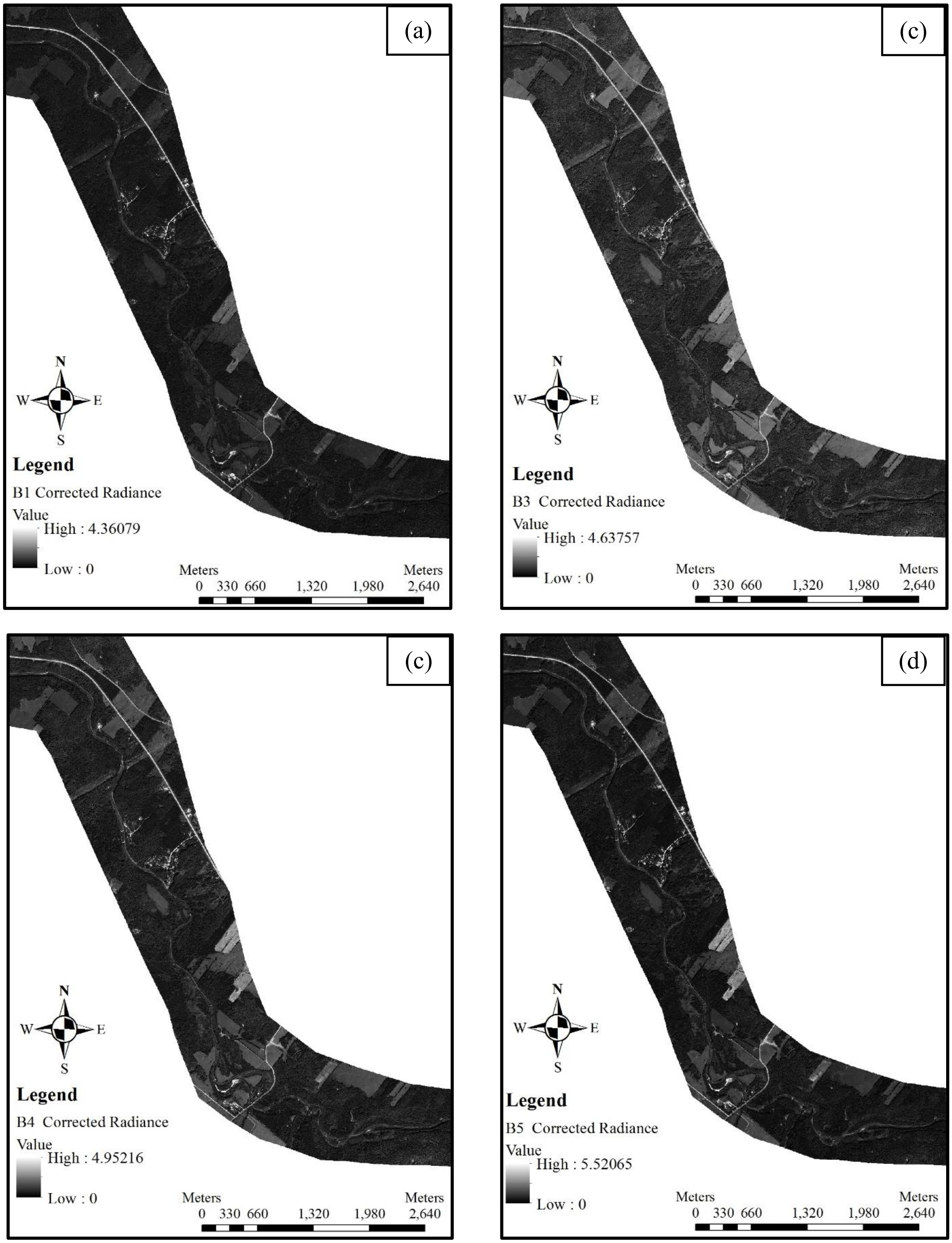

Figure 23: Radiometrically corrected images from WorldView-2 satellite: a) band B1; b) band B3; c) band B4; d) band B5

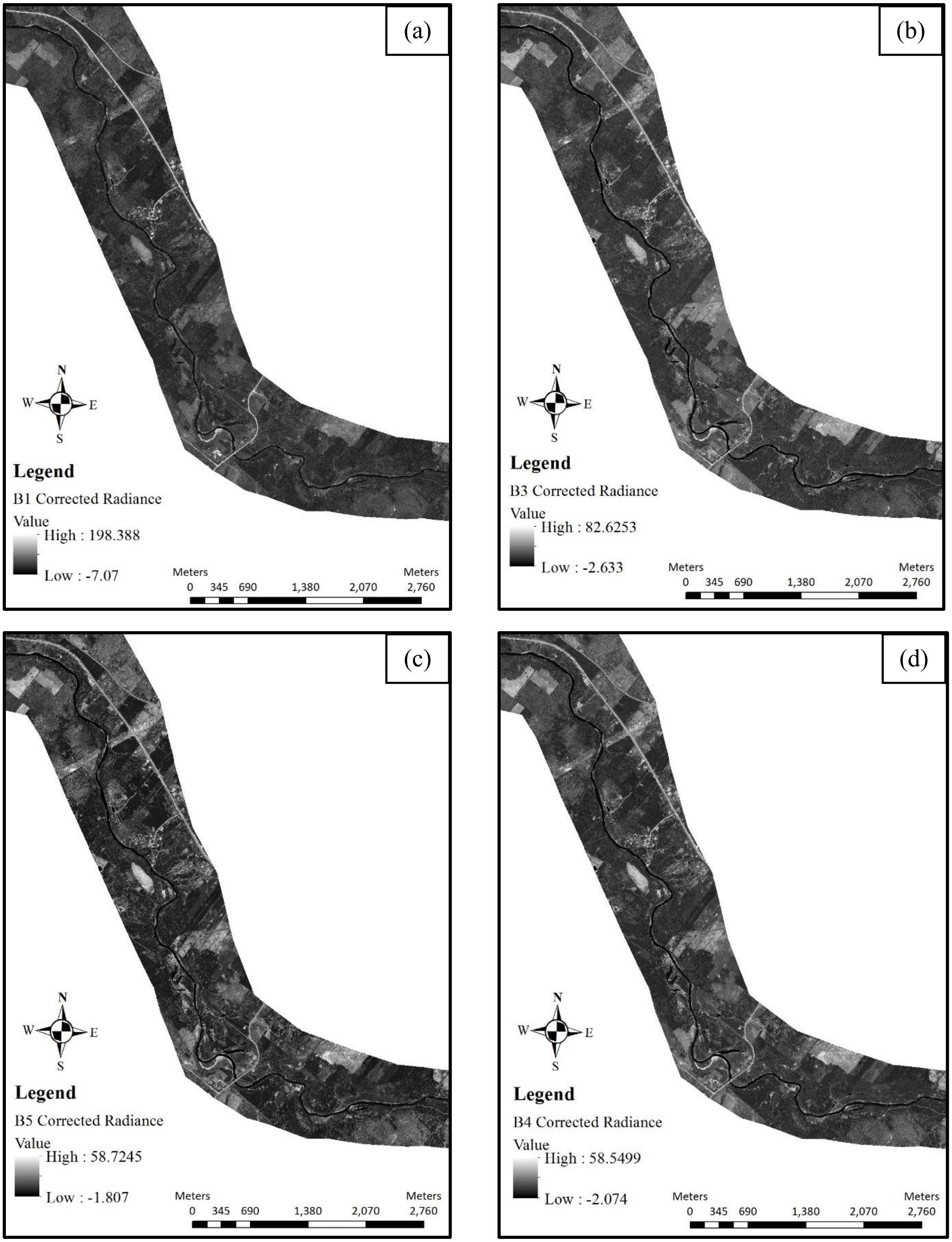

Figure 24: Radiometrically corrected images from WorldView-3 satellite: a) band B1; b) band B3; c) band B4; d) band B5

Table 15: Attenuation coefficient and relevant parameters for the green band of WorldView-3 image after radiometric correction.

Parameter	Value	Units
Absorption Coefficient (a)	0.0677	m^{-1}
backscattering coefficient of pure seawater (b_{bw})	0.0014	m^{-1}
backscattering coefficient of suspended particles (b_{bp})	8.0533	m^{-1}
Total backscattering (b_b)	8.0547	m^{-1}
Spectral power for particle backscattering coefficient (Y)	1.8363	-
u ratio	0.9917	-
Attenuation Coefficient	25.3232	m^{-1}

Table 16: Attenuation coefficient and relevant parameters for the red band of WorldView-3 image after radiometric correction.

Parameter	Value	Units
Absorption Coefficient (a)	1.1398	m^{-1}
backscattering coefficient of pure seawater (b_{bw})	0.0007	m^{-1}
backscattering coefficient of suspended particles (b_{bp})	5.8585	m^{-1}
Total backscattering (b_b)	5.8592	m^{-1}
Spectral power for particle backscattering coefficient (Y)	1.8363	-
u ratio	0.8372	-
Attenuation Coefficient	25.7892	m^{-1}

A comparison of attenuation coefficient values for the green and red band between before- and after-radiometric corrections indicates that the corrections yielded significantly higher values. However, the difference between the two attenuation coefficients or the effective attenuation coefficient remains below unity (equal to 0.4660). The data shown in Figures 25 and 26 demonstrates how the resolution and elevations changed from before- to after-radiometric corrections.

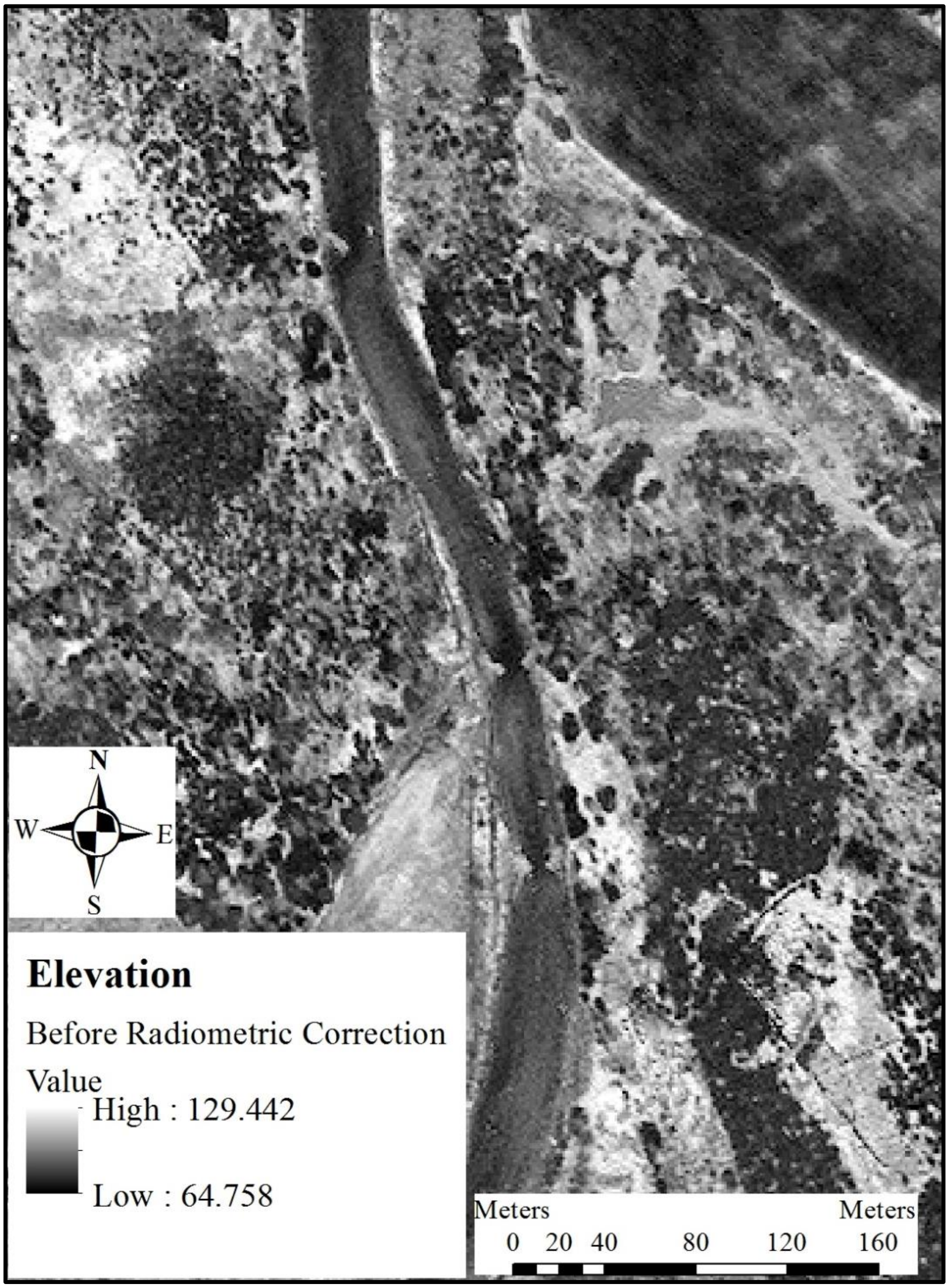

Figure 25: Bed elevations from WolrdView-3 Image for the locations of the deflectors before radiometric corrections.

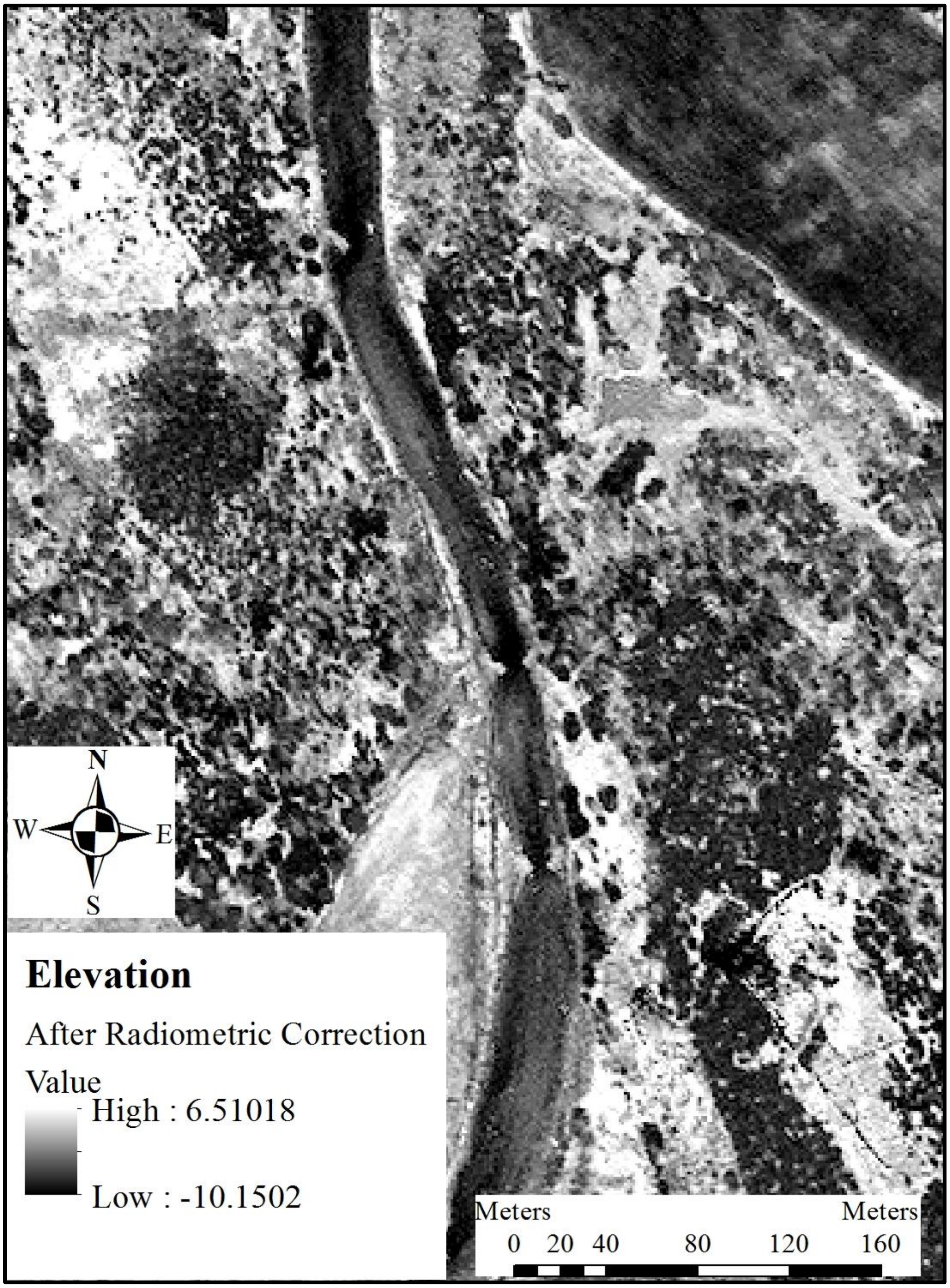

Figure 26: Bed elevations from WolrdView-3 Image for the locations of the deflectors after radiometric corrections.

In Figure 27, river elevation extracted from the rest of image to investigate the changes in elevation after radiometric corrections.

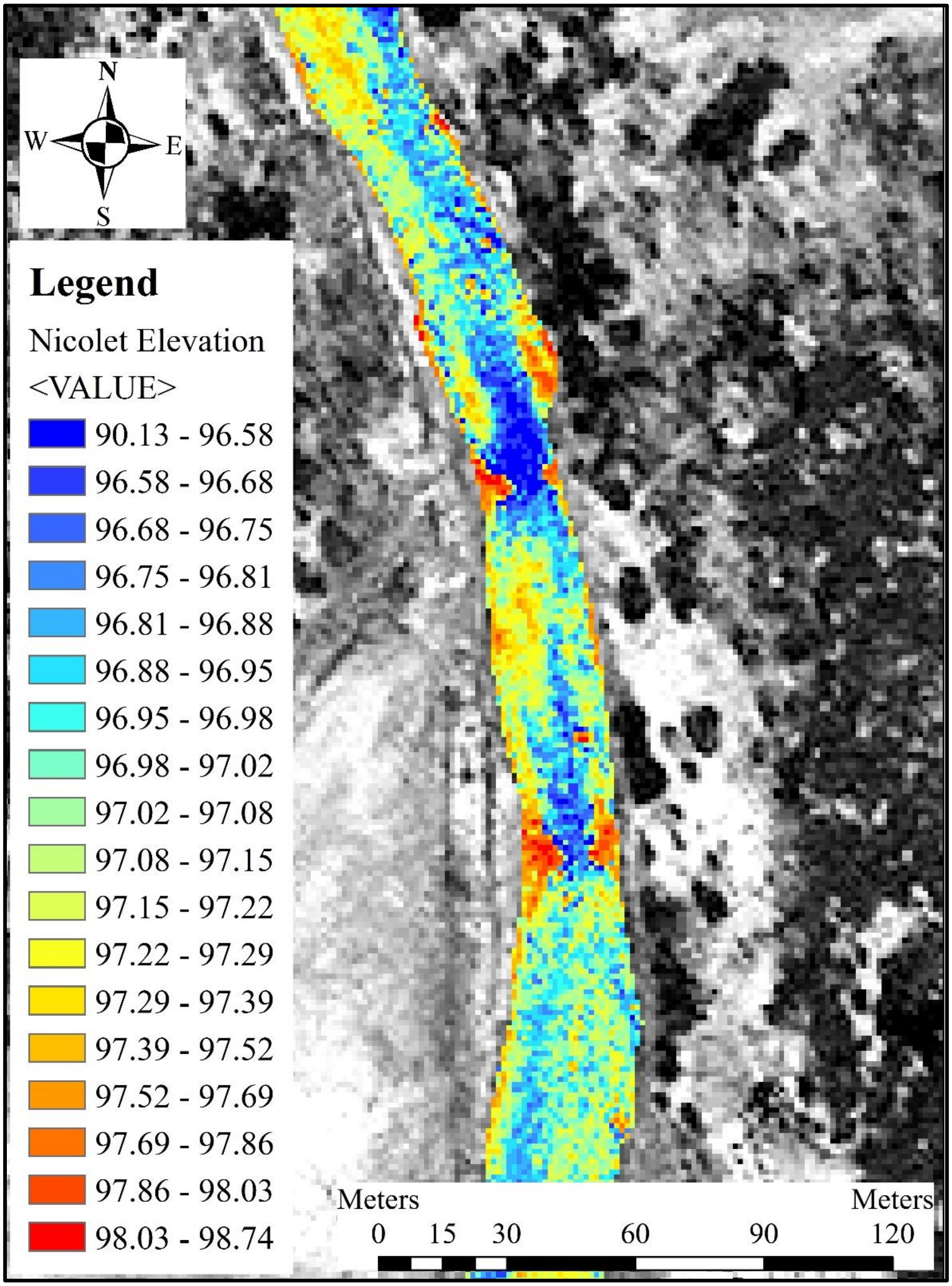

Figure 27: Bed elevations along the Nicolet River after radiometric correction. The regions of the deflectors are shown by the contrast between the red colour and dark blue colour.

Based on the field measurements (Carré et al. 2007), the riverbed elevations should be between 96.5 and 97 m. In Figure 28, only two pixels had elevation values smaller than 96.5 m, and seven pixels had values larger than 97 m. Only 9 pixels show values outside the range of measured values. This is a remarkable improvement over the calculations before radiometric corrections, in which 22 out of 59 pixels had values outside the range. In conclusion, the radiometric corrections in the analytical method increased the accuracy of results from 62.7% to 84.7% in terms of data points falling into the expected range of riverbed elevations.

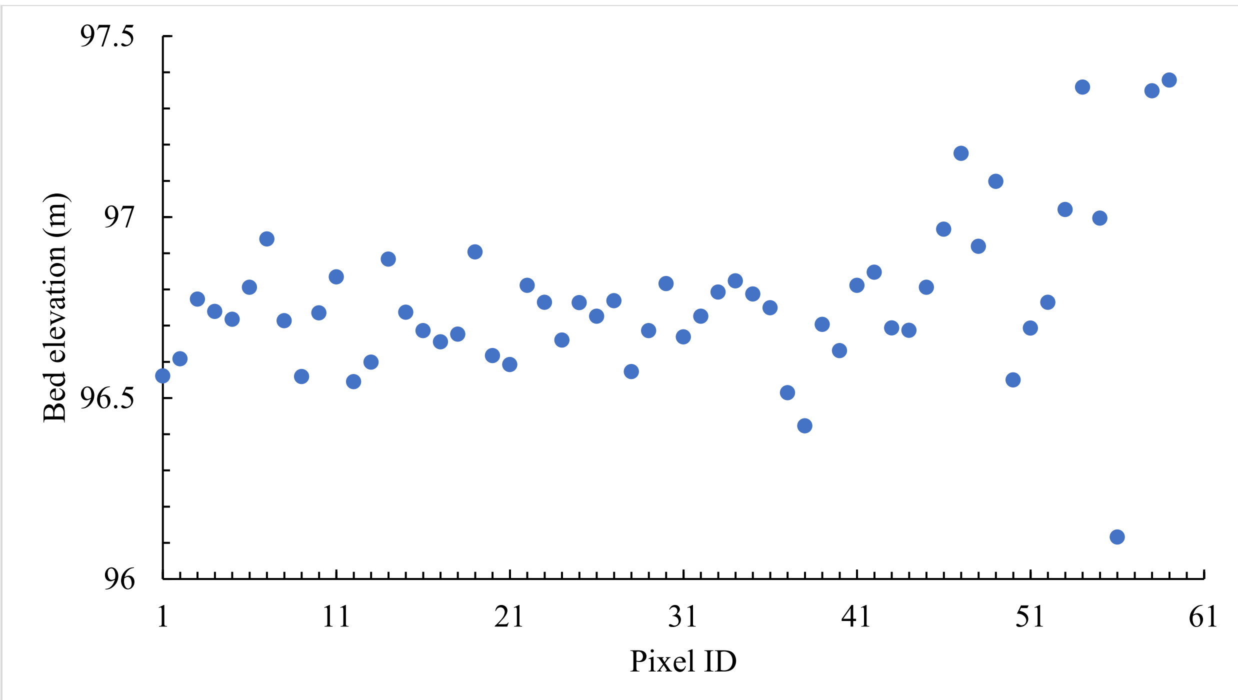

Figure 28: Bed elevation from WorldView-3 at 59 pixels located downstream of the pool (Figure 27) after radiometric corrections.

In Figures 29 and 30, it is shown that the Nicolet River bathymetry exhibits such realistic geometric features as braided sections, meanders, and oxbow sections. These features became noticeable when comparing the after-radiometric correction figures to Figures 19 and 20 where no radiometric corrections were applied. A lesson learned from analysing the WorldView-3 satellite image is that radiometrical corrections lead to reliable and accurate riverbed elevations and hence flow depth of the river.

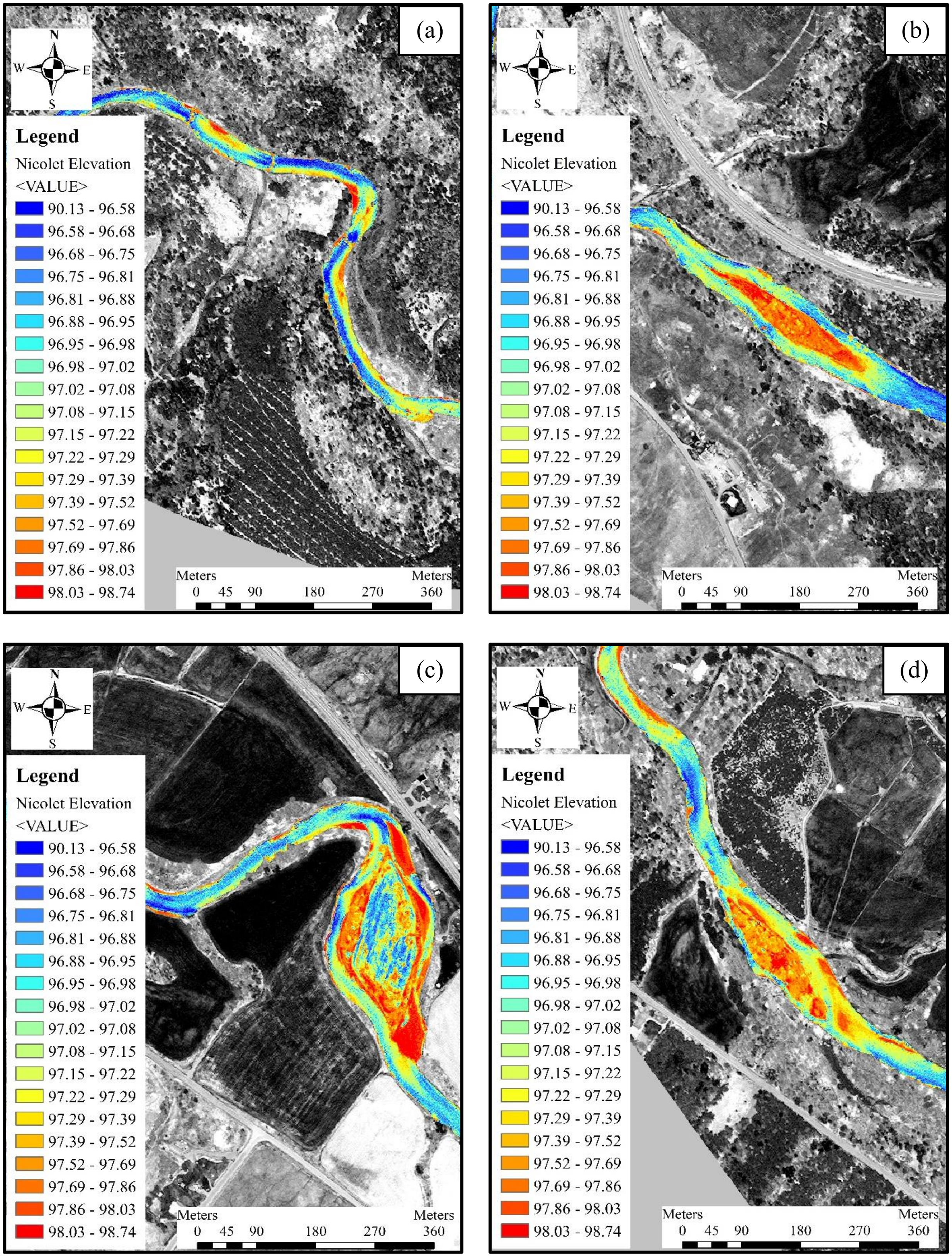

Figure 29: Elevation detail for some locations of the Nicolet River in WorldView-3 image after radiometric corrections.

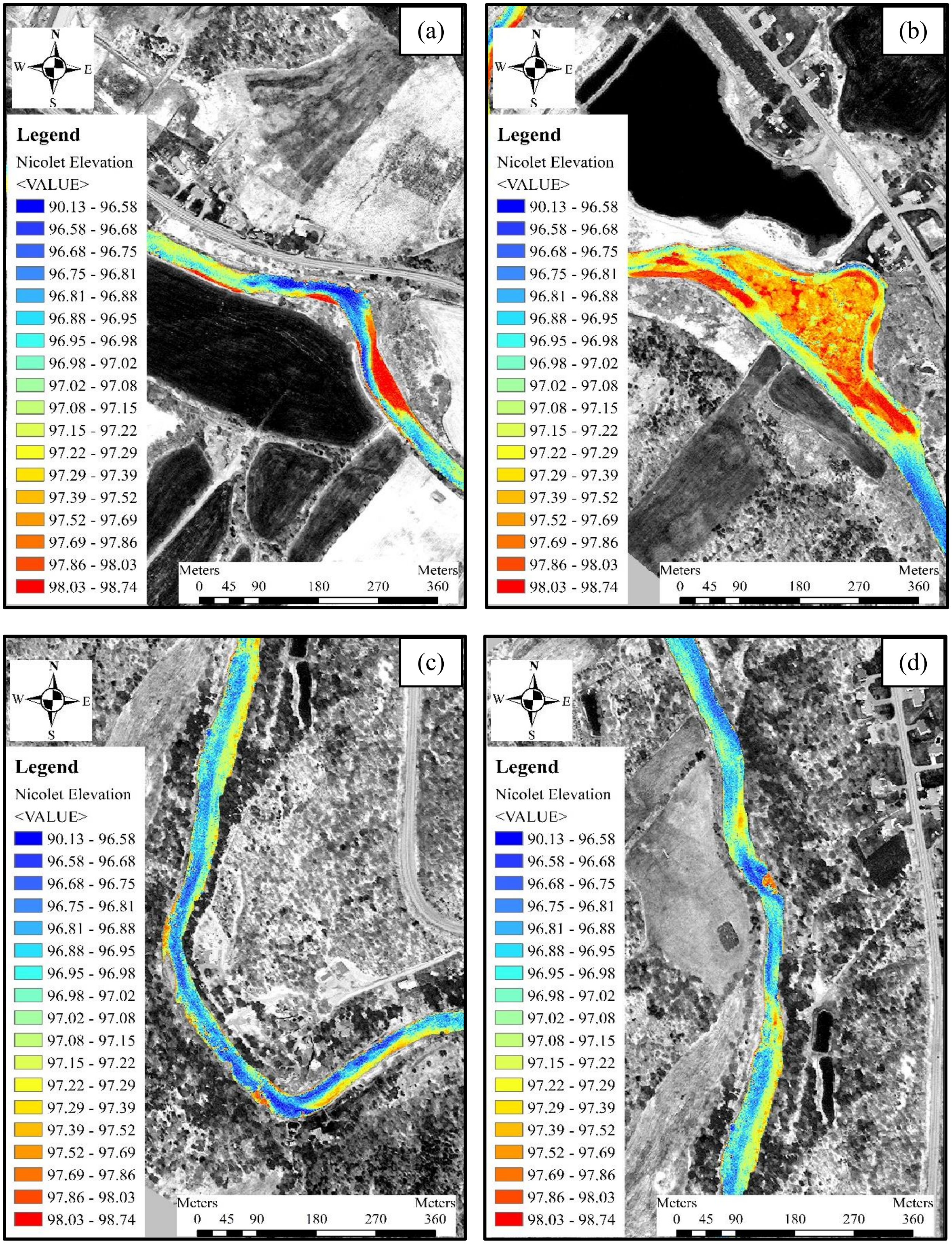

Figure 30: Elevation detail for some location of the Nicolet River in WorldView-3 image after radiometric corrections.

For the WorldView-2 satellite image, we focused on the issue of radiometric corrections. We compared the suitability of all band combinations, and identified the ratio between the green and the yellow band as the most suitable choice as it produced riverbed elevations closest to the available field measurements from the deflector pool. The procedures for calculations are similar as for the WorldView-3 image. Radiometric corrections were applied according to Equation 39; values of reflectance of each band were calculated; the attenuation coefficient was evaluated. The results are summarised in Tables 17 and 18, with details of all coefficients and constants involved for the calculation of the attenuation coefficient for each band. The difference of attenuation coefficient between the green and the yellow band gives the effective attenuation coefficient for the WorldView-2 image covering the Nicolet river. The effective attenuation coefficient was 0.0996.

Table 17: Attenuation coefficient and relevant parameters for the green band of WorldView-2 image.

Parameter	Value	Units
Absorption Coefficient (a)	0.1460	m^{-1}
backscattering coefficient of pure seawater (b_{bw})	0.0014	m^{-1}
backscattering coefficient of suspended particles (b_{bp})	0.0849	m^{-1}
Total backscattering (b_b)	0.0863	m^{-1}
Spectral power for particle backscattering coefficient (Y)	1.1267	-
u ratio	0.3714	-
Attenuation Coefficient	0.4998	m^{-1}

Table 18: Attenuation coefficient and relevant parameters for the yellow band of WorldView-2 image

Parameter	Value	Units
Absorption Coefficient (a)	0.1061	m^{-1}
backscattering coefficient of pure seawater (b_{bw})	0.0009	m^{-1}
backscattering coefficient of suspended particles (b_{bp})	0.0767	m^{-1}
Total backscattering (b_b)	0.0776	m^{-1}
Spectral power for particle backscattering coefficient (Y)	1.1267	-
u ratio	0.4225	-
Attenuation Coefficient	0.4002	m^{-1}

Using this value for effective attenuation, the WorldView-2 image yielded Nicolet riverbed elevations. The results of elevations with radiometric corrections are shown in Figure 31 for the area of deflectors. A comparison between Figures 31 and 27 clearly shows the difference in quality between images of different resolutions. The WorldView-2 image had a resolution of 2 m (Figure 31), whereas the WorldView-3 image had a resolution of 1.2 m (Figure 27). Another noticeable difference was colour spans showing different levels of elevations in the Nicolet River. On the new colour span, the pixel values for elevations in the downstream pool are extracted and plotted in Figure 32.

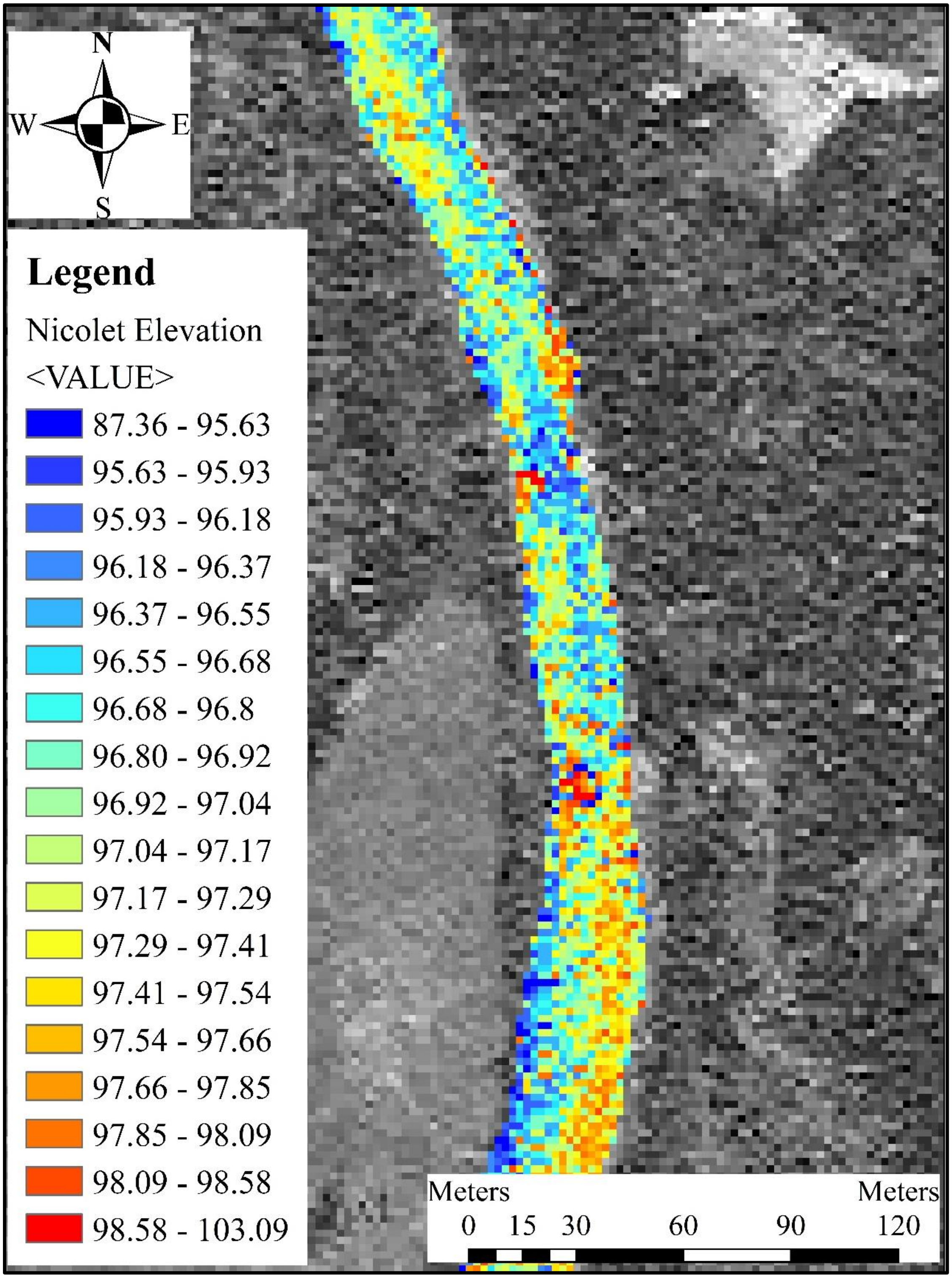

Figure 31: Bed elevations along the Nicolet River after radiometric correction for WorldView-2 image. The regions of the deflectors are shown by the contrast between the red colour and dark blue colour.

In Figure 32, 16 pixels had values of larger than 97 m, and eight pixels had values of smaller than 96.5 m. These values are outside the range of riverbed elevations measured from locations in the downstream pool. This is to say that even after applying radiometric corrections as stated in the WolrdView-2 satellite guide, a significant number of pixels values were not comparable to the measured elevations. Equation 40 for radiometric corrections of WorldView-3 satellite images considers the effects of atmosphere in terms of deviation and delay of received radiance to the satellite sensor through the gain and offset constants of bands. The same consideration is not given in Equation 39 got radiometric corrections of WorldView-2 images. This is probably the reason for the poor quality of bathymetry results from the WorldView-2 image.

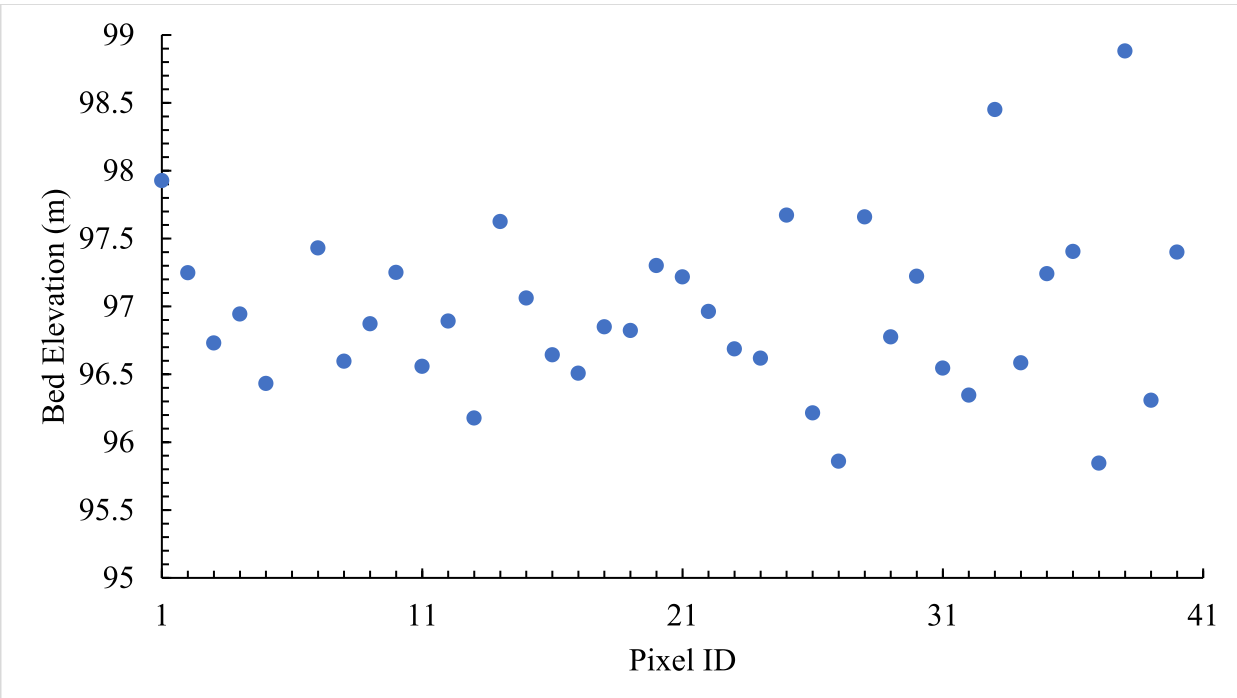

Figure 32: Bed elevation from WorldView-2 at 40 pixels located downstream of the pool (Figure 31) after radiometric corrections.

4.4 Cross section depths of the Nicolet River

The river bathymetry of the 25-km long reach of the Nicolet River was mapped from the WorldView-3 image. An example of the mapped river bathymetry was plotted as water depth in Figure 33. A cross-sectional view of the bathymetry is useful. We selected five channel cross-sections, marked as A, B, C, D and E in Figure 33, and provided a cross-sectional view of varying riverbed elevations from one riverbank to the other (Figures 34 to 38). It is understood that at each of the five cross-sections, the water depths changed across the cross-section width. The bathymetry data for each of the cross-sections in ArcGIS plotted in Figures 34 to 38 are provided in Appendix A of this thesis.

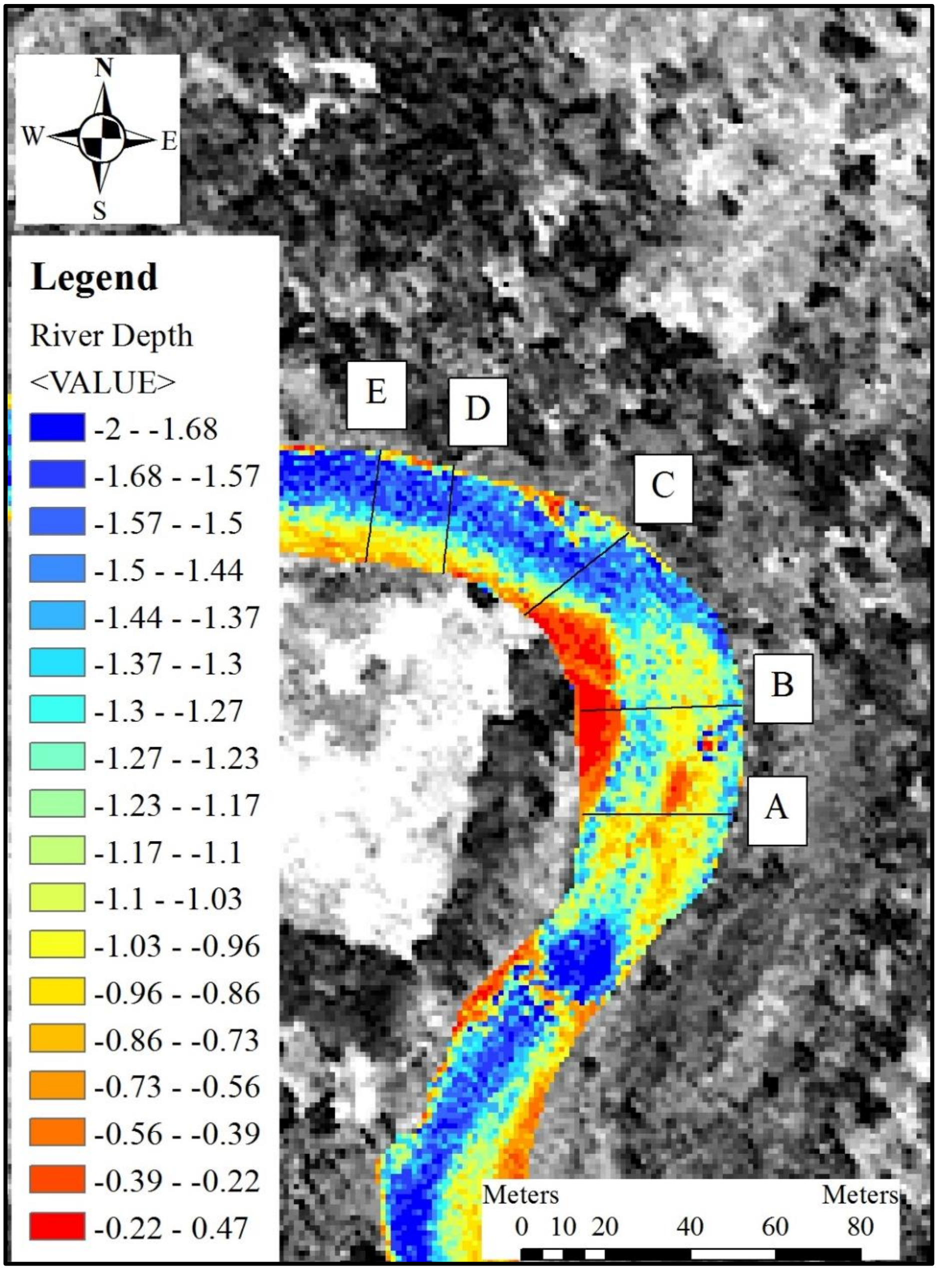

Figure 33: The Nicolet River water depth corresponding to Figure 29a and locations of five selected cross-sections.

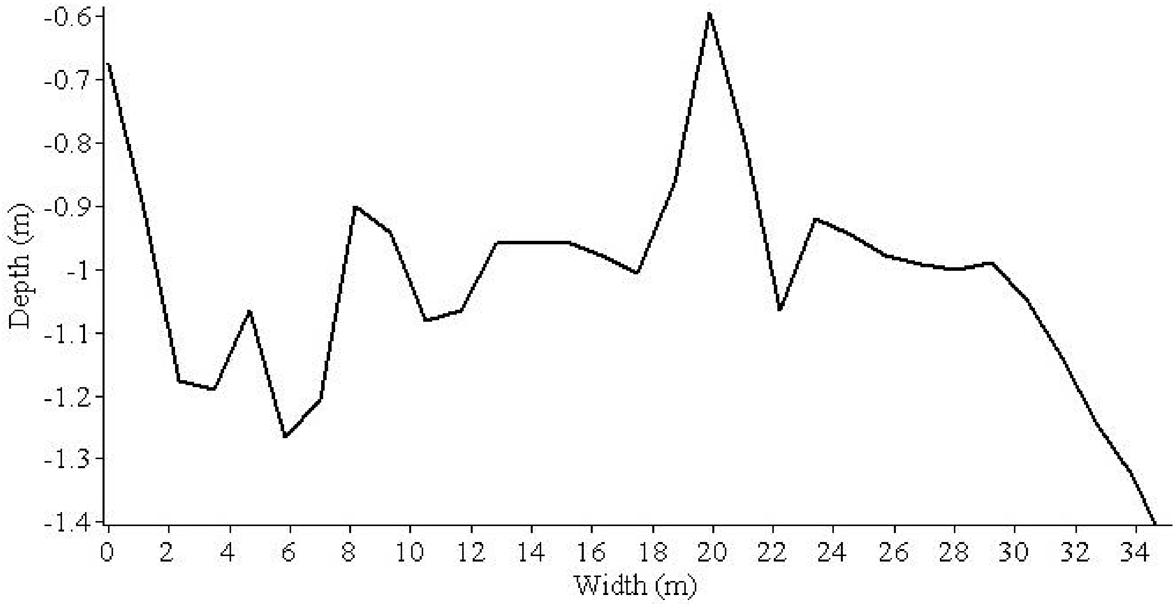

Figure 34: The Nicolet River water depth cross-section at location A of Figure 33

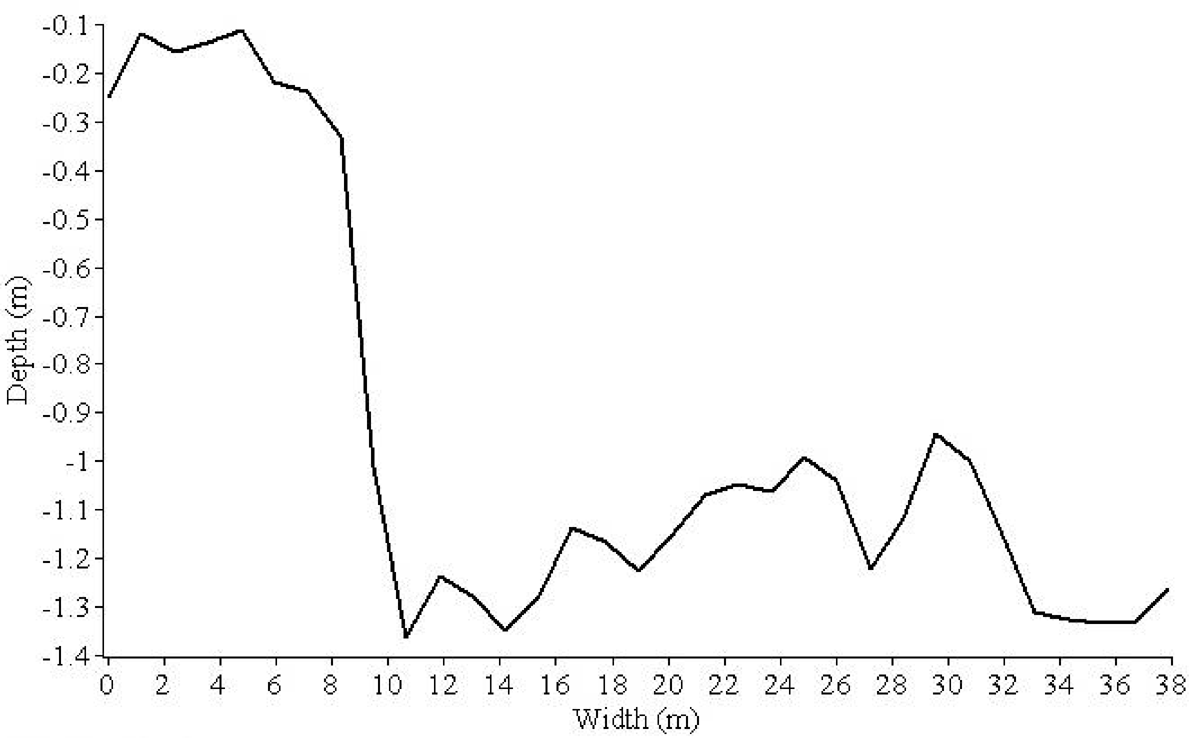

Figure 35: The Nicolet River water depth cross-section at location B of Figure 33

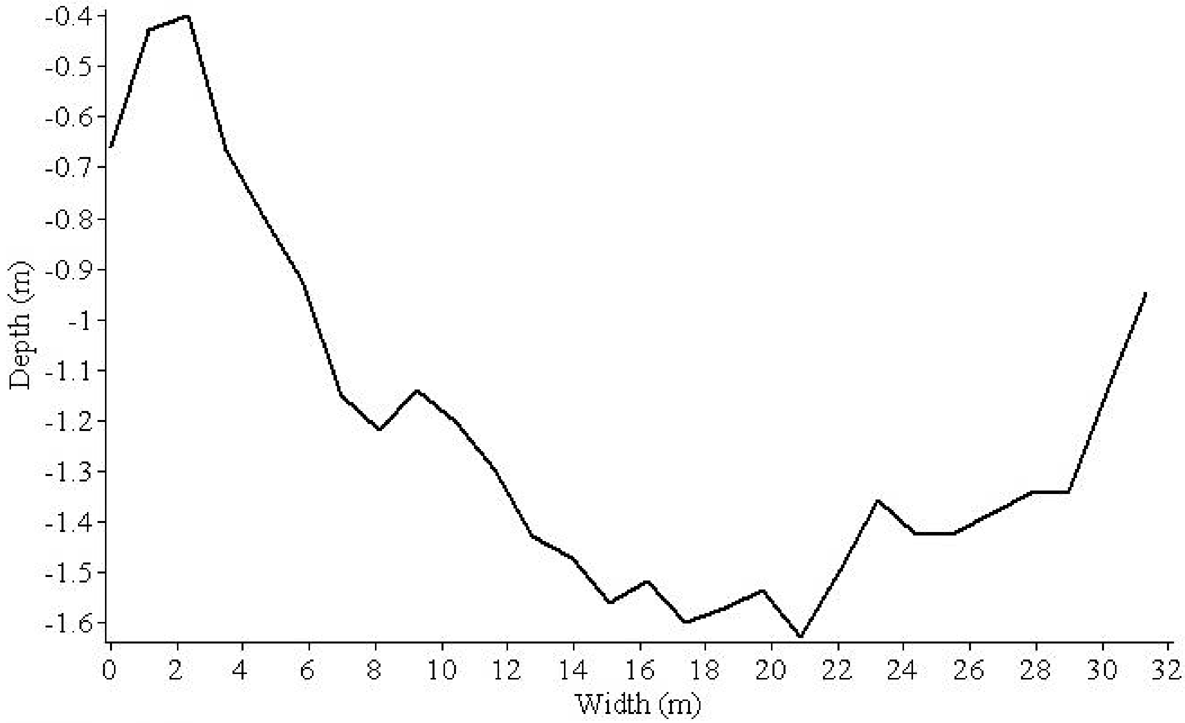

Figure 36: The Nicolet River water depth cross-section at location C of Figure 33

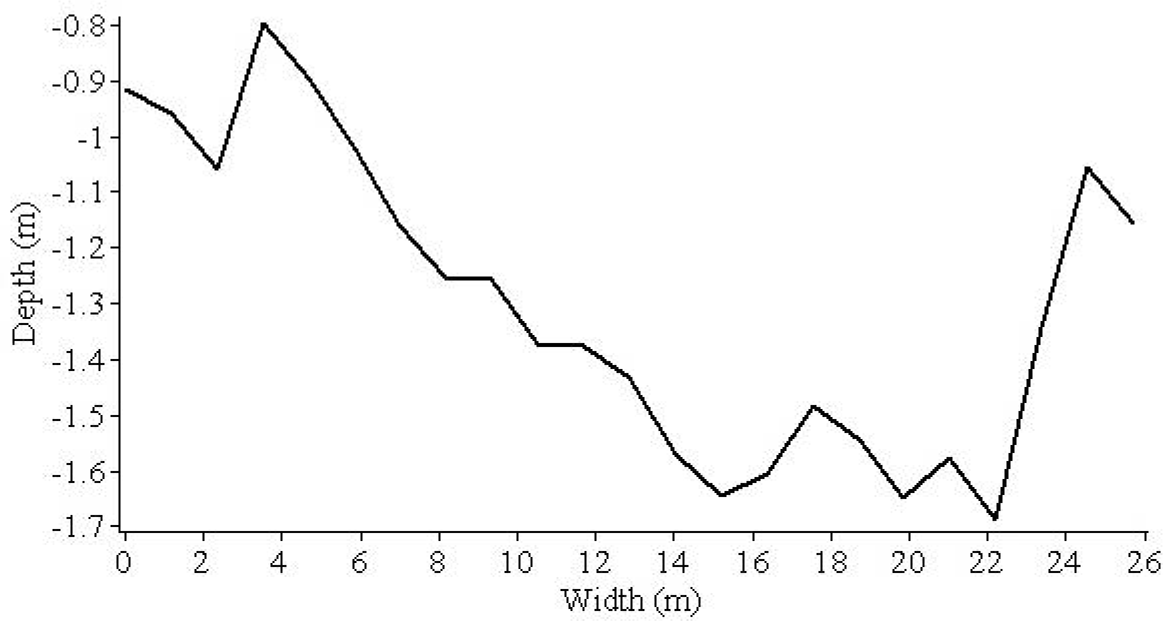

Figure 37: The Nicolet River water depth cross-section at location D of Figure 33

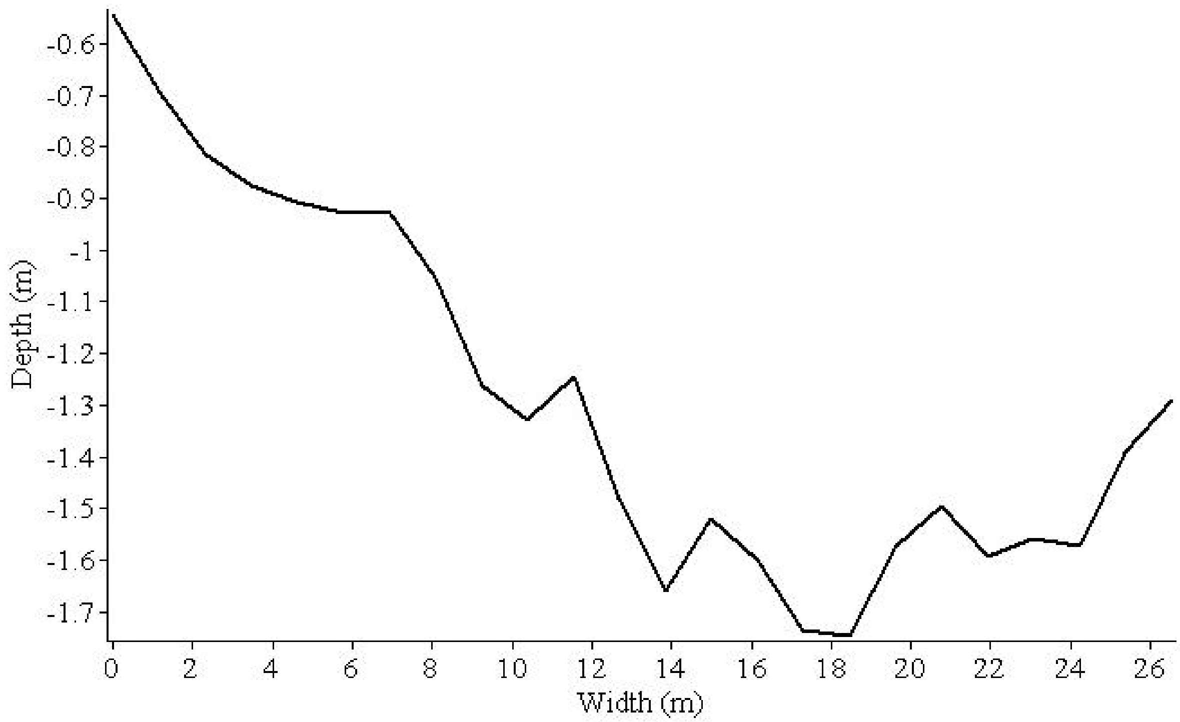

Figure 38: The Nicolet River water depth cross-section at location E of Figure 33

Similar to Figure 33, Figure 39 shows varying water depths corresponding to the riverbed elevations plotted in Figure 30a. In Figures 40 to 44, the riverbed elevations at five selected cross-sections, marked as A, B, C, D and E in Figure 39, are shown. The data shown in the figures is listed in Appendix B. The distributions of riverbed elevations in Figures 33 and 39 consisted of discrete pixel values in the channel section. The WorldView-3 satellite provides images at a 1.2-m resolution. Thus, each pixel covered an area of 1.2 m × 1.2 m on the ground. The limitation is that the riverbed elevation calculated for a pixel is a single value for the entire 1.2 m × 1.2 m area on the ground. In realty, the depths may change from point to point within the area. This explains why the stating depth at some cross sections or the ending depth or both are not zero. With an image resolution of 1.2 m, the first and the last pixel of a cross-section introduce approximations to the near-riverbank geometry. The approximations can be too crude for certain applications, an example of which is the study of bank erosion.

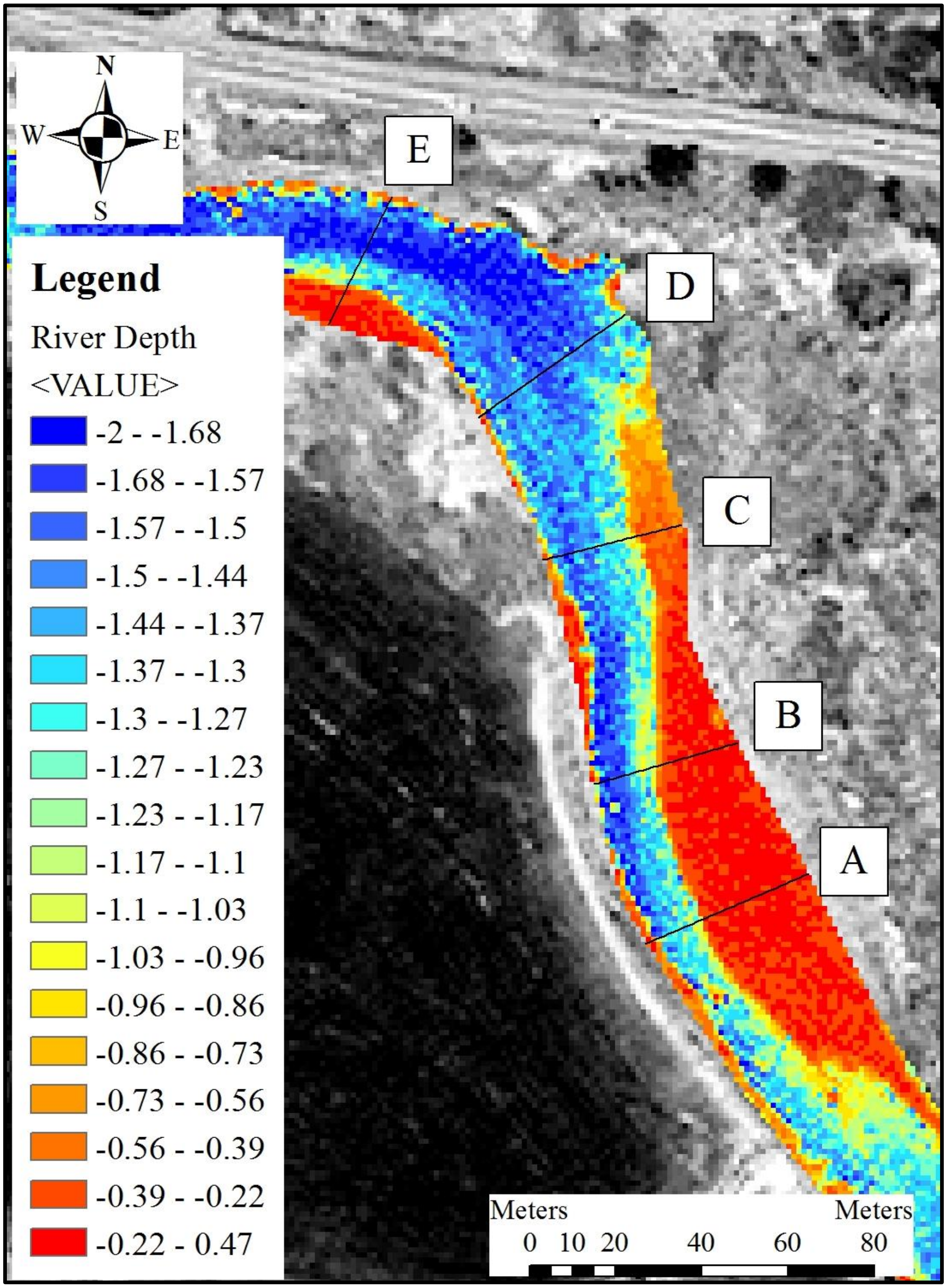

Figure 39: The Nicolet River water depth corresponding to Figure 30a and locations of five selected cross-sections.

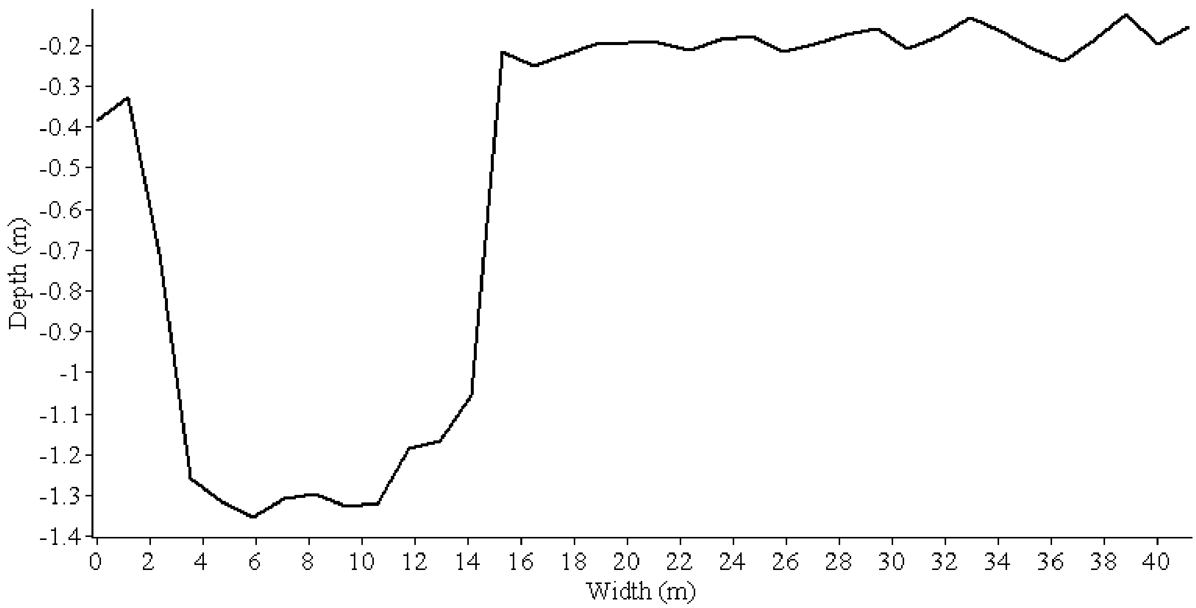

Figure 40: The Nicolet River water depth cross-section at location A of Figure 39

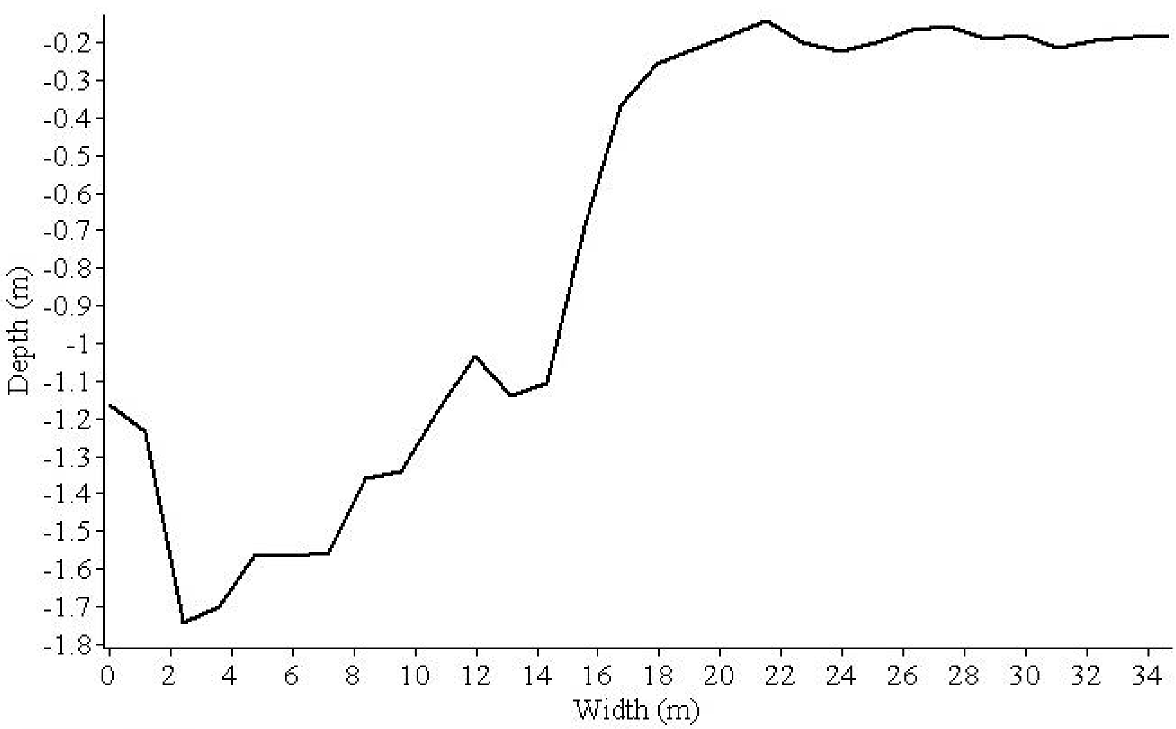

Figure 41: The Nicolet River water depth cross-section at location B of Figure 39

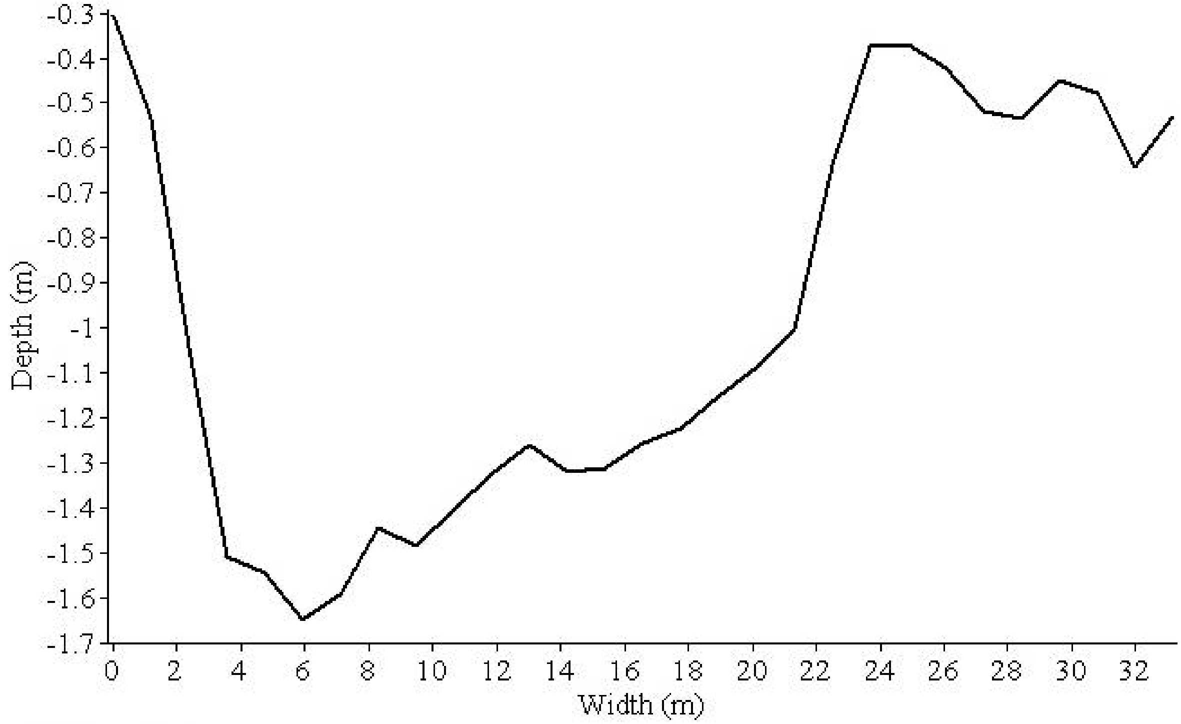

Figure 42: The Nicolet River water depth cross-section at location C of Figure 39

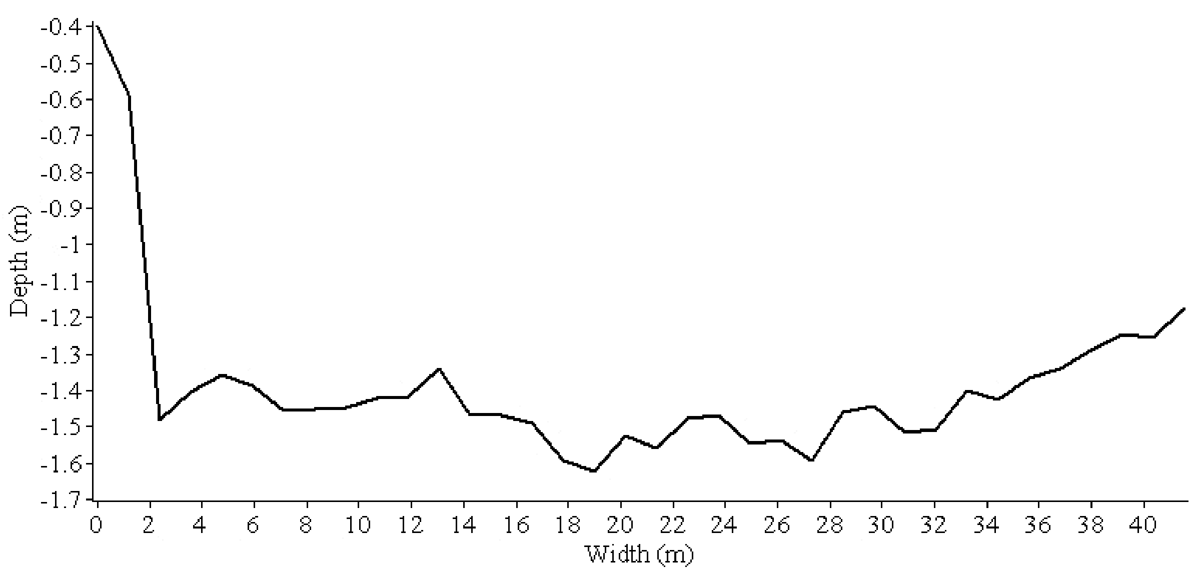

Figure 43: The Nicolet River water depth cross-section at location D of Figure 39

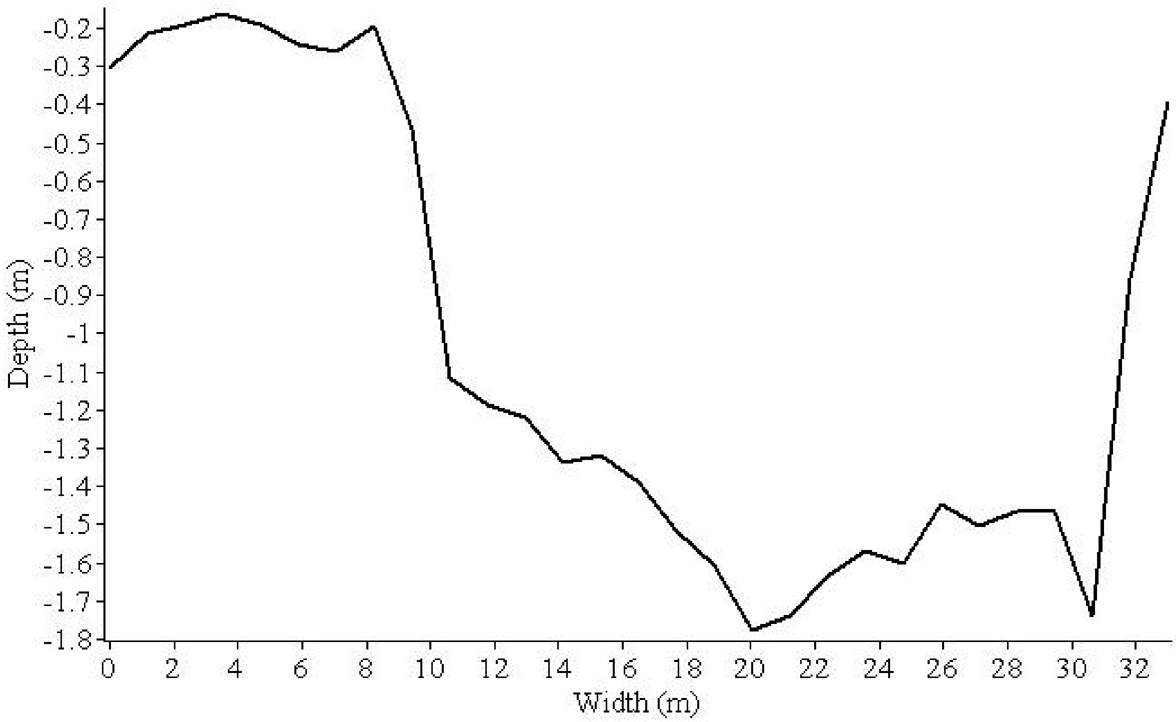

Figure 44: The Nicolet River water depth cross-section at location E of Figure 39

5 DISCUSSION

5.1 Advantages of methods without the need for survey data calibration

Different methodologies for producing river bathymetry have been reported in the literature (Baban 1993; Niroumand-Jadidi et al. 2020). Some are completely based on direct field measurements. The main issue is that field measurements are time-consuming and costly to make. Some combine remote sensing data with field measurements from some locations within the river site in question. A significant limitation is that the methods cannot easily be applied to remote river sites as field measurements are typically not available. Others combine physical laws with field measurements. It is well-known that the physical laws introduce approximations and thus have their uncertainties. Thus, it is desirable to develop new analytical methods for mapping river bathymetry, which do not rely on the availability of field measurements.

Such analytical methods exist in ocean applications, but it is not known how well they work in river applications. The river environment features much stronger spatial variations in bathymetry than the ocean environment. Inspired by successful studies of oceanic and coastal water bathymetry, this study follows a set of analytical relationships for calculations of river flow depth. The calculations start from a general equation from Lambert-Beer's law and select a pair of wavelengths as input to a ratio algorithm. The key challenge encountered in river applications is the determination of the attenuation coefficient and relevant parameters. This study initiated the quest for reliable relationships for determining the coefficient. Applications to oceans and coastal waters have produced some analytical/semi-analytical relationships, expressed by a set of equations for calculating the attenuation coefficient. However, these equations involve many technical factors (e.g., parameters of satellite's optical sensor for recording solar radiances, offset and gain of wavelengths, solar angle and so on) and/or environmental factors (e.g., turbidity of river water, riverbed condition, cloud coverage, tree canopy and so on) that can cause errors in the results of bathymetry.

5.2 Selection of bands

The best pair of bands to use in the ratio algorithm was found through examining all possible band combinations in the visible spectrum. A total of 12 possible combinations were examined. They include using the ratios of the coastal blue band, the blue band, the green band and the red band to the yellow band. In the coastal blue and blue bands, the wavelengths are lower than 550 nm. They are not a suitable option because with these bands, we needed to consider the absorption of radiance by suspended particles. Therefore, band combinations involving the blue band and coastal blue band were excluded because of their wavelengths of less than 550 nm. We found that for WorldView-3 images, among all the remaining band combinations, the red band and the green band provide the bathymetry in the best agreement with available measurements of riverbed elevations. The other band combinations gave either completely inaccurate results or results that are not as accurate as the red and green band combination. For example, the combinations of the yellow and green bands or the yellow and red bands for the WorldView-3 image produced elevation results far different from the field measurements. Our calculations show that the combinations of the yellow and green bands and the yellow and red bands gave effective attenuation coefficients of 43.9999 and 43.5338, respectively. These effective attenuation coefficients resulted in elevations hundred times larger than the expected values.

For WorldView-2 images, using the ratio of the red band to the green band underestimated riverbed elevations. Instead of the red band, we used the yellow band, which penetrates better in water, and improved the results. For WorldView-2 images, the yellow band led to better results, possibly because the turbidity condition of the Nicolet River requires a band with stronger penetration.

5.3 Increased accuracy by applying radiometric and transmission corrections

This study explored possible ways to eliminate or reduce errors in retrieved river bathymetry without relying on field data for calibration. As a beam of sunlight passes through the atmosphere and water column, it is subject to the effects of absorption and scattering in these environments. Therefore, these effects must be considered in the calculation to increase the accuracy of bathymetry results. This study addressed the issue of atmospheric effects through radiometric corrections and the issue of water effects through a series of equations.

Radiometric corrections are fundamental corrections that are applied to all pixels of a satellite image. These corrections affect not only the value of band ratio in the ratio algorithm directly but also the attenuation coefficient indirectly. Radiometric corrections can be divided into two main categories: relative corrections, and absolute corrections. The relative radiometric corrections consider climate data and illumination geometry to remove stripe noises, defective lines and non-uniformity (Janzen et al. 2006). The absolute radiometric corrections improve the raw physical scale of digital numbers. The images from the WorldView-2 and WordView-3 satellites covering the Nicolet River are delivered with relatively corrected radiance. Only the absolute radiometric corrections are applied to each band of images in this study. The corrections correlate with the date of the scene in question and the sensor properties of satellites. An absolute radiometric calibration factor and the effective bandwidth are common parameters with different values for both the WorldView-2 and WordView-3 images, which are used in the calculation of absolute radiometric corrections. WordView-2 radiometric correction equations do not use explicit offset and gain values, whereas WordView-3 radiometric correction equations do (Updike and Comp 2010; Kuester 2016).

As water depth increases, the reflectance of bands decreases. For a wavelength band with higher absorption, the natural logarithm of the reflected band decreases faster, compared to a wavelength band with lower absorption (Stumpf et al. 2003). This feature, along with Lambert-Beer's law, helps generate a natural ratio algorithm that can remove the influence of bed type on reflectance (Stumpf et al. 2003). In a band ratio algorithm, it is necessary to use the reflectance of each band. Therefore, the corrected radiance of bands has to be transformed to top-of-atmosphere reflectance. This transformation can be achieved through calculating parameters like the solar zenith angle, Earth-Sun distance, and solar irradiance. These parameters can be different from one satellite to another.

For the Nicolet River, the implementation of radiometric corrections leads to significantly improved results of obtained riverbed elevations. In the pool area between the pair of deflectors, there are 59 pixels in the WorldView-3 image. Before radiometric corrections, 22 pixels gave elevations outside the range of measured values; after radiometric corrections, only 9 pixels gave values outside the range. Thus, the radiometric corrections reduce the percentage of out-of-range data points from 37.3% to 15.3%. In the WorldView-2 image, 40 pixels cover the pool area. After radiometric corrections, 24 out of 40 pixels gave values outside the range or 60% of data points failure to match field measurements. This inaccuracy occurs due to a lack of information about possible gain and offset factors. Therefore, it is not possible to consider all influence parameters in radiometric corrections.

The effects of water on reflected wavelengths are considered in series of semi-analytical equations. Similar to coastal and oceans bathymetry studies, this thesis investigates the effects of backscattering and absorption of river water through the attenuation coefficient (Z. P. Lee, Du, and Arnone 2005). A multiband quasi-analytical algorithm for open coastal waters allows for backscattering and absorption effects in pure water and in the presence of suspended loads (Lee et al. 2002). This study uses wavelengths longer than 550 nm. In these wavelengths, the absorption effect of suspended loads is quite small. Only the absorption effect of pure water needs to be considered.

With regard to backscattering effects, the total backscattering is the sum of the backscattering of pure water and suspended loads. This study uses Morel's (1974) equation which calculates the backscattering coefficient of pure water based on wavelengths. There are several possible wavelengths in each band for use in the equation. This study uses the centre wavelength of each band as the input wavelength to the equation. The results are compared to the experimental values of backscattering coefficient from Buiteveld, Hakvoort, and Donze (1994). We show an excellent comparison between our analytical results and their experimental data. In conclusion, the backscattering coefficient of pure water is valid as calculated based on centre wavelengths.

5.4 Other remote sensing methods and future improvement

It is worth mentioning that Light Detection and Ranging (LiDAR) is also a remote sensing method for examining the surface of the Earth. Similar to other field survey methods, LiDAR requires operators and flights over a target area. This study explores methods without involving operators at a river site and in-situ equipment for depth measurements. This is useful especially for remote locations of inconvenient accessibility. Also, this reduces operational costs and time, which are important issues in mapping river bathymetry. The conventional methods may take long time in mobilisation to and demobilisation from a river site. Thus, they are not feasible for mapping the bathymetry of an extensive region because of the time-consuming process. Even the LiDAR methods are not sufficient enough to cover a large target region.

In the near future, the Surface Water and Ocean Topography (SWOT) mission jointly by NASA and the National Centre for Space Studies of French (CNES), in partnership with the Canadian Space Agency and UK Space Agency, will provide surface water data. SWOT operations will be able to capture images of rivers, and the images will offer an excellent opportunity to efficiently map river bathymetry. Previously, a comparison between optical bathymetry from WorldView-2 images of a lake and in-situ measurements of depth gave correction coefficients of 0.59 to 0.81 (Jawak and Luis 2015). In this study, the retrieved bathymetry achieves acceptable accuracy; 84.7% of data points are within the range of measured values.

In this study, the methods for river bathymetry are new. The methods should be extended to address outstanding issues:

1) The satellite images used in this study are free of cloud coverage. Thus, the effects of cloud shadow should be evaluated in future studies.
2) Along a river channel of longer than 16 km, there is a change in the solar angle. This study uses only one value for the solar angle. Future studies should use changing solar angles when dealing with a long river reach.
3) This study determines the radiation of each band for wet pixels covering the whole river and applies the same radiation to the entire river reach in calculations of involved coefficients. Future studies should calculate local radiations for different parts of the river reach in question and then use them in further analysis.

5.5 Sensitivity of digital elevation model to attenuation coefficient

The attenuation coefficient and involved parameters are not free of errors. How sensitive are the obtained bathymetry to the errors? We test the sensitivity by introducing some percentage changes to the absorption and backscattering coefficients. They affect the attenuation coefficient value and thus the results of obtained riverbed elevation. We consider four scenarios: (1) the absorption coefficient increases in value by 1%, and there is no change to the backscattering coefficient; 2) there is no change to the backscattering coefficient, and the absorption coefficient increases in value by 5%; 3) there is no change to the absorption coefficient, and the backscattering coefficient increases in value by 1%; 4) there is no change to the absorption coefficient, and the backscattering coefficient increases in value by 5%. Table 19 provides a summary of the changes in absorption, backscattering and attenuation coefficients for the green band in WorldView-3 image. Table 20 provides a summary of the changes in absorption, backscattering and attenuation coefficients for the red band in WorldView-3 image.

Table 19: Changes of values for the effective parameters in four different scenarios the green band of the WorldView-3 image

	Absorption coefficient (a)	Backscattering coefficient (b_b)	Attenuation coefficient (k)
Base scenario	0.0677	8.0533	25.3232
Scenario 1 (1% increase in a)	0.0684	8.0533	25.3853
Scenario 2 (5% increase in a)	0.0711	8.0533	25.6296
Scenario 3 (1% increase in b_b)	0.0677	8.1353	25.5756
Scenario 4 (5% increase in b_b)	0.0677	8.4575	26.5855

Table 20: Changes in values for the effective parameters in four different scenarios in the red band of the WorldView-3 image

	Absorption coefficient (a)	Backscattering coefficient (b_b)	Attenuation coefficient (k)
Base scenario	1.1398	5.8592	25.7892
Scenario 1 (1% increase in a)	1.1511	5.8592	25.8022
Scenario 2 (5% increase in a)	1.1968	5.8592	25.8541
Scenario 3 (1% increase in b_b)	1.1398	5.9178	26.0341
Scenario 4 (5% increase in b_b)	1.1398	6.1522	27.0138

Riverbed elevations were obtained in scenarios 1, 2, 3 and 4. Figures 45 to 48 show the results of each scenario in the downstream pool location, covered by 59 pixels.

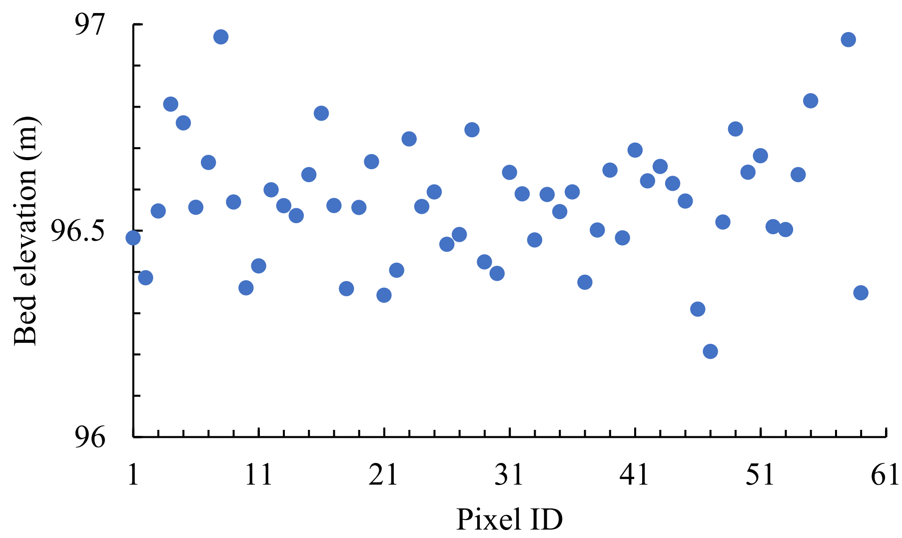

Figure 45: Riverbed elevations in scenario 1 from the WorldView-3 image, with 59 pixels located in the downstream pool.

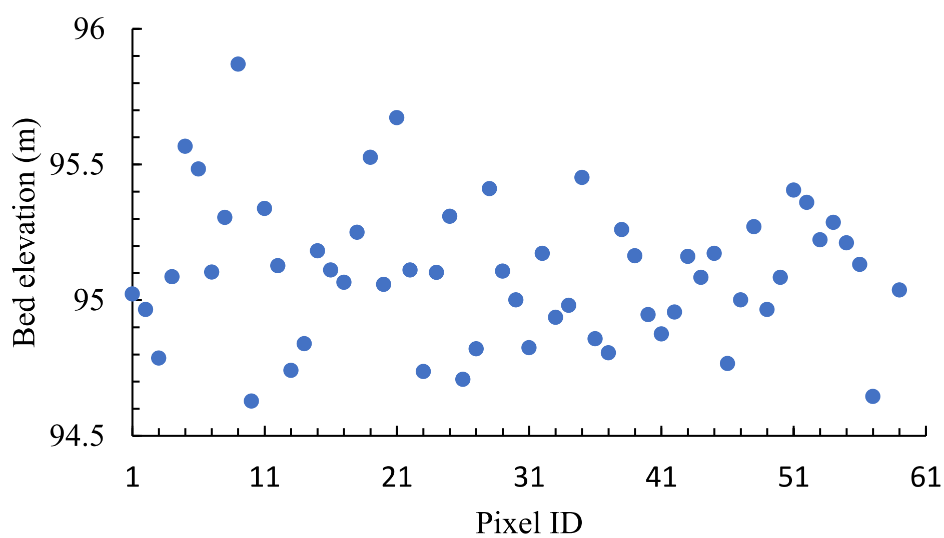

Figure 46: Riverbed elevations in scenario 2 from the WorldView-3 image, with 59 pixels located in the downstream pool.

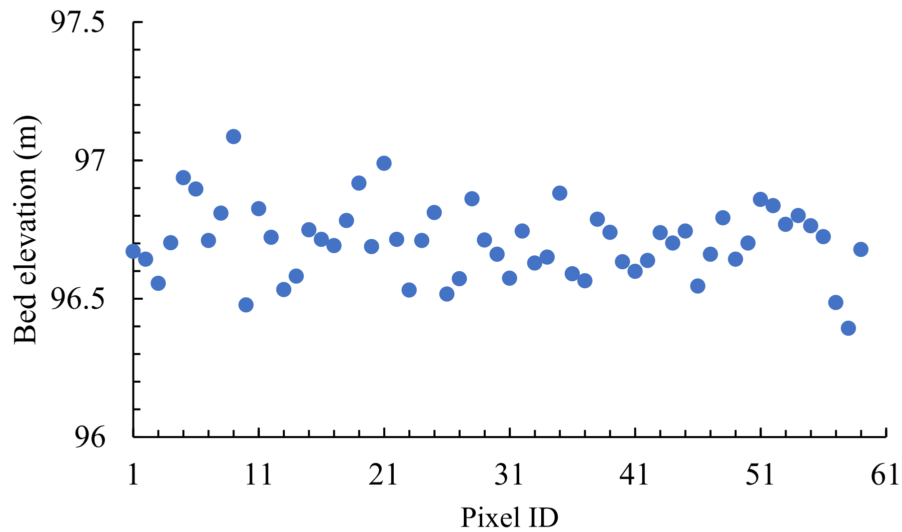

Figure 47: Riverbed elevations in scenario 3 from the WorldView-3 image, with 59 pixels located in the downstream pool.

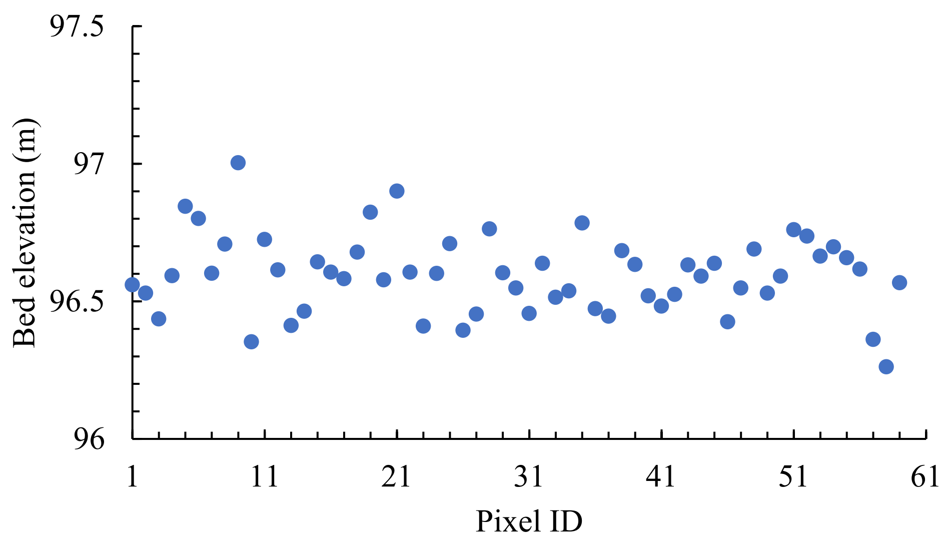

Figure 48: Riverbed elevations in scenario 4 from the WorldView-3 image, with 59 pixels located in the downstream pool.

As shown in Figure 45 shows, a 1% increase in the value of absorption coefficient results in riverbed elevations in two pixels exceeding 97 m, and in 17 pixels dropping below 96.5 m. This means that the 1% increase in the value of absorption coefficient brings the accuracy of the model down from 84.7% to 67.7%. In the scenario of increasing the value of absorption coefficient by

5%, the riverbed elevations in 58 out of 59 pixels drop below 96.5 m. This means that an increase in absorption coefficient value by 5% results in underestimates of riverbed elevations or overestimates of water depth.

In the scenarios that only the backscattering coefficient changes, the obtained riverbed elevations change slightly. In scenario 3, the backscattering coefficient increases in value by 1%, the riverbed elevations in only four pixels have a value out of acceptable range, meaning the accuracy of the obtained bathymetry increases to 93%. A 5% increase in the value of this coefficient can reduce the accuracy to 75%, as the riverbed elevations in 14 pixels have a value below 96.5 m.

The DEM provided for all river points is calculated based on the elevation of a specific datum point station. Therefore, the Nicolet River DEM points are likely to be horizontal. However, we know that rivers have a slope from upstream to downstream, and the elevation of points decreases from upstream to downstream. To consider the river slope and to find the actual elevation of each point in the Nicolet river, it is necessary to add the difference between the elevation of any specific point to the elevation of the datum station. Finding elevation of any point can happen with the help of google earth.

6 CONCLUSIONS

This research work has contributed to the development of new methods for mapping river bathymetry from high-resolution satellite images. The methods are applied to a 25-km reach of the Nicolet River in Quebec. Important concluding remarks from this work are summarised below:

1) The new methods differ from previous methods for retrieving river bathymetric data from satellite images. The previous methods rely on field measurements for the calibration of regression relationships, whereas the new methods do not. Therefore, the new methods can be applied to a remote river reach, which satellite images may cover and from which field measurements may not be available.
2) One way to enhance the accuracy of the new methods is to use data of radiance coming from wet pixels only, as demonstrated in the application to the Nicolet River. The wet pixels of satellite images covering the river are separated from the rest of pixels, and the radiance of each frequency band is determined for further analysis.
3) Using radiance records from satellite sensors directly to derive river bathymetry does not produce the most accurate results. This is because sunlight is absorbed and scattered during its journey through the atmosphere and water column. The radiance records should be corrected in order to remove atmospheric effects by considering gain, offset and absolute radiometric calibration factors (Eq. 40). The records should be converted to values at the top of atmosphere reflectance (Eq. 41). The reason is that the ratio band algorithm uses band reflectance as pixel value.
4) A general equation for the light attenuation coefficient is adopted from ocean studies. The coefficient allows for the effects of absorption and backscattering by water on wavelengths. With this equation, it is possible to correct radiances that come out of water column in the ratio algorithm. This idea is new in river studies. A comparision of results between before and after radiometric correction of visible bands (Figs 16 and 23 for WorldView-2 image; Figs 17 and 24 for WorldView-3 image) shows noticeable changes to band pixel values.
5) Without radiometric correction, the results of bathymetry dervied from WorldView-3 image are less comparable with available field measurements (Fig. 22) than with the radiometric correction. For WorldView-2 image, the radiometric correction (Eq. 39) does

not include gain and offset effects, and thus the results are not as accurate as those from WorldView-3 image.

6) A shortcoming of deriving river bathymetry from satellite images is the discontiuity in flow depths across a channel cross-section from one riverbank to the other. The depths do not always start from zero value at one riverbank and end with zero value at the other. For example, each pixel of a WorldView-3 image provides a single value for a horizontal area of 1.2×1.2 m^2. The river bathymetry is mapped by connecting discreet pixel values.

REFERENCES

Agapiou, Athos, and Vasiliki Lysandrou. 2015. “Remote Sensing Archaeology : Tracking and Mapping Evolution in European Scientific Literature from 1999 to 2015.” *Journal of Archaeological Science* 4:192–200. doi: 10.1016/j.jasrep.2015.09.010.

Baban, Serwan M. J. 1993. “The Evaluation of Different Algorithms for Bathymetric Charting of Lakes Using Landsat Imagery.” *International Journal of Remote Sensing* 14(12):2263–73. doi: 10.1080/01431169308954035.

Barsi, Julia A., Simon J. Hook, John R. Schott, Nina G. Raqueno, and Brian L. Markham. 2007. “Landsat-5 Thematic Mapper Thermal Band Calibration Update.” *IEEE Geoscience and Remote Sensing Letters* 4(4):552–55. doi: 10.1109/LGRS.2007.896322.

Bierwirth, P. N., T. J. Lee, and R. V. Burne. 1993. “Shallow Sea-Floor Reflectance and Water Depth Derived by Unmixing Multispectral Imagery.” *Photogrammetric Engineering & Remote Sensing* 59(3):331–38.

Buiteveld, Hendrik, J. H. M. Hakvoort, and M. Donze. 1994. “Optical Properties of Pure Water.” Pp. 174–83 in *Ocean Optics XII*. Vol. 2258.

Campbell, James B., and Randolph H. Wynne. 2011. *Introduction to Remote Sensing FIFTH EDITION*. Vol. XXXIII.

Carré, David M., Pascale M. Biron, and Susan J. Gaskin. 2007. “Flow Dynamics and Bedload Sediment Transport around Paired Deflectors for Fish Habitat Enhancement: A Field Study in the Nicolet River.” *Canadian Journal of Civil Engineering* 34(6):761–69. doi: 10.1139/L06-083.

Chen, Jian-feng, James A. Zagzebski, and Ernest L. Madsen. 1993. “Tests of Backscatter Coefficient Measurement Using Broadband Pulses.” *IEEE Transactions on Ultrasonics, Ferroelectrics, and Frequency Control* 40(5):603–7.

Farr, Harold K. 1980. “Multibeam Bathymetric Sonar: Sea Beam and Hydro Chart.” *Marine Geodesy* 4(2):77–93. doi: 10.1080/15210608009379375.

Feurer, Denis, Jean Stéphane Bailly, Christian Puech, Yann Le Coarer, and Alain A. Viau. 2008.

“Very-High-Resolution Mapping of River-Immersed Topography by Remote Sensing.” *Progress in Physical Geography* 32(4):403–19. doi: 10.1177/0309133308096030.

Harada, Sho, and S. Samuel Li. 2018. “Combining Remote Sensing with Physical Flow Laws to Estimate River Channel Geometry.” *River Research and Applications* 34(October 2017):697–708. doi: 10.1002/rra.3298.

Janzen, Darren T., Arthur L. Fredeen, and Roger D. Wheate. 2006. “Radiometric Correction Techniques and Accuracy Assessment for Landsat TM Data in Remote Forested Regions.” *Canadian Journal of Remote Sensing* 32(5):330–40. doi: 10.5589/m06-028.

Jawak, S. D., and A. J. Luis. 2015. “Spectral Information Analysis for the Semiautomatic Derivation of Shallow Lake Bathymetry Using High-Resolution Multispectral Imagery: A Case Study of Antarctic Coastal Oasis.” *Aquatic Procedia* 4(Icwrcoe):1331–38. doi: 10.1016/j.aqpro.2015.02.173.

Jupp, D. L. B. 1989. “Background and Extensions to Depth of Penetration (DOP) Mapping in Shallow Coastal Waters.” in *Proceedings of Remote Sensing of the Coastal Zone International Symposium*.

Kuester, Michele. 2016. *Radiometric Use of WorldView - 3 Imagery Technical Note*.

Langhorst, Theodore, Tamlin M. Pavelsky, Renato Prata de Moraes Frasson, Rui Wei, Alessio Domeneghetti, Elizabeth H. Altenau, Michael T. Durand, J. Toby Minear, Karl W. Wegmann, and Matthew R. Fuller. 2019. “Anticipated Improvements to River Surface Elevation Profiles From the Surface Water and Ocean Topography Mission.” *Frontiers in Earth Science* 7:1–13. doi: 10.3389/feart.2019.00102.

Lee, Zhong-ping, Miroslaw Darecki, Kendall L. Carder, Curtiss O. Davis, Dariusz Stramski, and W. Joseph Rhea. 2005. “Diffuse Attenuation Coefficient of Downwelling Irradiance : An Evaluation of Remote Sensing Methods.” *Journal of Geophysical Research* 110:1–9. doi: 10.1029/2004JC002573.

Lee, Zhong Ping, Ke Ping Du, and Robert Arnone. 2005. “A Model for the Diffuse Attenuation Coefficient of Downwelling Irradiance.” *Journal of Geophysical Research* 110:1–10. doi: 10.1029/2004JC002275.

Lee, Zhongping, Kendall L. Carder, and Robert A. Arnone. 2002. “Deriving Inherent Optical Properties from Water Color : A Multiband Quasi- Analytical Algorithm for Optically Deep Waters.” *Applied Optics* 41(27):5755–72. doi: 10.1364/AO.41.005755.

Legleiter, C. J., and B. T. Overstreet. 2012. “Mapping Gravel Bed River Bathymetry from Space.” *Journal of Geophysical Research* 117:1–24. doi: 10.1029/2012JF002539.

Legleiter, Carl J., Dar A. Roberts, and Rick L. Lawrence. 2009. “Spectrally Based Remote Sensing of River Bathymetry.” *Earth Surface Processes and Landforms* 34:1039–59. doi: 10.1002/esp.

Lyzenga, David R. 1978. “Passive Remote Sensing Techniques for Mapping Water Depth and Bottom Features.” *Applied Optics* 17(3):379–83. doi: 10.1364/ao.17.000379.

Matsuda, Iware. 2004. “River Morphology And Channel Processes.” *Fresh Surface Water* 1:1–12.

McFeeters, S. K. 1996. “The Use of the Normalized Difference Water Index (NDWI) in the Delineation of Open Water Features.” *International Journal of Remote Sensing* 17(7):1425–32. doi: 10.1080/01431169608948714.

Meeus, Jean. 1998. *Astronomical Algorithms*. Second. Richmond, Virgina: Willmann-Bell.

Morel, Andre. 1974. *Optical Properties of Pure Water and Pure Seawater, in: Optical Aspects of Oceanography*. edited by N. G. Jerlov and E. Steemann Nielson. New York.

Natural Resources Canada. 2020. *Height Reference System Modernization Information about the Canadian Geodetic Vertical Datum of 2013 (CGVD2013)*. Vol. 2.

Ng, Karen Pei-Talc. 2005. “Two-Dimensional Hydraulic-Habitat Modeling of a Rehabilitated River.”

Niroumand-Jadidi, M., and A. Vitti. 2016. “Optimal Band Ratio Analysis of Worldview-3 Imagery For Bathymetry of Shallow Rivers (Case Study : Sarca River , Italy).” Pp. 361–64 in *The International Archives of the Photogrammetry, Remote Sensing and Spatial Information Sciences*. Vols. XLI-B8.

Niroumand-Jadidi, Milad, Francesca Bovolo, and Lorenzo Bruzzone. 2020. “SMART-SDB: Sample-Specific Multiple Band Ratio Technique for Satellite-Derived Bathymetry.” *Remote*

Sensing of Environment 251:1–13. doi: 10.1016/j.rse.2020.112091.

Parente, Claudio, and Massimiliano Pepe. 2018. "Bathymetry From Worldview-3 Satellite Data Using Radiometric Band Ratio." *Acta Polytechnica* 58(2):109–17. doi: 10.14311/AP.2018.58.0109.

Philpot, William D. 1989. "Bathymetric Mapping with Passive Multispectral Imagery." *Applied Optics* 28(8):1569–78. doi: 10.1364/ao.28.001569.

Polcyn, F. .., W. L. Brown, and I. J. Sattinger. 1970. *The Measurement of Water Depth by Remote Sensing Techniques*. MICHIGAN: Willow Run Laboratories.

Quadros, N. .., P. .. Collier, and C. S. Fraser. 2008. "Integration of Bathymetric and Topographic Lidar: A Preliminary Investigation." *The International Archives of the Photogrammetry Remote Sensing and Spatial Information Sciences Beijing 2008* XXXVII(B8):1299–1304.

Shah, Ankit, Benidhar Deshmukh, and L. K. Sinha. 2020. "A Review of Approaches for Water Depth Estimation with Multispectral Data." *World Water Policy* 6:152–67. doi: 10.1002/wwp2.12029.

Shields, F. Douglas, Charles M. Cooper, and Scott S. Knight. 1995. "Experiment in Stream Restoration." *Journal of Hydraulic Engineering* 121(6):494–502. doi: 10.1061/(asce)0733-9429(1995)121:6(494).

Stumpf, Richard P., Kristine Holderied, and Mark Sinclair. 2003. "Determination of Water Depth with High-Resolution Satellite Imagery over Variable Bottom Types." *Limnology and Oceanography* 48(1, part 2):547–56.

Tripathi, N. K., and A. M. Rao. 2002. "Bathymetric Mapping in Kakinada Bay, India, Using IRS-1D LISS-III Data." *International Journal of Remote Sensing* 23(6):1013–25. doi: 10.1080/01431160110075785.

U.S. Geological Survey. 1998. *US GeoData Digital Elevation Models*. Vol. 1927.

United States Geological Survey. 1997. *Landsat Data A Brief History of the Landsat Program*.

Updike, Todd, and Chris Comp. 2010. *Radiometric Use of WorldView-2 Imagery Technical Note*.

Vaze, Parag, Said Kaki, Daniel Limonadi, Daniel Esteban-Fernandez, and Guy Zohar. 2018. “The Surface Water and Ocean Topography Mission.” Pp. 1–9 in *IEEE Aerospace Conference*. IEEE.

Wang, Chisheng, Qingquan Li, Yanxiong Liu, Guofeng Wu, Peng Liu, and Xiaoli Ding. 2015. “A Comparison of Waveform Processing Algorithms for Single-Wavelength LiDAR Bathymetry.” *ISPRS Journal of Photogrammetry and Remote Sensing* 101:22–35. doi: 10.1016/j.isprsjprs.2014.11.005.

Wiyanarti, E. 2018. “River and Civilization in Sumatera’s Historical Perspective in the 7th to 14th Centuries.” in *IOP Conference Series: Earth and Environmental Science*. Vol. 145.

Yalin, MS. 2015. *River Mechanics*. Oxford: Pergamon Press.

APPENDIXES

Appendix A: Data of depth varying at across cross-sections marked in Figure 33.

Table A21: Depths varying across the width at cross-section A of Figure 33

Width (m)	Depth (m)	Width (m)	Depth (m)
0	-0.6744	28.0459	-1.0014
1.1686	-0.9059	29.2145	-0.9898
2.3372	-1.1748	30.383	-1.0475
3.5057	-1.1888	31.5516	-1.1388
4.6743	-1.0648	32.7202	-1.2456
5.8429	-1.2641	33.8888	-1.3261
7.0115	-1.2055	35.0574	-1.4466
8.1801	-0.9002		
9.3486	-0.9425		
10.5172	-1.0813		
11.6858	-1.0646		
12.8544	-0.9586		
14.0229	-0.9585		
15.1915	-0.9562		
16.3601	-0.9783		
17.5287	-1.0073		
18.6973	-0.8636		
19.8658	-0.5933		
21.0344	-0.7958		
22.203	-1.0656		
23.3716	-0.9186		
24.5402	-0.9448		
25.7087	-0.9779		
26.8773	-0.9934		

Table A22: Depths varying across the width at cross-section B of Figure 33

Width (m)	Depth (m)	Width (m)	Depth (m)
0	-0.2493	31.9488	-1.1531
1.1833	-0.1156	33.1321	-1.3134
2.3666	-0.155	34.3154	-1.3288
3.5499	-0.1377	35.4987	-1.3346
4.7332	-0.1098	36.682	-1.3299
5.9164	-0.2166	37.8652	-1.2628
7.0997	-0.2382		
8.283	-0.3301		
9.4663	-1.0121		
10.6496	-1.3645		
11.8329	-1.2392		
13.0162	-1.2787		
14.1995	-1.3513		
15.3828	-1.2791		
16.566	-1.138		
17.7493	-1.1685		
18.9326	-1.2271		
20.1159	-1.1559		
21.2992	-1.0698		
22.4825	-1.0481		
23.6658	-1.0619		
24.8491	-0.9933		
26.0324	-1.0415		
27.2156	-1.2243		
28.3989	-1.1172		
29.5822	-0.9426		
30.7655	-0.9995		

Table A23: Depths varying across the width at cross-section C of Figure 33

Width (m)	Depth (m)
0	-0.6597
1.1603	-0.4264
2.3206	-0.3996
3.481	-0.6661
4.6413	-0.7988
5.8016	-0.9216
6.9619	-1.152
8.1223	-1.2192
9.2826	-1.1398
10.4429	-1.2051
11.6032	-1.2947
12.7636	-1.4265
13.9239	-1.471
15.0842	-1.5585
16.2445	-1.516
17.4048	-1.5978
18.5652	-1.5706
19.7255	-1.5338
20.8858	-1.627
22.0461	-1.4943
23.2065	-1.3559
24.3668	-1.4239
25.5271	-1.4207
26.6874	-1.3801
27.8478	-1.3434
29.0081	-1.3391
30.1684	-1.1366
31.3287	-0.9476

Table A24: Depths varying across the width at cross-section D of Figure 33

Width (m)	Depth (m)
0	-0.9163
1.1688	-0.9595
2.3376	-1.0603
3.5064	-0.7968
4.6752	-0.8956
5.844	-1.0223
7.0128	-1.1582
8.1816	-1.2524
9.3504	-1.2566
10.5192	-1.3731
11.688	-1.3763
12.8567	-1.4315
14.0255	-1.5674
15.1943	-1.6457
16.3631	-1.6038
17.5319	-1.4819
18.7007	-1.5435
19.8695	-1.6491
21.0383	-1.5767
22.2071	-1.6876
23.3759	-1.3432
24.5447	-1.0548
25.7135	-1.1552

Table A25: Depths varying across the width at cross-section E of Figure 33

Width (m)	Depth (m)
0	-0.5448
1.1538	-0.6957
2.3076	-0.8129
3.4613	-0.874
4.6151	-0.9079
5.7689	-0.9277
6.9227	-0.9245
8.0764	-1.0549
9.2302	-1.2613
10.384	-1.3281
11.5378	-1.2463
12.6915	-1.4809
13.8453	-1.6597
14.9991	-1.5194
16.1529	-1.6015
17.3066	-1.735
18.4604	-1.7462
19.6142	-1.5714
20.768	-1.4966
21.9217	-1.5943
23.0755	-1.5594
24.2293	-1.5708
25.3831	-1.3915
26.5368	-1.29

Appendix B: Data of depth varying at across cross-sections marked in Figure 39

Table B26: Depths varying across the width at cross-section A of Figure 39

Width (m)	Depth (m)	Width (m)	Depth (m)
0	-0.3828	30.6078	-0.2087
1.1772	-0.3256	31.785	-0.1779
2.3544	-0.7095	32.9622	-0.1311
3.5317	-1.258	34.1395	-0.1678
4.7089	-1.3154	35.3167	-0.2105
5.8861	-1.3534	36.4939	-0.2377
7.0633	-1.3074	37.6711	-0.1844
8.2406	-1.2957	38.8484	-0.1248
9.4178	-1.3285	40.0256	-0.1973
10.595	-1.3186	41.2028	-0.157
11.7722	-1.1839		
12.9495	-1.1667		
14.1267	-1.0554		
15.3039	-0.218		
16.4811	-0.25		
17.6583	-0.2232		
18.8356	-0.1977		
20.0128	-0.1941		
21.19	-0.1952		
22.3672	-0.2112		
23.5445	-0.1842		
24.7217	-0.1781		
25.8989	-0.2173		
27.0761	-0.198		
28.2534	-0.1736		
29.4306	-0.1582		

Table B27: Depths varying across the width at cross-section B of Figure 39

Width (m)	Depth (m)	Width (m)	Depth (m)
0	-1.165	33.4612	-0.1836
1.195	-1.2332	34.6563	-0.1843
2.3901	-1.7436		
3.5851	-1.6996		
4.7802	-1.5592		
5.9752	-1.5652		
7.1703	-1.5549		
8.3653	-1.3588		
9.5604	-1.3411		
10.7554	-1.1845		
11.9504	-1.0353		
13.1455	-1.1409		
14.3405	-1.1077		
15.5356	-0.6867		
16.7306	-0.3667		
17.9257	-0.2554		
19.1207	-0.22		
20.3157	-0.1781		
21.5108	-0.1415		
22.7058	-0.1994		
23.9009	-0.2254		
25.0959	-0.2001		
26.291	-0.1654		
27.486	-0.157		
28.6811	-0.1905		
29.8761	-0.1806		
31.0711	-0.2139		
32.2662	-0.1945		

Table B28: Depths varying across the width at cross-section C of Figure 39

Width (m)	Depth (m)	Width (m)	Depth (m)
0	-0.3054	33.1616	-0.5297
1.1843	-0.5351		
2.3687	-1.0438		
3.553	-1.5089		
4.7374	-1.5455		
5.9217	-1.6497		
7.1061	-1.5954		
8.2904	-1.4454		
9.4747	-1.485		
10.6591	-1.4063		
11.8434	-1.3234		
13.0278	-1.2604		
14.2121	-1.3198		
15.3964	-1.3133		
16.5808	-1.2556		
17.7651	-1.2249		
18.9495	-1.1515		
20.1338	-1.0871		
21.3182	-1.0022		
22.5025	-0.637		
23.6868	-0.3731		
24.8712	-0.3689		
26.0555	-0.4226		
27.2399	-0.518		
28.4242	-0.5338		
29.6086	-0.4495		
30.7929	-0.4791		
31.9772	-0.644		

Table B29: Depths varying across the width at cross-section D of Figure 39

Width (m)	Depth (m)	Width (m)	Depth (m)
0	-0.3992	33.2438	-1.3982
1.1873	-0.5856	34.4311	-1.4267
2.3746	-1.4811	35.6184	-1.3661
3.5618	-1.4038	36.8056	-1.3404
4.7491	-1.359	37.9929	-1.2888
5.9364	-1.3877	39.1802	-1.2458
7.1237	-1.456	40.3675	-1.2545
8.311	-1.4526	41.5548	-1.172
9.4982	-1.4465		
10.6855	-1.4228		
11.8728	-1.4154		
13.0601	-1.3415		
14.2473	-1.4689		
15.4346	-1.4662		
16.6219	-1.4886		
17.8092	-1.5907		
18.9965	-1.6222		
20.1837	-1.523		
21.371	-1.5565		
22.5583	-1.4756		
23.7456	-1.4663		
24.9329	-1.5438		
26.1201	-1.5352		
27.3074	-1.5942		
28.4947	-1.4587		
29.682	-1.4446		
30.8692	-1.5132		
32.0565	-1.5079		

Table B30: Depths varying across the width at cross-section E of Figure 39

Width (m)	Depth (m)	Width (m)	Depth (m)
0	-0.3035	32.9978	-0.395
1.1785	-0.2163		
2.357	-0.1907		
3.5355	-0.1621		
4.714	-0.1908		
5.8925	-0.241		
7.071	-0.2634		
8.2495	-0.1951		
9.4279	-0.4646		
10.6064	-1.1158		
11.7849	-1.1873		
12.9634	-1.2176		
14.1419	-1.3357		
15.3204	-1.3206		
16.4989	-1.3876		
17.6774	-1.5169		
18.8559	-1.6069		
20.0344	-1.777		
21.2129	-1.7393		
22.3914	-1.6332		
23.5699	-1.5669		
24.7484	-1.6004		
25.9269	-1.4466		
27.1053	-1.5054		
28.2838	-1.4661		
29.4623	-1.4653		
30.6408	-1.7376		
31.8193	-0.8567		

Appendix C: DEM of the entire river reach from WorldView-3 image

Sample rows of DEM are shown below. The complete data sheet is in a separate file.

FID	Shape	Point-ID	Bed-Elevation	Easting	Northing
(-)	(-)	(-)	(m)	(m)	(m)
0	Point	1	97.602104	274303.799694	5100310.19999899
1	Point	2	97.130554	274301.399694	5100308.99999899
2	Point	3	97.083336	274300.199694	5100307.79999899
3	Point	4	97.116653	274301.399694	5100307.79999899
4	Point	5	97.089088	274297.799694	5100306.59999899
5	Point	6	96.952171	274298.999694	5100306.59999899
6	Point	7	96.952171	274300.199694	5100306.59999899
7	Point	8	97.039696	274301.399694	5100306.59999899
8	Point	9	97.040154	274296.599694	5100305.39999899
9	Point	10	97.077507	274297.799694	5100305.39999899
10	Point	11	97.021126	274298.999694	5100305.39999899
….					
609475	Point	609476	97.630356	288520.199694	5086609.79999899
609476	Point	609477	97.602257	288521.399694	5086609.79999899
609477	Point	609478	98.053841	288512.999694	5086608.59999899
609478	Point	609479	97.682053	288514.199694	5086608.59999899
609479	Point	609480	97.400345	288515.399694	5086608.59999899
609480	Point	609481	97.63295	288516.599694	5086608.59999899
609481	Point	609482	97.355545	288517.799694	5086608.59999899
609482	Point	609483	97.551216	288518.999694	5086608.59999899
609483	Point	609484	97.56237	288520.199694	5086608.59999899
609484	Point	609485	97.457382	288521.399694	5086608.59999899

Appendix D: DEM of the entire river reach from WorldView-2 image

Sample rows of DEM are shown below. The complete data sheet is in a separate file.

FID	Shape	Point-ID	Bed-Elevation	Easting	Northing
(-)	(-)	(-)	(m)	(m)	(m)
1	Point	1	96.89583	274314.999694362	5100240.99999899
2	Point	2	96.66879	274312.999694361	5100238.99999899
3	Point	3	96.87307	274314.999694362	5100238.99999899
4	Point	4	96.27666	274310.999694361	5100236.99999899
5	Point	5	96.97843	274312.999694361	5100236.99999899
6	Point	6	97.49587	274314.999694362	5100236.99999899
7	Point	7	97.76571	274316.99969436	5100236.99999899
8	Point	8	96.95827	274306.99969436	5100234.99999899
9	Point	9	96.77851	274308.99969436	5100234.99999899
10	Point	10	96.74087	274310.999694361	5100234.99999899
….					
208935	Point	208935	97.90028	285660.999694359	5087004.99999899
208936	Point	208936	97.26769	285662.99969436	5087004.99999899
208937	Point	208937	96.82783	285664.999694361	5087004.99999899
208938	Point	208938	96.78276	285666.999694361	5087004.99999899
208939	Point	208939	97.26531	285668.999694362	5087004.99999899
208940	Point	208940	97.419	285670.99969436	5087004.99999899
208941	Point	208941	97.09514	285672.99969436	5087004.99999899
208942	Point	208942	96.91661	285674.999694361	5087004.99999899
208943	Point	208943	96.87307	285676.999694361	5087004.99999899
208944	Point	208944	97.31711	285678.999694362	5087004.99999899